



Title	Surface-related operation instabilities of GaN HEMTs and their control using Al ₂ O ₃ -based MOS structures
Author(s)	西口, 賢弥
Citation	北海道大学. 博士(工学) 甲第13083号
Issue Date	2018-03-22
DOI	10.14943/doctoral.k13083
Doc URL	http://hdl.handle.net/2115/70528
Type	theses (doctoral)
File Information	Kenya_Nishiguchi.pdf



[Instructions for use](#)

博士論文

Surface-related operation instabilities of GaN HEMTs and
their control using Al₂O₃-based MOS structures

GaN HEMT における表面起因の動作不安定性と Al₂O₃
MOS 構造を用いた制御

Kenya Nishiguchi

西口 賢弥

Graduate School of Information Science and Technology

Hokkaido University

北海道大学大学院 情報科学研究科

February, 2018

Acknowledgements

First of all, I would like to thank my supervisor, Prof. Tamotsu Hashizume. He guided and advised me sincerely throughout my bachelor, master, and doctoral courses. I wanted to give up to graduate doctoral course many times. However, I could get finally great results and knowledge about my research theme. These six years under his direction are irreplaceable for me. He is the best professor.

I am thankful to Prof. Takashi Fukui, Prof. Eiichi Sano, Prof. Junichi Motohisa, Prof. Shinjiro Hara, and Prof. Katsuhiro Tomioka for helping me study in RCIQE. Furthermore, I wish to thank to thank to Prof. Masamichi Akazawa, Prof. Taketomo Sato, and Prof. Seiya Kasai, the supervisors of our seminar group, for advising and discussing me during my study.

I wish to thank to my ex-colleagues, Dr. Kota Ohi and Dr. Yujin Hori. They advised me that the importance of doctoral course. In addition, I am thankful to Mr. Yutaka Senzaki. I worked hard with him. Furthermore, I am thankful to Dr. Joel T. Asubar and Dr. Zenji Yatabe. They helped me many times when I was depressed.

I wish to thank the current members of “Hashizume-group”, Dr. Maciek Matys, Mr. Shiro Ozaki, Mr. Shota Kaneki, Mr. Shota Toiya, Yuji Ando, Tatsuya Oyobiki, and Syota Sasaki. They helped my research.

I would like to thank to Dr. Marchin Miczek and Dr. Junji Kotani. Each of them developed a very wonderful simulator by using C language. Kotani’s simulator taught me how to calculate potential distribution and TFE curret. And, Marchin’s simulator taught me how to calculate C-V characteristics with interface states. I developed C-V calculation simulator based on both programs. This is the most important property of my university school life.

I wish to thank to Prof. Testu Kachi of Nagoya Univ., Dr. Naoki Hara of Fujitsu

Lab., Dr. Masataka Higashiwaki of National Institute of Information and Communications Technology (NICT), and Dr. Yasuo Koide of National Institute for Materials Science (NIMS). They discussed and advised me about my research theme.

I really appreciate to Dr. Hajime Fujikura, Dr. Masafumi Horikiri, and members of SCIOCS, Tetsuo Narita and members of Toyota Central Research and Development Laboratories, Inc. They provided very high quality epilayers for our group.

I really appreciate Dr. Dagmar Gregusova for sharing a lot of wonderful time with me throughout the collaboration reseach and many conferences. Furthemore, I would like to express many thanks to Prof. Jan Kuzmik, Dr. Milan Tapajna, and members of Slovak Academy of Sciences, for always discussing and advising me very kindly.

I would like to thank to Prof. Bouguslawa Adamowicz, and members of Silesian University of Technology, for giving me the opportunities to have the collaboration works with you.

I really appreciate Kentaro Sasaki and Ryutaro Kodaira. They are best colleague.

最後になりましたが、私の学位取得を最後まで応援して下さった両親、妹、そして妻に深く感謝申し上げます。

February, 2018 at RCIQE

Kenya Nishiguchi

Contents

Chapter 1	Introduction	7
1.1	Background	7
1.2	Benefits of Using Gallium Nitride (GaN)	9
1.3	GaN-based High Electron Mobility Transistors (HEMTs)	12
1.4	Merits of Metal-Insulator-Semiconductor (MIS) Structure	13
1.5	Several Issues of GaN-based HEMTs	15
1.6	Purpose of this Work	18
1.7	Outline	18
References		21
Chapter 2	Physical properties of GaN	25
2.1	Basic Properties of III-N Semiconductor Materials	25
2.2	The state of the art of Growth Method and Quality of GaN Crystal	26
2.3	AlGaN/GaN heterojunction	27
References		35
Chapter 3	Electronic States at Interface or Surface of Semicon- ductor	37
3.1	Introduction	37
3.2	Fermi level Pinning and it's Origin	37
3.3	Charge neutrality level	38
3.4	Metal-induced gap state model (MIGS)	39
3.5	Disorder-Induced Gap State Model (DIGS)	39
3.6	Unified defect model (UDM)	41

3.7	Influence of interface states at the insulator/GaN interface on the capacitance-voltage behavior of insulator/GaN MOS structures	41
3.8	Theoretical C-V curves of the Al ₂ O ₃ /GaN structure	44
3.9	Special Case of Interface States distributed both in energy and space	48
References		55
Chapter 4	Evaluation of surface charging at AlGaN surface using a dual-gate structure	59
4.1	Background	59
4.2	Device structure and fabrication process	60
4.3	Results and discussions	61
4.4	Conclusion	68
References		69
Chapter 5	Current linearity and operation stability in GaN MIS HEMTs	71
5.1	Background	71
5.2	Device Fabrication Processes	72
5.3	Extremely Decreased Electronic States at Al ₂ O ₃ /n-GaN Interface by Reverse-Bias Annealing	73
5.4	Results and Discussion	76
5.5	Conclusions	87
References		89
Chapter 6	Conclusion	93

Chapter 1

Introduction

1.1 Background

In recent years, the technological innovation in the field of information technology has been remarkable. The spread of information devices such as personal computers, the expansion of the role of the Internet and the spread of satellite broadcasting are progressing rapidly. However, there are several problems in the field of information technology.

1.1.1 Volume of mobile communication traffic

The volume of communication traffic has been increasing worldwide with the rapid spread of smartphones in recent years. The global volume of communication traffic is expected to reach 30×10^{18} bytes/month in 2020 as shown in Figure 1.1. Increases in communication facilities, speed, and capacity are thus required.

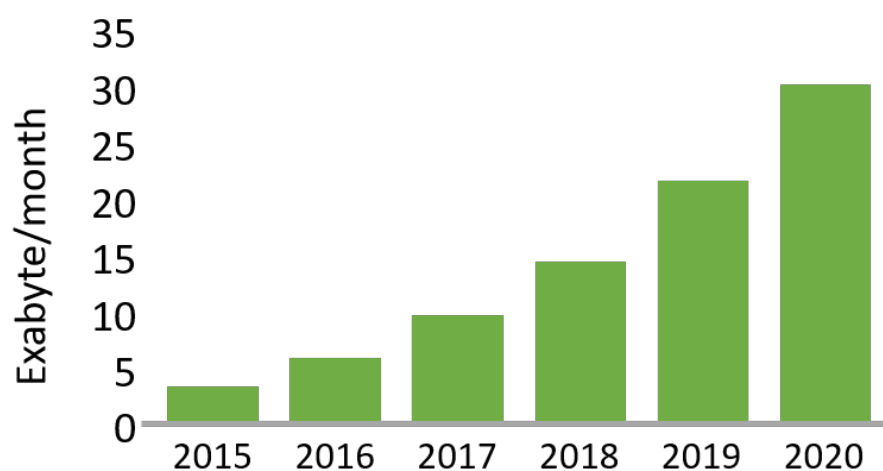


Figure 1.1. Predicted global volume of mobile communication.

The frequency band used for mobile communication in Japan is 700 MHz–2 GHz.

However, 5 GHz will be used in future [1]. Increasing the communication frequency can increase the speed and capacity of mobile communications. However, a disadvantage of using a high frequency in long-distance communication is the large degradation in the atmosphere. In addition, obstacles such as buildings adversely affect mobile communications. To solve these problems, it is necessary to improve the power of communication amplifiers used in base stations.

There is another problem in backhaul, that is, the intermediate links between base stations. The frequency band used for backhaul is extremely high, 40 to 50 GHz. In addition, the frequency band used for backhaul depends on that used for mobile communication.

1.1.2 Radars

Radars are used for weather observation, ships, automobiles, and so forth. The frequency band used for radars is around 10 GHz. In addition, the output power of radar is extremely high, 1 to 100 kW.

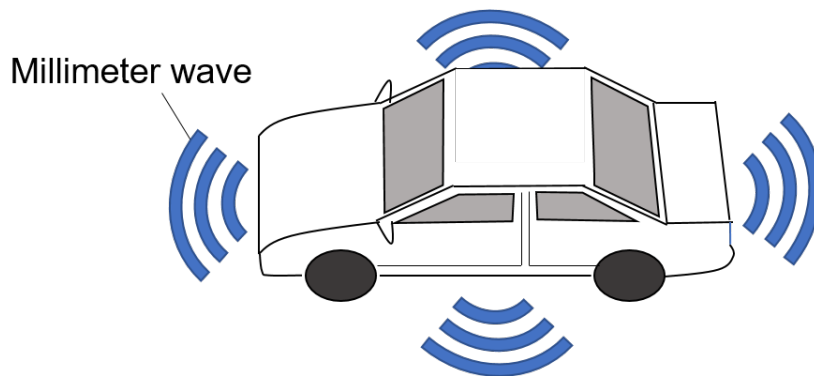


Figure 1.2. Millimeter-wave radars are used in automobiles.

The size of radars for automobiles is expected to decrease in future. The miniaturization of radars is an essential task because automobiles have fuel consumption and space constraints. In addition, it is necessary to use a high frequency to improve the accuracy of radars for automobiles as shown in Figure 1.2.

1.1.3 Wireless communication as an alternative to optical communication

Optical fiber communication is extremely fast, and its noise is small because it is a form of wired communication. However, if optical fibers are disconnected owing

to disasters or for other reasons, it seriously affects the communication network. In fact, 1.9 million fixed communication lines and 29000 mobile communication lines were damaged by the Great East Japan Earthquake in 2011.

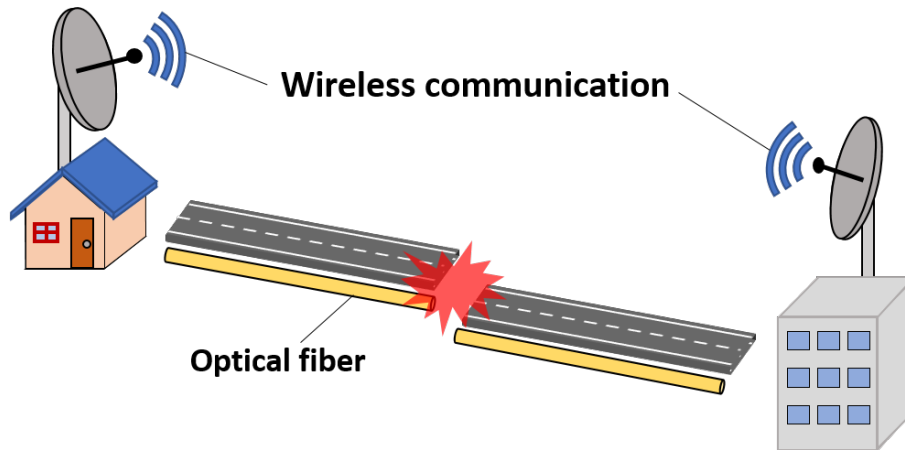


Figure 1.3. Wireless communications can be used when optical fibers are broken.

Wireless communication is useful in such cases as shown in Figure 1.3, and its equipment is convenient to move and install. In addition, a simple base station is extremely important in areas where the installation of optical fibers is difficult. The cost and time required to install communication networks with wireless networks can be reduced to less than those with optical fibers. For such base stations, miniaturization and high output power are required. The frequency band range of 30 to 300 GHz can be used for wireless communication. However, 1-W-class high-output-power amplifiers are required for transmission over a distance of a km order using the millimeter-wave band.

1.2 Benefits of Using Gallium Nitride (GaN)

Some currently used applications are shown in Figure 1.4. Most high-frequency/high-power applications are operated using vacuum tube amplifiers, not semiconductors. However, the power consumed by vacuum tube amplifiers is considerable since the vacuum tube constantly emits electrons in vacuum. Therefore, it is possible to downsize amplifiers and reduce their power consumption by replacing the vacuum tube with semiconductor devices.

A comparison of the properties of different semiconductor materials is shown in

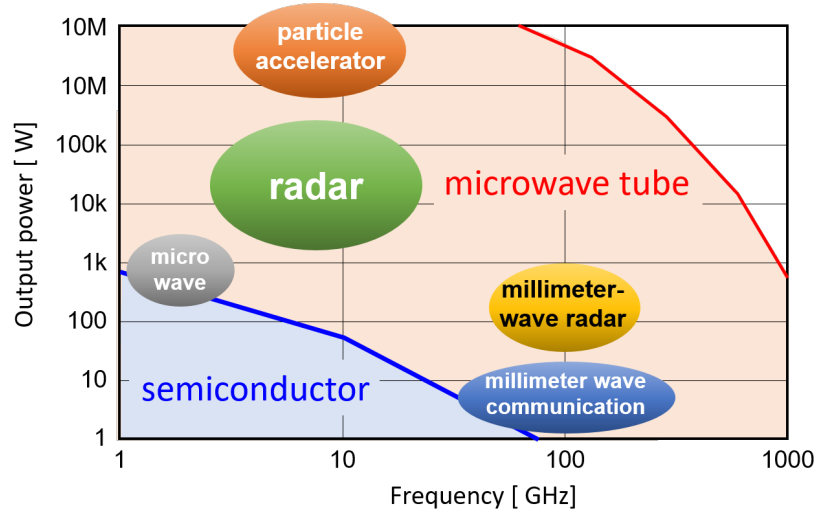


Figure 1.4. Output power and operating frequency of some applications.

Table 1.1. Gallium nitride (GaN) has a threefold wider band gap, a tenfold higher breakdown electric field, and a twofold higher saturation velocity than Si. Owing to its wide band gap, GaN exhibits stable operation even at high temperatures thus, a simpler cooling system can be employed in amplifiers using GaN transistors. Also, the size of passive components including reactance can be miniaturized because GaN-based devices can be switched at higher frequencies than Si-based devices. Furthermore, the dielectric breakdown electric fields of GaN and SiC are about 10 times larger than those of Si and GaAs. Owing to this property, it is possible to miniaturize amplifiers.

	Si	GaAs	4H-SiC	GaN
Bandgap (eV)	1.1	1.4	3.2	3.4
Breakdown electric field (MV/cm)	0.3	0.4	3	3
Thermal conductivity (W/cmK)	1.3	0.5	5	1.3
Electron mobility ($\text{cm}^2\text{V}^{-1}\text{s}^{-1}$)	1450	8500	950	2000
Electron saturation velocity (cm/s)	1×10^7	1.3×10^7	2×10^7	2.7×10^7

Table 1.1. Basic physical properties of various semiconductor materials.

In addition, the electron mobility and electron velocity are very important for high-radio-frequency (RF) applications. Electron mobility is defined as:

$$v = \mu E, \quad (1.1)$$

where v , μ , and E are electron velocity, electron mobility, and electric field, respectively. However, the electron velocity is not determined only by electron mobility.

Monte Carlo simulations of electron velocity versus electric field for GaN have been reported [2]. The results of these simulations are shown in Figure 1.5. Results for GaAs, Si, and SiC are also shown for comparison. The peak velocity in GaN is close to 3×10^7 cm/s and the saturation velocity is 1.5×10^7 cm/s. Both values are considerably higher than those for Si and GaAs.

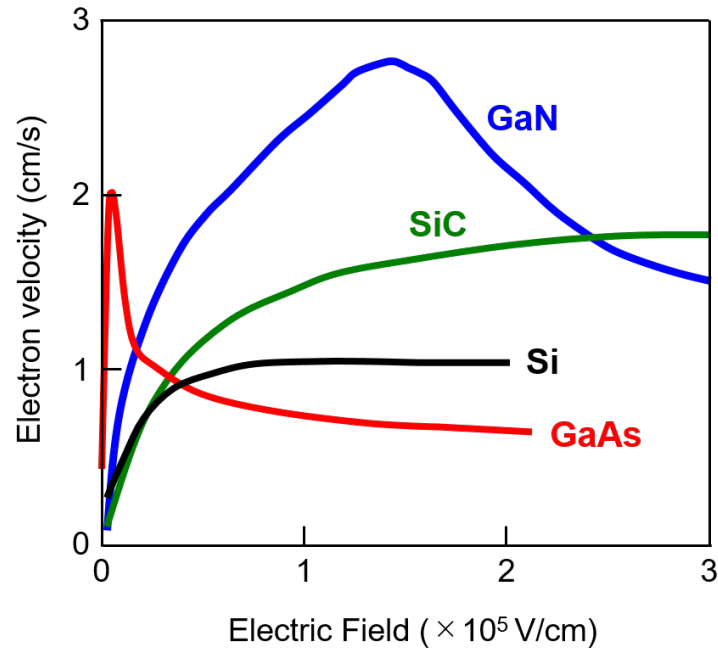


Figure 1.5. Electron drift velocity as a function of electric field for Si, GaAs, SiC, and GaN at 300 K [2].

Johnson's figure of merit is a measure of the suitability of a semiconductor material for high-frequency power transistor applications and requirements [3]. It is defined as:

$$V_m f_T = \frac{E_B v_s}{2\pi}, \quad (1.2)$$

where V_m and f_T are the maximum allowable applied voltage and cutoff frequency, respectively. Figure 1.6 shows Johnson's figure of merit of each semiconductor material. The figure shows that GaN is highly suitable for high-power RF applications.

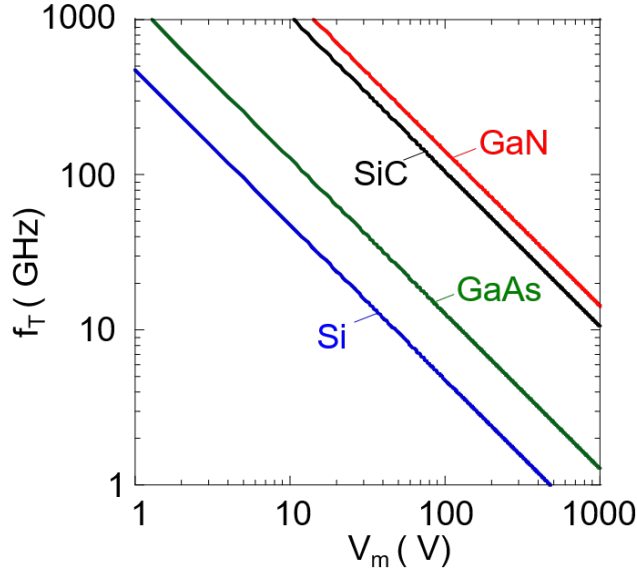


Figure 1.6. Johnson's figure of merit of Si, GaAs, SiC, and GaN.

1.3 GaN-based High Electron Mobility Transistors (HEMTs)

One of the main advantages of GaN is the two-dimensional electron gas (2DEG) generated at the interface of heterostructures such as AlGa_N/Ga_N and InAlN/Ga_N. The carrier densities of the 2DEG are $1 \times 10^{13} \text{ cm}^{-2}$ at the AlGa_N/Ga_N interface and $2 \times 10^{13} \text{ cm}^{-2}$ at the InAlN/Ga_N interface. In addition, the electron mobility is $2000 \text{ cm}^2\text{V}^{-1}\text{s}^{-1}$ at both interfaces.

For GaN-based transistors, great effort has been devoted to improving the device performance and operation stability/reliability. In particular, AlGa_N/Ga_N high-electron-mobility transistors (HEMTs) have been making steady progress in terms of high-frequency and high-power performance [4–10]. Figure 1.7 shows a schematic illustration of an AlGa_N/Ga_N HEMT.

By using GaN HEMTs with breakdown voltages of up to 600 V, highly efficient high-frequency switching systems with a compact size have been demonstrated [8, 10, 11]. By downscaling the gate length to the sub-100-nm regime in conjunction with state-of-the-art technologies, Shinohara and co-workers have recently achieved ultrahigh-speed operation with record-high maximum current gain cutoff frequency (f_T) of 454 GHz with accompanying power gain cutoff frequency

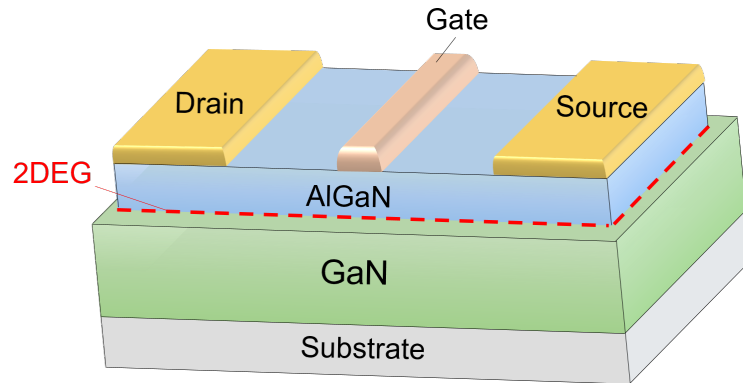


Figure 1.7. Schematic illustration of AlGaN/GaN HEMT.

(f_{max}) of 444 GHz on a 20 nm gate HEMT [4, 12]. Figure 1.8 shows off-state breakdown voltage (BV_{off}) versus current gain f_T for GaN-based HEMTs.

It is desirable for fifth-generation (5G) communication systems that the W-band (75–110 GHz) and E-band (60–90 GHz) frequency ranges are used for the wireless backhaul.

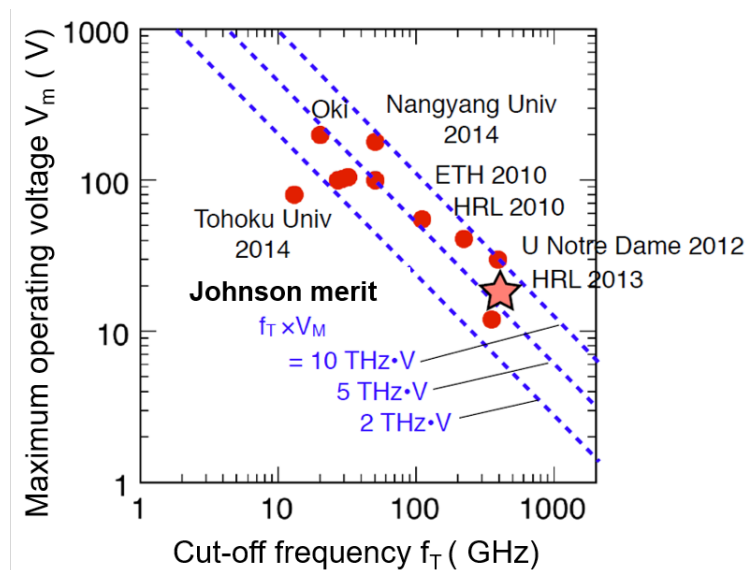


Figure 1.8. Off-state breakdown voltage versus current gain cutoff frequency for GaN-based HEMTs [13].

1.4 Merits of Metal-Insulator-Semiconductor (MIS) Structure

For reduced power consumption as well as failure protection, normally-off operation is highly preferred, particularly for power switching devices. Obviously, normally-off

devices require a positive gate voltage to be turned on, which leads to extremely high leakage current levels in Schottky gate (SG) devices. Thus, a metal-insulator-semiconductor (MIS) gate is necessary for normally-off power switching transistors as shown in Figure 1.9. For RF applications, 5G wireless systems also require higher

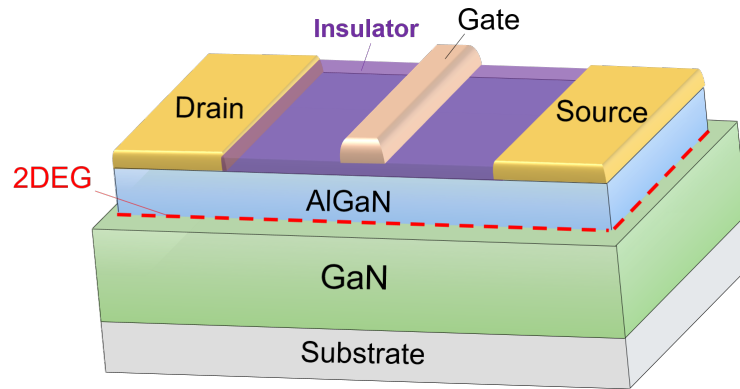


Figure 1.9. Schematic illustration of AlGaIn/GaN MIS HEMT.

efficiency and linearity for RF power transistors. Power amplifiers using SG GaN HEMTs suffer from reduced gain and efficiency with increasing input RF power owing to significant gate leakage currents caused by a large input swing that may drive devices deep into the forward bias regime as shown in Figure 1.10. Such high leakage currents seriously affect the operation stability and large-signal linearity of power amplifiers [14]. Moreover, a suitable surface passivation scheme is necessary for the stable and reliable operation of power devices.

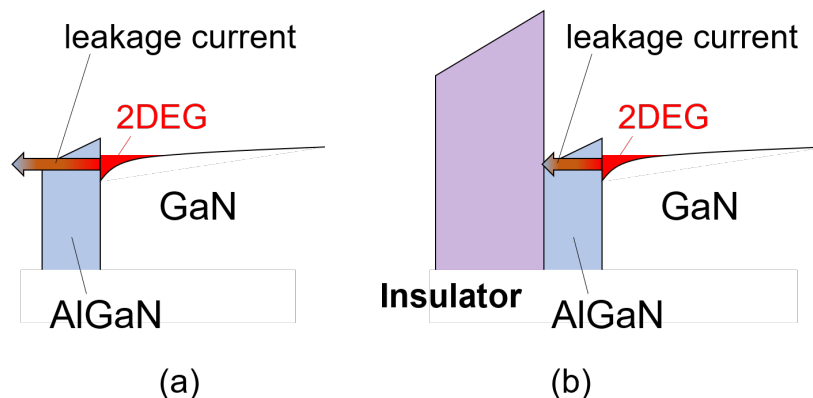


Figure 1.10. Schematic illustration of band diagrams of AlGaIn/GaN HEMTs with (a) Schottky and (b) MIS gate structures.

An MIS structure is very effective for overcoming such problems related to the SG

structure. For example, a gate-stack technology based on the principles of interface engineering, barrier-layer engineering, and the gate dielectric technique has been employed in normally-off GaN HEMTs for power switching devices [8, 10, 15, 16]. For RF devices, Kanamura et al. demonstrated that the gate leakage current was sufficiently controlled in an AlGaIn/GaN MIS-HEMT even under high-input-power operation [14]. Thus, MIS-HEMTs can accommodate a wider input signal sweep than Schottky-gate, resulting in a higher maximum output power. In addition, the MIS structure is necessary for InAlN/GaN HEMTs. GaN HEMTs using an InAlN electron-supplying layer are promising for enhancing 2DEG density because of their high spontaneous polarization and high band offset at the conduction band [17]. In fact, Makiyama et al. demonstrated an output power density of 3 W/mm at 96 GHz in a GaN HEMT using quaternary InAlGaIn barrier layers [18]. However, the large gate leakage current in InAlN/GaN HEMTs often limits their operation. The MIS structure is suitable for addressing the leakage current issue and therefore increasing the performance of InAlN/GaN HEMTs.

1.5 Several Issues of GaN-based HEMTs

1.5.1 Reliability issues of the MIS structure

Since the quality of the semiconductor/insulator interface significantly affects the transistor performance, a chemically stable MIS structure with low interface state density should be developed for practical device application [15, 19, 20]. In this regard, various insulators have been applied to achieve GaN MIS HEMTs with excellent performance. However, several problems remain unsolved [20]. The instability of the threshold voltage (V_{TH}) is one of the most serious problems. Some groups have reported that a V_{TH} shift appears under different gate bias conditions in MIS-HEMTs [21–24], as shown in Figure 1.11 [24]. The charging state of the interface traps varies with the gate bias, and excess interface charges, particularly at deeper electronic states, are responsible for such V_{TH} fluctuation.

Another problem is the unexpected degradation of current linearity in GaN-based MIS HEMTs. Although the dynamic range of input signal sweeping is one of the advantages of MIS HEMTs, some groups have reported sudden current saturation

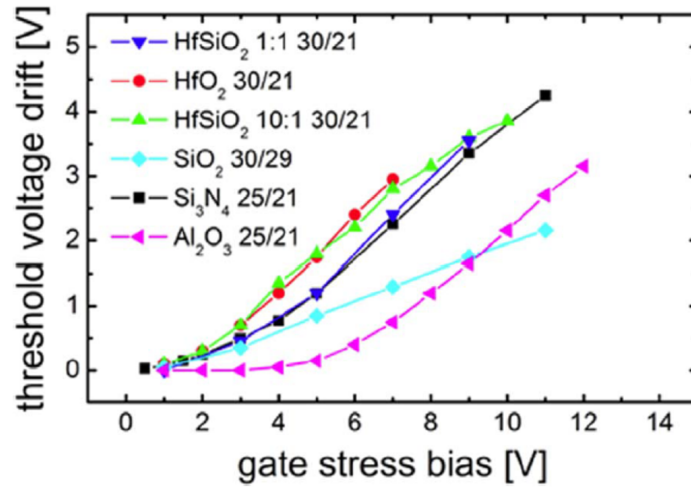


Figure 1.11. Comparison of gate-stress induced V_{TH} drift of AlGaIn/GaN MIS-HEMTs for different dielectrics with different insulators and AlGaIn thicknesses. [24]

at a forward bias [25, 26] as shown in Figure 1.12.

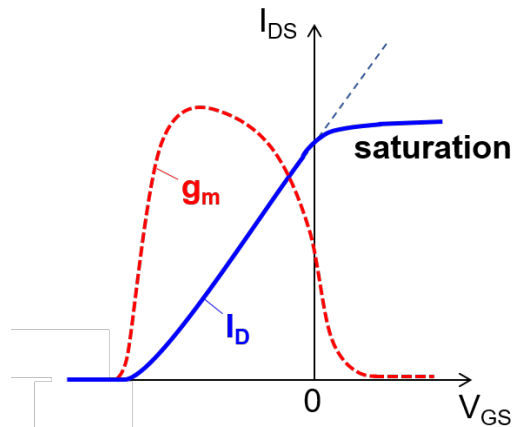


Figure 1.12. Illustration of I_D saturation behavior at forward bias.

It is likely that a high density of electronic states at the insulator/barrier interface, particularly near the conduction band edge, screens the gate electric field and reduces the control of the surface potential of the barrier layer. This prevents a further increase in the 2DEG density, leading to pronounced current saturation at a forward gate bias. Such degradation of the current linearity may be responsible for gain loss and the degradation of large-signal linearity in power amplifiers.

1.5.2 Current collapse

Another major concern is the current collapse phenomenon, which is a temporary reduction of the drain current following the application of a high voltage and/or high power, in both on- and off-state operations [27, 28]. Nishiguchi et al. reported that the drain-source voltage (V_{DS}) enhances current collapse as shown in Figure 1.13 [29]. Figure 1.13 shows that the saturation drain current is decreased and the on-resistance is increased after applying off-stress.

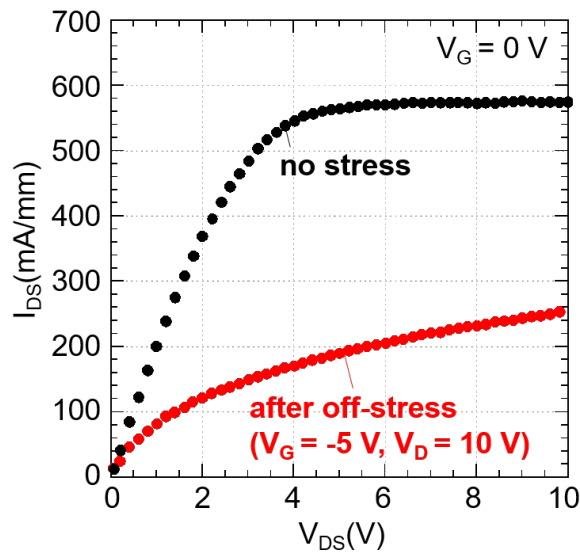


Figure 1.13. Current collapse of AlGaIn/GaN Schottky HEMTs [29].

According to the most widely accepted “virtual gate” model proposed by Vetury et al. [28], current collapse is mainly due to surface charging at part of the gate drain (GD) access region close to the gate edge. On the basis of the gate injection and surface hopping model [30, 31] illustrated in Figure 1.14, electron conduction via trap-to-trap hopping can be promoted by increasing the drain voltage.

Consequently, this may lead to the widening of the virtual gate from the gate edge to a further inside the GD access region. Using Kelvin probe force microscopy, several groups have reported the changes in the surface potential of AlGaIn due to surface trap occupancy in the GD access region after applying an off-bias stress to AlGaIn/GaN HEMTs [32–36]. In addition, it has recently been demonstrated that trapping can extend as far as a distance of 100 nm order from the drain-side

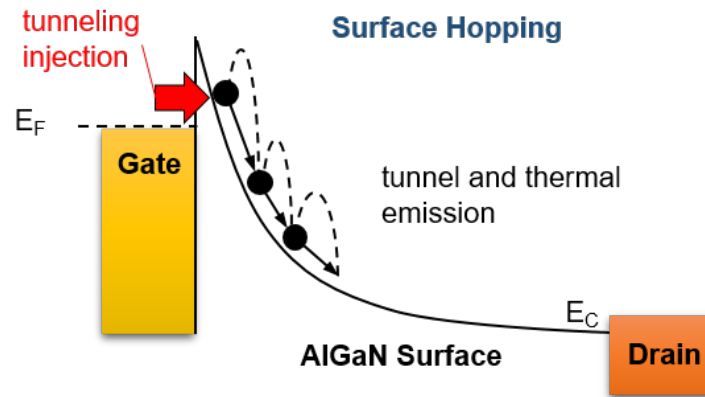


Figure 1.14. Gate injection and surface hopping model.

gate edge [35,36]. However, there have been few reports on the effects of spatially induced surface charging on the current–voltage (I–V) characteristics of AlGaN/GaN HEMTs.

1.6 Purpose of this Work

As discussed in Section 1.3, AlGaN/GaN HEMTs have enormous potential for high-power RF applications. In addition, the MIS structure is very effective for improving their performance as described in Section 1.4. However, several problems remain unsolved, as described in Section 1.5.1, as well as the problems discussed in Section 1.5.2.

The purpose of this work is to evaluate the effect of interface states on the electrical characteristics of AlGaN/GaN HEMTs. In addition, a method of evaluating the length of the surface charging area and a process to decrease the density of interface states are proposed.

1.7 Outline

This thesis includes six chapters.

In Chapter 2, the physical properties of GaN, such as its crystal structure, are introduced. The spontaneous and piezoelectric polarizations at the AlGaN/GaN heterostructure and the generation mechanism of the 2DEG-induced polarization effect are also introduced. Furthermore, the electrical conduction properties of GaN and an AlGaN/GaN heterointerface are described.

In Chapter 3, the interface states are explained, and their models and their effects on electrical characteristics are described. Finally, the process to decrease the interface state density that our group is researching is introduced.

In Chapter 4, the fabrication process and DC basic characteristics of Schottky AlGa_N/Ga_N HEMTs are discussed. In addition, the current collapse due to negative gate stress is described. It is probable that surface states at the AlGa_N surface cause the current collapse.

In Chapter 5, the current linearity and operation stability of AlGa_N/Ga_N MOS HEMTs are discussed. The relationship between these characteristics and the interface states is investigated in this work.

In Chapter 6, the present work is summarized and a conclusion is given.

References

- [1] T. Hashizume, K. Nishiguchi, S. Kaneki, J. Kuzmik, and Z. Yatabe, *Mater. Sci. Semicond. Process.* (2017).
- [2] S. C. Jain, M. Willander, J. Narayan, and R. Van Overstraeten, *J. Appl. Phys.* **87**, 965 (2000).
- [3] E. O. Johnson, *RCA Rev.* **26**, 163 (1965).
- [4] K. Shinohara, D.C. Regan, Y. Tang, A. L. Corrion, D.F. Brown, J.C. Wong, J.F. Robinson, H.H. Fung, A. Schmitz, T.C. Oh, S.J. Kim, P.S. Chen, R.G. Nagele, A.D. Margomenos, and M. Micovic, *IEEE Trans. Electron Devices* **60**, 2983 (2013).
- [5] D.S. Lee, Z. Liu, and T. Palacios, *Jpn. J. Appl. Phys.* **53**, 100212 (2014).
- [6] T. Ueda, M. Ishida, T. Tanaka, and D. Ueda, *Jpn. J. Appl. Phys.* **53**, 100214 (2014).
- [7] T. Kachi, *Jpn. J. Appl. Phys.* **53**, 100210 (2014).
- [8] F. Roccaforte, P. Fiorenza, G. Greco, R.L. Nigro, F. Giannazzo, A. Patti, and M. Saggio, *Phys. Status Solidi A* **211**, 2063 (2014).
- [9] M. Kuzuhara and H. Tokuda, *IEEE Trans. Electron Devices* **62**, 405 (2015).
- [10] K.J. Chen, O. Haeberlen, A. Lidow, C. I. Tsai, T. Ueda, Y. Uemoto, and Y. Wu, *IEEE Trans. Electron Devices* **64**, 779 (2017).
- [11] E. A. Jones, F. Wang, and D. Costinett, *IEEE J. Emerging and Selected Topics in Power Electronics* **4**, 707 (2016).
- [12] Y. Tang, K. Shinohara, D. Regan, A. Corrion, D. Brown, J. Wong, A. Schmitz, H. Fung, S. Kim, and M. Micovic, *IEEE Electron Device Lett.* **36**, 549 (2015).
- [13] K. Kobayashi, S. Hatakeyama, T. Yoshida, Y. Yabe, D. Piedra, T. Palacios, T. Otsuji, and T. Suemitsu, *Appl. Phys. Express* **7**, 096501 (2014).
- [14] M. Kanamura, T. Kikkawa, T. Iwai, K. Imanishi, T. Kubo, and K. Joshin, *IEDM Tech. Dig.*, 2005, p. 572.

- [15] F. Roccaforte, P. Fiorenza, G. Greco, M. Vivona, R. L. Nigro, F. Giannazzo, A. Patti, and M. Saggio, *Appl. Surf. Sci.* **301**, 9 (2014).
- [16] S. Yang, S. Liu, C. Liu, M. Hua, and K.J. Chen, *Semicond. Sci. Technol.* **31**, 024001 (2016).
- [17] J. Kuzmik, *IEEE Electron Device Lett.* **22**, 510 (2001).
- [18] K. Makiyama, S. Ozaki, T. Ohki, N. Okamoto, Y. Minoura, Y. Niida, Y. Kamada, K. Joshin, K. Watanabe, and Y. Miyamoto, *IEDM Tech. Dig.*, 2015, p. 213.
- [19] Z. Yatabe, Y. Hori, W. Ma, J.T. Asubar, M. Akazawa, T. Sato, and T. Hashizume, *Jpn. J. Appl. Phys.* **53**, 100213 (2014).
- [20] Z. Yatabe, J.T. Asubar, and T. Hashizume, *J. Phys. D* **49**, 393001 (2016).
- [21] Y. Lu, S. Yang, Q. Jiang, Z. Tang, B. Li, and K.J. Chen, *Phys. Status Solidi C* **10**, 1397 (2013).
- [22] M. Ľapajna, M. Jurkovič, L. Válik, Š. Haščik, D. Gregušová, F. Brunner, E.-M. Cho, and J. Kuzmik, *Appl. Phys. Lett.* **102**, 243509 (2013).
- [23] D.W. Johnson, R.T.P. Lee, R.J.W. Hill, M.H. Wong, G. Bersuker, E.L. Piner, P.D. Kirsch, and H.R. Harris, *IEEE Trans. Electron Devices* **60**, 3197 (2013).
- [24] P. Lagerger, P. Steinschifter, M. Reiner, M. Stadtmuller, G. Denifl, A. Naumann, J. Muller, L. Wilde, J. Sundqvist, D. Pogany, and C. Ostermaier, *Appl. Phys. Lett.* **105**, 033512 (2014).
- [25] Z. Zhang, W. Li, K. Fu, G. Yu, X. Zhang, Y. Zhao, S. Sun, L. Song, X. Deng, Z. Xing, L. Yang, R. Ji, C. Zeng, Y. Fan, Z. Dong, Y. Cai, and B. Zhang, *IEEE Electron Device Lett.* **38**, 236 (2017).
- [26] X. Lu, K. Yu, H. Jiang, A. Zhang, and K.M. Lau, *IEEE Trans. Electron Devices* **64**, 824 (2017).
- [27] M. A. Khan, M. S. Shur, Q. C. Chen, and J. N. Kuznia, *Electron. Lett.* **30**, 2175 (1994).
- [28] R. Vetry, N. Q. Zhang, S. Keller, and U. K. Mishra, *IEEE Trans. Electron Devices* **48**, 560 (2001).
- [29] K. Nishiguchi, J. T. Asubar, and T. Hashizume, *Jpn. J. Appl. Phys.* **53**, 070301 (2014).

-
- [30] R. J. Trew, D. S. Green, and J. B. Shealy, *IEEE Microwave Mag.* **10** [4], 116 (2009).
- [31] J. Kotani, M. Tajima, S. Kasai, and T. Hashizume, *Appl. Phys. Lett.* **91**, 093501 (2007).
- [32] G. Koley, V. Tilak, L. F. Eastman, and M. G. Spencer, *IEEE Trans. Electron Devices* **50**, 886 (2003).
- [33] K. Nakagami, Y. Ohno, S. Kishimoto, K. Maezawa, and T. Mizutani, *Appl. Phys. Lett.* **85**, 6028 (2004).
- [34] S. Kamiya, M. Iwami, T. Tsuchiya, M. Kurouchi, J. Kikawa, T. Yamada, A. Wakejima, H. Miyamoto, A. Suzuki, A. Hinoki, T. Araki, and Y. Nanishi, *Appl. Phys. Lett.* **90**, 213511 (2007).
- [35] S. DasGupta, L. B. Biedermann, M. Sun, R. Kaplar, M. Marinella, K. R. Zavadil, S. Atcitty, and T. Palacios, *Appl. Phys. Lett.* **101**, 243506 (2012).
- [36] D. W. Cardwell, A. R. Arehart, C. Poblenz, Y. Pei, J. S. Speck, U. K. Mishra, S. A. Ringel, and J. P. Pelz, *Appl. Phys. Lett.* **100**, 193507 (2012).

Chapter 2

Physical properties of GaN

2.1 Basic Properties of III-N Semiconductor Materials

2.1.1 Crystal Structure

III-N semiconductors i.e GaN, AlGaN can be crystallized in either hexagonal (wurtzite, see Figure 2.1(a)) or cubic (zincblende, Figure 2.1(b)) structure depending on the substrate symmetry and growth conditions. In the wurtzite structure, the cation and anion atoms align in the same direction (vertically, in this case). Such symmetrical configuration with the ionic alignment leads to characteristic polarization effects. Furthermore GaN wurtzite crystal structure has a wider bandgap than the zinc-blend structure. Therefore for the fabrication of power devices, GaN wurtzite is often used. Moreover it should be noted that GaN-based HEMTs are mainly fabricated on the c-plane of GaN wurtzite.

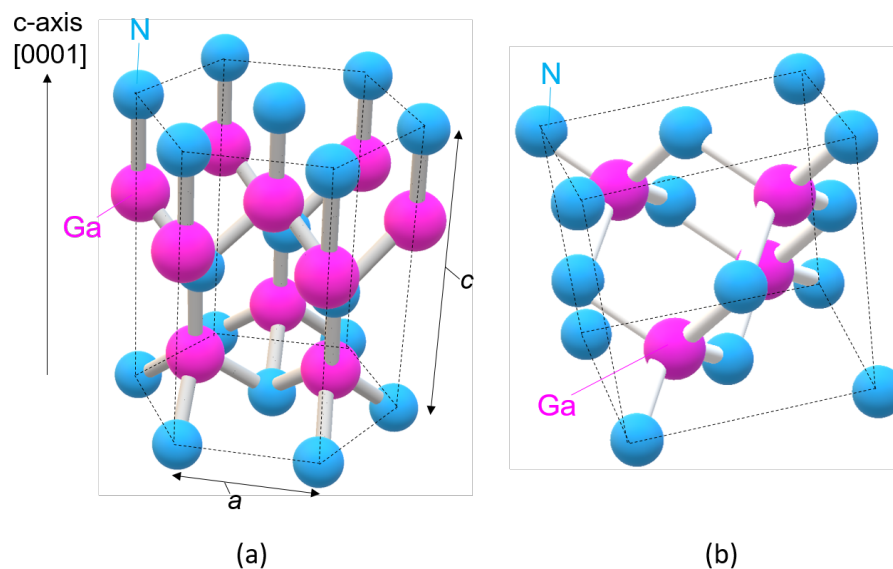


Figure 2.1. Schematic illustration of (a)wurtzite and (b) zinc-blend crystal of GaN.

This is because the wurtzite III-N do not have inversion symmetry along the c-axis and thus the strong ionicity results in a large polarization along the $[0001]$ crystal direction (see Figure 2.2(a)). This feature will be discussed in more detail in the next section. On the other hand, a- and m- plane of GaN wurtzite (see Figure 2.2 (b) and (c)) are very important for vertical type GaN devices, because in such devices drain current flows through the a- and m-plane.

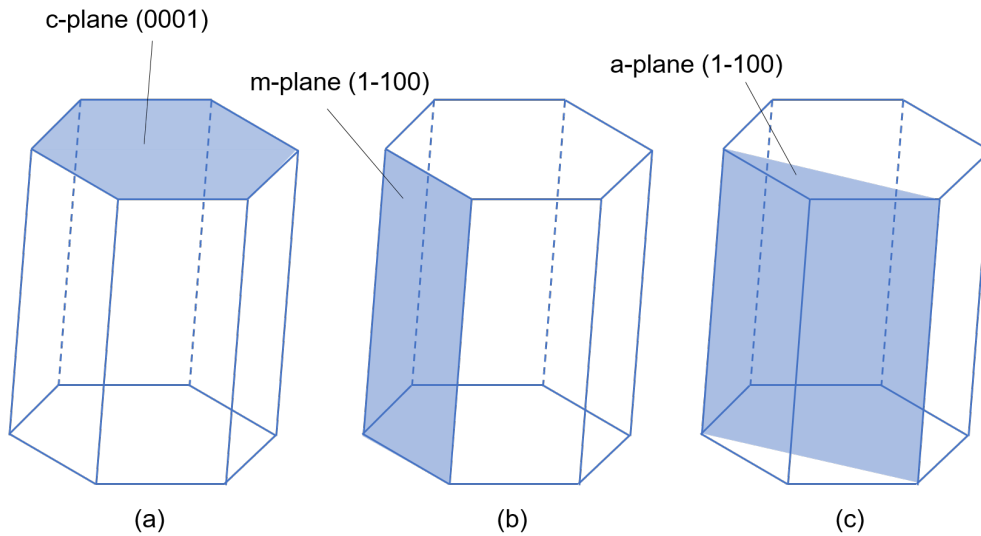


Figure 2.2. Schematic illustration of each plane of wurtzite structure.

2.2 The state of the art of Growth Method and Quality of GaN Crystal

Due to the lack of the native substrates GaN-based devices were developed so far on heterogeneous substrates such SiC or Sapphire. Furthermore, it should be noted that it's difficult to produce high-purity layers of GaN by MOCVD due to the presence of residual carbon impurities in the range 10^{15} to 10^{17} cm^{-3} [1–4]. However, very recently Fujikura et al. [5] developed quartz-free hydride-vapor-phase epitaxy (HVPE) method (see Figure 2.3). By using this method the authors were able to obtain highly pure GaN grown on freestanding GaN substrates with extremely low residual impurities concentration. In particular the Si concentration was below the detection limit of SIMS measurement, and less than 5×10^{14} cm^{-3} . The O and C concentrations were below their relevant detection limits, and less than the mid- 10^{15} cm^{-3} region. In addition, the high-purity layer grown by quartz-free HVPE

showed an insulating nature in the absence of a dopant.

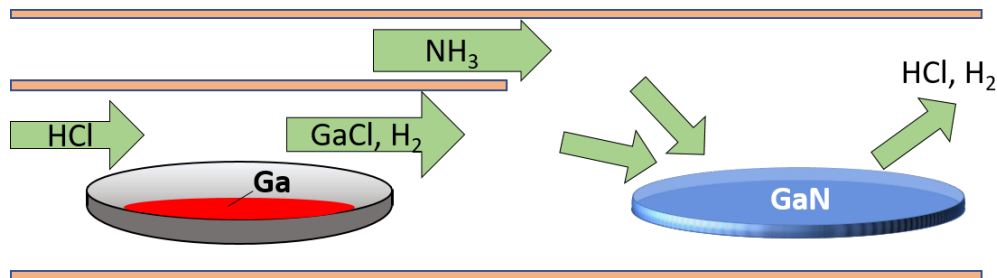


Figure 2.3. Schematic drawing of the HVPE system.

Therefore quartz-free HVPE method appears to be an effective method for the fabrication of the native GaN substrates and in consequence power devices.

2.3 AlGaN/GaN heterojunction

2.3.1 Alloys and heterojunctions Using III-N Semiconductors

III-N semiconductors also enable us to realize various types of III-N alloys having different bandgap and lattice constant. Figure 2.4 shows the relationship between lattice constant and bandgap for GaN, AlN, InN, and their alloys. InAlN has an additional unique feature for HEMTs. When the In composition ratio is 13 %, the lattice constant a of $\text{In}_{0.13}\text{Al}_{0.78}\text{N}$ in accordance with that of GaN can be prepared on the c -plane of GaN layer. Besides that, the large conduction-band offset at the InAlN/GaN interface has a big merit for the HEMT application.

AlGaN is an alloy of AlN and GaN. The AlGaN/GaN heterojunction are the most popular application for the HEMTs as was shown in the previous chapter. Comparing with the InAlN/GaN system, AlGaN and GaN have no lattice-matching selections, resulting in the tensile-straining in the AlGaN/GaN heterostructures. This feature leads to the polarization effects which will be explained in the next section.

2.3.2 Polarization effects in III-N heterojunctions

As shown in Figure 2.1, III-Ns grown on the c -plane leads to the “spontaneous” polarization due to the symmetric configuration of cations and anions in the c -axis direction. Ambacher et al. [9] reported the following spontaneous polarization charge densities:

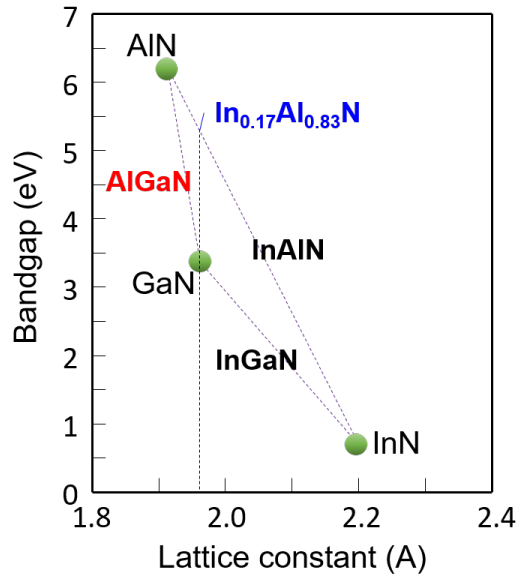


Figure 2.4. Lattice constant vs. bandgap relations for GaN, AlN, and InN [6–8].

$$\text{GaN:}P_{\text{sp}} = -1.8 \times 10^{13}/\text{cm}^2,$$

$$\text{AlN:}P_{\text{sp}} = -5.1 \times 10^{13}/\text{cm}^2,$$

$$\text{InN:}P_{\text{sp}} = -2.0 \times 10^{13}/\text{cm}^2.$$

The polarization charges are induced both on the *c*-plane and the opposite *c*-plane, as shown in Figure 2.5(a) and (b). In the case of the (0001) Ga-face surface crystal (see Figure 2.5(a)), the negative charges are induced by the cation atoms, Ga, Al. As a consequence, the spontaneous polarization field is oriented in the [0001] direction (see Figure 2.5(a)). On the other hand, in the case of the (000-1) N-face surface, the spontaneous polarization field shows the [0001] direction (see Figure 2.5(b)).

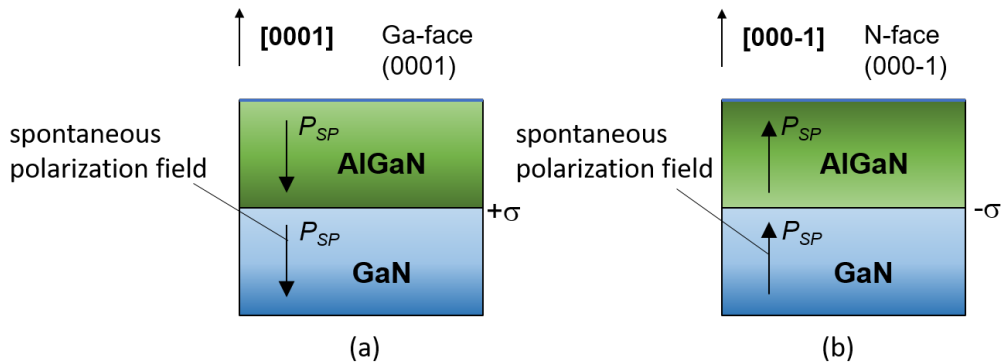


Figure 2.5. Directions of the spontaneous polarization field in (a) Ga-face and (b) N-face AlGaN/GaN heterostructure.

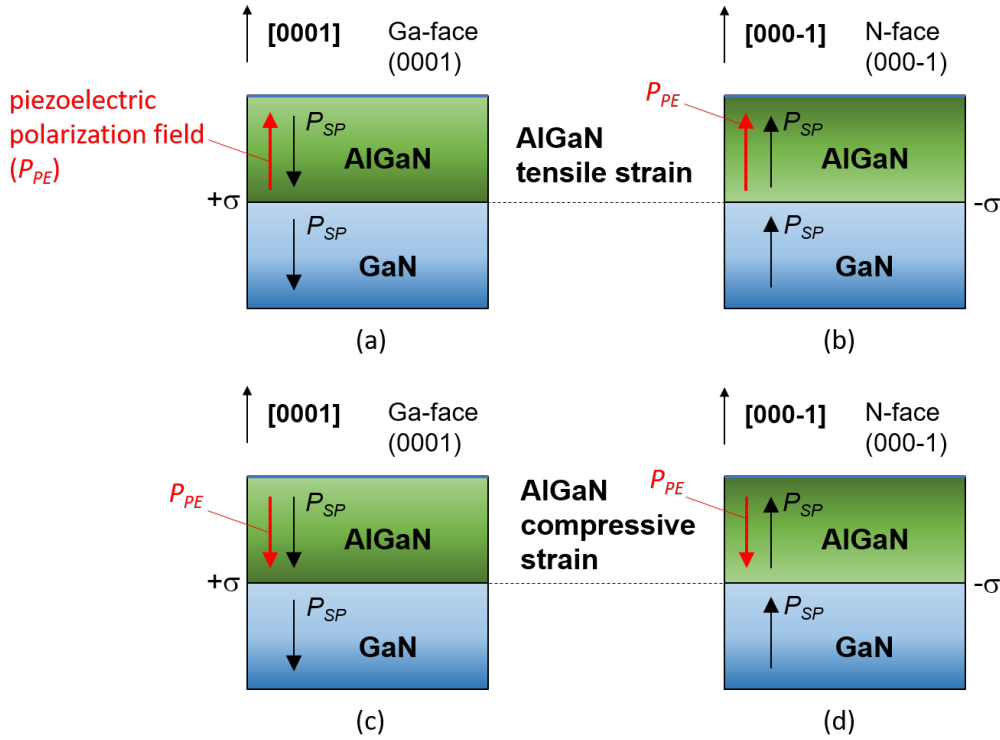


Figure 2.6. Directions of the piezoelectric polarization field in Ga-face (a and c) and N-face (b and d).

In addition to the spontaneous polarization, the lattice strain and compression due to the lattice-mismatched junction induces the piezoelectric polarization. Let us consider this polarization effect in the AlGa_N/Ga_N heterojunction. The most important difference between spontaneous and piezoelectric polarization is that the spontaneous polarization is independent the strain while piezoelectric polarization is strain induced. Ambacher et al. [9] have investigated the directions of piezoelectric polarization field for Ga-face, N-face strained, unstrained AlGa_N/Ga_N heterostructure as shown in Figure 2.6. As can be see from this figure piezoelectric and spontaneous polarization field is parallel in the case of tensile strain (see Figure 2.6(a) and (b)) and anti parallel in the case of compressively strain AlGa_N layer (see Figure 2.6(c) and (d)). Finally it should be mentioned that due to the polarization charges both spontaneous and piezoelectric, the potential of the heterojunction is bended downward, and in consequence 2DEG is induced.

2.3.3 2DEG induced at III-N heterointerfaces

Figure 2.7 shows the band diagram of the AlGa_xN/GaN heterojunction at equilibrium state. As was mentioned before, the band bended downward by the internal electric fields that create the potential quantum well at the AlGa_xN/GaN interface. As a result, the 2DEG with the high electron density is induced at the heterointerface. The electron mobility of such 2DEG is not affected by the impurity scattering because the internal electric fields are induced even in un-doped III-N systems. Note that the origin of 2DEG has not been cleared yet. The III-N electron devices utilizing such 2DEG are known as “heterojunction-field-effect transistors (HFETs)” or “high-electron-mobility transistors (HEMTs)”.

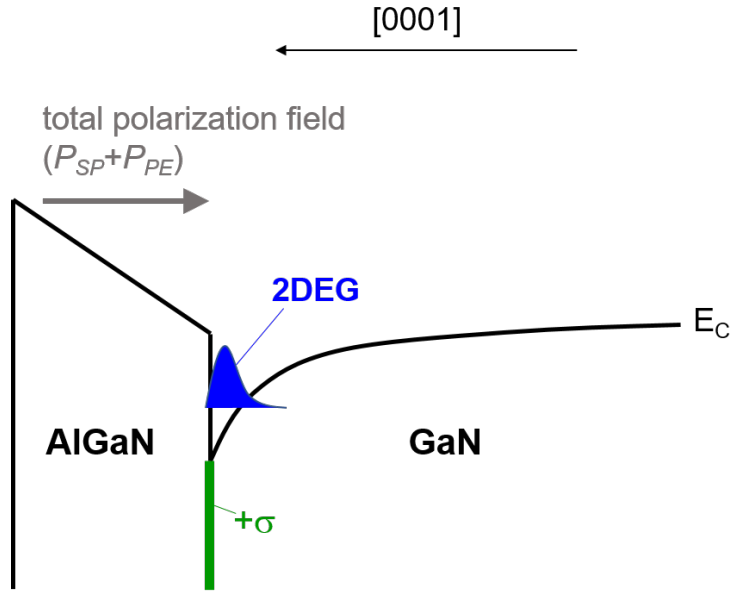


Figure 2.7. Schematic illustration of the conduction-band diagram of AlGa_xN/GaN heterostructure.

Ibbetson et al. proposed the following equation for the calculation 2DEG density [10]:

$$qn_s = \sigma_{PZ}(1 - t_{CR}/t), \quad (2.1)$$

where n_s , σ_{PZ} , t_{CR} , and t are 2DEG density, polarization-induced charge at AlGa_xN/GaN interface, the critical thickness, and thickness of AlGa_xN layer, respectively [9].

The spontaneous polarization of AlGa_xN is calculated as follows:

$$P_{SP}^{Al_xGa_{1-x}N} = P_{SP}^{AlN}x + P_{SP}^{GaN}(1-x), \quad (2.2)$$

where P_{SP}^{AlN} and P_{SP}^{GaN} are spontaneous polarization of AlN and GaN, respectively. The difference between spontaneous polarization of Al_xGa_{1-x}N and GaN ΔP_{SP} is calculated as follows:

$$\Delta P_{SP} = P_{SP}^{Al_xGa_{1-x}N} - P_{SP}^{GaN}. \quad (2.3)$$

In order to obtain ΔP_{SP} , it is necessary first calculated lattice constants. The lattice constant of AlGa_xN can be calculated as follows:

$$a_{Al_xGa_{1-x}N} = a_{AlN}x + a_{GaN}(1-x), \quad (2.4)$$

where a_{AlN} and a_{GaN} are a-lattice constants of AlN and GaN, respectively.

The elastic constant of AlGa_xN is calculated as follows:

$$C_{13(Al_xGa_{1-x}N)} = C_{13(AlN)}x + C_{13(GaN)}(1-x), \quad (2.5)$$

$$C_{33(Al_xGa_{1-x}N)} = C_{33(AlN)}x + C_{33(GaN)}(1-x), \quad (2.6)$$

where $C_{13,33(AlN,GaN)}$ are elastic constants of AlN and GaN, respectively.

The piezoelectric constant of AlGa_xN is calculated as follows:

$$e_{13(Al_xGa_{1-x}N)} = e_{13(AlN)}x + e_{13(GaN)}(1-x), \quad (2.7)$$

$$e_{33(Al_xGa_{1-x}N)} = e_{33(AlN)}x + e_{33(GaN)}(1-x), \quad (2.8)$$

where $e_{13,33(AlN,GaN)}$ are piezoelectric constants of AlN and GaN, respectively.

Using equation 2.2–2.8, the piezoelectric polarization charge can be calculated as follows:

$$P_{PE}^{Al_xGa_{1-x}N} = 2\left(\frac{a_{GaN} - a_{Al_xGa_{1-x}N}}{a_{Al_xGa_{1-x}N}}\right)(e_{31(Al_xGa_{1-x}N)} - e_{33(Al_xGa_{1-x}N)})\frac{C_{13(Al_xGa_{1-x}N)}}{C_{33(Al_xGa_{1-x}N)}} \quad (2.9)$$

The total polarization sheet charge density is defined by:

$$P_{total} = P_{PE}^{Al_xGa_{1-x}N} + \Delta P_{SP}. \quad (2.10)$$

For the Al composition equal to 20 %, P_{total} is $1.13 \times 10^{13} \text{ cm}^{-2}$, which is one order of magnitude higher than the inversion carrier densities at Si and SiC MOS interfaces.

Using In_{0.17}Al_{0.83}N as a barrier layer of HEMTs, the lattice-matched InAlN/GaN heterojunction shows the P_{PE} of zero. However, the higher P_{SP} of the InAlN gives

	C_{33} (GPa)	C_{13} (GPz)	e_{33} (Cm ⁻²)	e_{31} (Cm ⁻²)
GaN	415 ^a	83 ^a	0.65 ^b	-0.33 ^b
AlN	373 ^a	108 ^a	1.55 ^c	-0.58 ^c

^aRef. [11], ^bRef. [12], ^cRef. [13]

Table 2.1. Piezoelectric and elastic constant of GaN and AlN.

the positive ΔP_0 two times higher than in AlGaIn, i.e. $P_{total} = 2.73 \times 10^{13} \text{ cm}^{-2}$. The larger conduction-band offset at the InAlN/GaN interface is also expected to suppress the gate leakage current under a forward gate bias. Kuzmik also mentioned that the piezoelectric polarization of the InGaIn channel layer may realize the much more higher-density 2DEG and the higher band offset as compared with other III-N heterostructures [14].

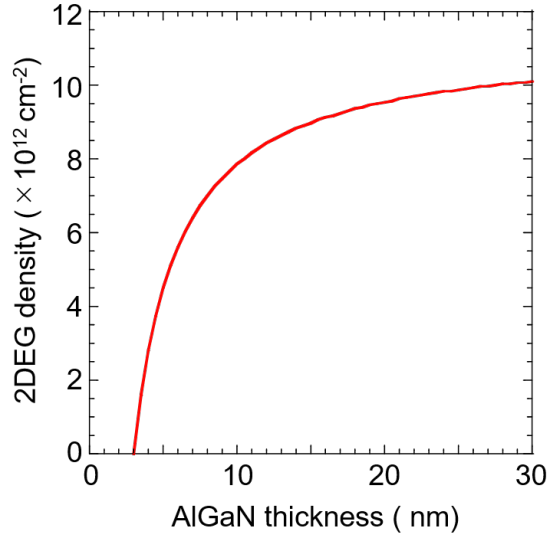


Figure 2.8. Calculated the 2DEG sheet carrier density as a function of Al_{0.20}Ga_{0.80}N barrier thickness.

In the case of the AlGaIn/GaN heterojunction, the P_{SP} is proportional to the Al composition ratio of AlGaIn. The typical Al composition ratio of AlGaIn which is usually used for the HEMTs is around 20–30 %, resulting in the 2DEG density of around 10^{13} cm^{-2} . Figure 2.8 shows the relationship between the 2DEG density and the thickness of AlGaIn with the Al composition ratio of 20 %. Ideally, the 2DEG density increases with the AlGaIn thickness due to the increase of P_{PE} . In the real case, the lattice strain can be relaxed with the thicker growth of AlGaIn, resulting in

the saturation of the 2DEG density. Furthermore, the thinner AlGa_N also relaxes the compression of itself, leading to decrease of P_{PE} . As a consequence, when ΔP_0 is zero, the heterojunction system does not create the 2DEG channel. Therefore in the case of the AlGa_N/Ga_N heterostructure, the 2DEG density can be modulated by the Al composition ration and the thickness of AlGa_N barrier layer.

References

- [1] I. C. Kizilyalli, A. P. Edwards, O. Aktas, T. Prunty, and D. Bour, *IEEE Trans. Electron Devices* **62**, 414 (2015).
- [2] T. Tanaka, N. Kaneda, T. Mishim, Y. Kihara, T. Aoki, and K. Shiojima, *Jpn. J. Appl. Phys.* **54**, 041002 (2015).
- [3] J. A. Freitas, Jr., M. A. Mastro, E. A. Imhoff, M. J. Tadjer, C. R. Eddy, Jr., and F. J. Kub, *J. Cryst. Growth* **312**, 2616 (2010).
- [4] Q. Mao, J. Liu, X. Wu, J. Zhang, C. Xiong, C. Mo, M. Zhang, and F. Jiang, *J. Semicond.* **36**, 093003 (2015).
- [5] H. Fujikura, T. Konno, T. Yoshida, and F. Horikiri, *Jpn. J. Appl. Phys.* **56**, 085503 (2017).
- [6] S. Fujita, *Jpn. J. Appl. Phys.* **54**, 030101 (2015).
- [7] J. Kuzmik, G. Pozzovivo, C. Ostermaier, G. Strasser, D. Pogany, E. Gornik, J.-F. Carlin, M. Gonschorek, E. Feltin, and N. Grandjean, *J. Appl. Phys.* **106**, 124503 (2009).
- [8] F. Medjdoub, J.-F. Carlin, M. Gonschorek, E. Feltin, M. A. Py, D. Ducatteau, C. Gaguire, N. Grandjean, and E. Kohn, *Tech. Dig.-Int. Electron Devices Meet.*, December 2006, p. 1.
- [9] O. Ambacher, J. Smart, J. R. Shealy, N. G. Weimann, K. Chu, M. Murphy, W. J. Schaff, L. F. Eastman, R. Dimitrov, L. Wittmer, M. Stutzmann, W. Rieger, and J. Hilsenbeck, *J. Appl. Phys.* **85**, 3222 (1999).
- [10] J. P. Ibbetson, P. T. Fini, K. D. Ness, S. P. DenBaars, J. S. Speck, and U. K. Mishra, *Appl. Phys. Lett.* **77**, 250 (2000).
- [11] A. Zoroddu, F. Bernardini, and P. Ruggerone, *Phys. Rev. B* **64**, 045208 (2001).
- [12] M. A. Littlejohn, J. R. Hauser, and T. H. Glisson, *Appl. Phys. Lett.* **26**, 625 (1975).
- [13] K. Tsubouchi, K. Sugai, and N. Mikoshiba, *IEEE Ultrason. Symp.* **1**, 375 (1981).

- [14] J. Kuzmik, IEEE Electron Device Lett. **22**, 510 (2011).

Chapter 3

Electronic States at Interface or Surface of Semiconductor

3.1 Introduction

Nowdays, Metal/Semiconductor(M-S), Semiconductor/Semiconductor(S-S), and Insulator/Semiconductor(I-S) interfaces are basic components of semiconductor devices. It is extremely important to control the properties of such interfaces, because they strongly influence the performance of semiconductor devices.

Therefore the purpose of this chapter is to review the present status of the various approaches to understand the Interface states. First a brief survey of the models on Fermi level pinning is presented.

3.2 Fermi level Pinning and it's Origin

The basic idea about band alignment at M-S interface is to align the bands naturally with each other, keeping the energy distance of each band from the vacuum level unchanged at the interface. This is the well-know Mott-Schottky limit. However, in reality a strong tendency of the metal Fermi level aligning with a characteristic energy position, E_0 (see Figure 3.1), of the semiconductor exists, making the value of Schottky barrier heights (SBH) independent or weakly dependent on the metal work function. This is so-called ‘‘Fermi level pinning’’. How strongly the barrier height ϕ_B , depends on the metal work function, ϕ_m , is usually expressed phenomenologically in terms of the interface index S defined by:

$$S = \frac{d\phi_B}{d\phi_m}. \quad (3.1)$$

Using S , SBH can be expressed as:

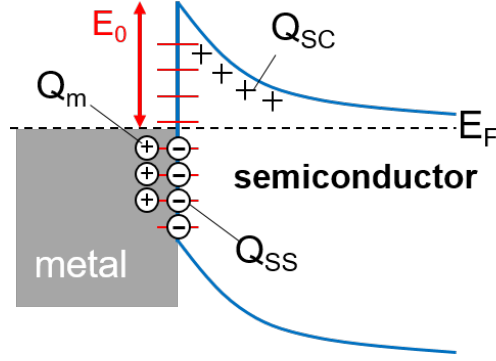


Figure 3.1. Schematic illustration of the Fermi level pinning due to surface states.

$$\phi_B = S(\phi_m - \chi_s) + (1 - S)(E_C - E_0) \quad (3.2)$$

where χ_s is the electron affinity of semiconductor. $S = 1$ corresponds to the Mott Schottky limit and $S = 0$ corresponds to the completely pinned limit (Bardeen limit).

Extensive studies on semiconductor surfaces and interfaces carried out in recent 10–30 years have revealed that Fermi level pinning also exists on free surface, at I-S interfaces and S-S interfaces. In order to explain the origin of Fermi level pinning several models were proposed. In the next sections we will describe all of them briefly.

3.3 Charge neutrality level

Hasegawa et al. [2] stressed that M-S, S-S and I-S interfaces are closely connected with both other through the so-called charge neutrality level (CNL) which can be defined as the boundary energy at which states in the gap state continuum change from a donor-type to acceptor-type character with increasing energy. In a one-dimensional model of a semiconductor, this boundary energy is the branch point energy of the complex band structure [1], and it lies at the midgap. In a three-dimensional crystal, the energy position of CNL can be determined as the zero-point of the cell averaged Green's function [1], as the average hybrid orbital energy position in the tight binding theory of the bands [2], as the midgap point of the dielectric energy gap (dielectric midgap) [3], or as the empirical tight-binding branch-

point energy [4].

The roles of the CNL at the interface are the following: (1) the reference energy for band line-up at the S-S interface (2) the Fermi level pinning point at the M-S interface in the Bardeen limit, and (3) the Fermi level pinning point at the I-S interface. Thus, it is an energy reference point of fundamental importance for interfaces. .

3.4 Metal-induced gap state model (MIGS)

In 1965, V. Heine [5] proposed that the evanescent tails of the wave functions in metals effectively serves interface states and pin the Fermi level (see Figure 3.2). Tersoff [1] later called this type of states as the metal induced gap states (MIGS), and showed the way to calculate the position of the CNL of these states as the pinning point. Fermi level pinning by MIGS is schematically shown in Figure 3.3(a). It should be noted that this model applies only to the pinning at the M-S interface and the pinning should be an intrinsic.

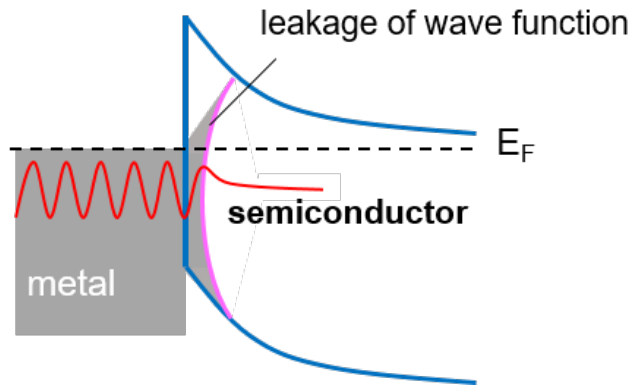


Figure 3.2. Schematic illustration of the MIGS model.

3.5 Disorder-Induced Gap State Model (DIGS)

On the other hand, Hasegawa and Ohno proposed a disorder induced gap state (DIGS) model, in which the disorder of bonds near the interface, caused by the interface formation process, produces an interface state continuum due to incomplete separation of bonding and anti-bonding states [2]. The Fermi level pinning mechanism is similar to that of the MIGS model as shown in Figure 3.3(a). However, the

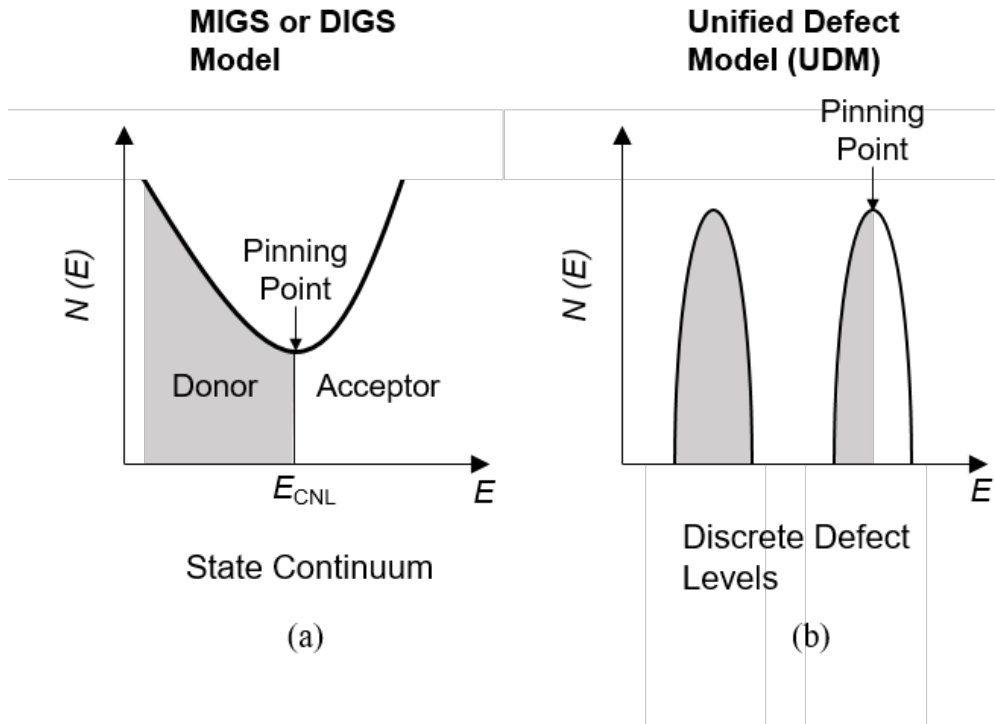


Figure 3.3. Fermi level pinning mechanisms (a) for the MIGS and DIGS models, and (b) for the Unified Defect Model (UDM).

origin of the states is different and that the pinning in the DIGS model is an intrinsic one. Additionally, the DIGS model applies not only to the M-S interface, but also to the free surfaces and the I-S interfaces as well as to defective S-S interfaces.

The primary difference between the MIGS and the DIGS model is that the Fermi level pinning may be avoided or inevitable. In the MIGS model, the pinning is intrinsic one, i.e. due to the simultaneous occurrence of extrinsic defects, the S value can decrease but the pinning does not disappear. On the other hand, in the DIGS model, pinning disappears and the Schottky-Mott limit can be realized if the interface disorder is removed by improving the interface formation process. Teraji and Hara found that the S value could be changed from 0.22 to 0.99 in SiC, and Schottky-Mott extreme of $S=0.99$ by changing the interface formation process [6]. Furthermore, Hasegawa *et al.* conducted a pulse electrochemical process that can form an oxide-free interface without process damage to form metallic dots. As a result, it is possible to get $S=0.4$ in GaAs and InP which are relatively pinning materials with $S \simeq 0.1$, and get $S \simeq 1$ when the dot size is small [7–9].

3.6 Unified defect model (UDM)

As another model of extrinsic pinning, Spicer et al. [10] proposed a unified defect model (UDM) in which near-interface discrete levels on the semiconductor side due to processing induced native defects serve as the pinning states as shown in Figure 3.3(b). The UDM model applies not only to the M-S interface but also to the free surface and I-S interface. The UDM model is a persuasive model but it does not give the experimentally observed pinning positions.

3.7 Influence of interface states at the insulator/GaN interface on the capacitance-voltage behavior of insulator/GaN MOS structures

As was mentioned before, interface states at the I-S interface has serious implications for the performance of GaN based devices. Therefore in the following chapters, we will discuss the influence of the interface states on the GaN MIS structure. Furthermore, we demonstrate a novel method for the control of the interface state densities which was developed in our group in 2017.

3.7.1 Theoretical approach for the simulation of the GaN based MOS C-V characteristics

In this chapter, we introduced the theoretical framework for the modeling of the GaN based MOS C-V characteristics.

During the calculation, two types of the energetic distribution of electronic state density at the Insulator/Semiconductor interface were assumed. One type of $D_{it}(E)$ is a U-shaped distribution in accordance with the DIGS model with donor-like states below the charge neutrality level E_{CNL} and acceptor-like states above it (see Figure 3.4(a)). The density of the states reaches the minimum, denoted D_{it0} , at E_{CNL} , and the full formula for $D_{it}(E)$ is

$$D_{it}^{A,D}(E) = D_{it0} \exp\left[\left(\frac{|E - E_{CNL}|}{E_{0A,0D}}\right)^{n_{A,D}}\right] \quad (3.3)$$

where E_{0A} , n_A , E_{0D} , and n_D describe the curvature of the acceptorlike branch ($E_{CNL} < E < E_C$) and the donorlike one ($E_V < E < E_{CNL}$), respectively.

The other kind of $D_{it}(E)$ is a narrow Gaussian curve describing defect discrete

states (see Figure 3.4(b)),

$$D_{it}^{A,D}{}_{Discrete}(E) = D_{it\ max} \exp\left[-4 \log 2 \left(\frac{E - E_{A,D}}{FWHM}\right)^2\right] \quad (3.4)$$

where $D_{it\ max}$ is the maximum density, $E_{A,D}$ is the energetic location of the level, and FWHM is the full width at half maximum of the Gaussian curve. In GaN, the donorlike discrete state at $E_D = E_C - 0.37$ eV, which is probably related to the N-vacancy defect [11, 12], and the acceptorlike state at $E_A = E_V + 1.0$ eV, which is related to the Ga vacancy [13, 14].

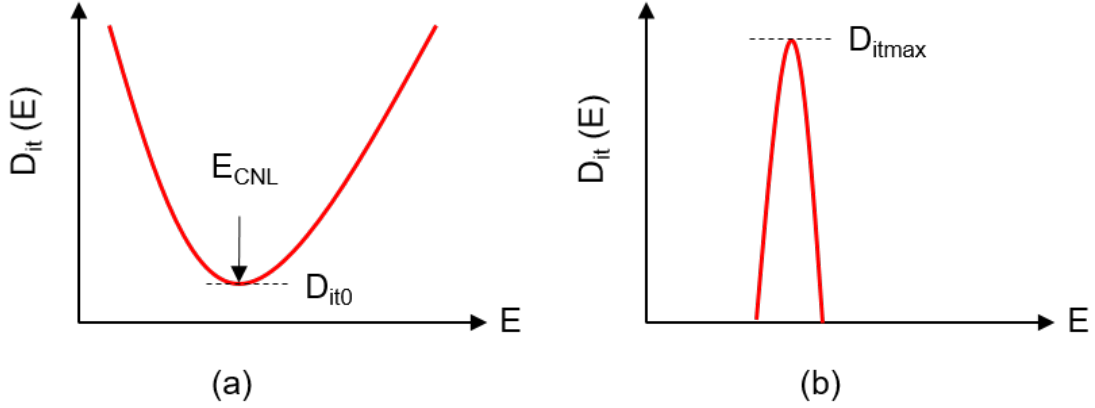


Figure 3.4. Schematic illustration of (a) continuous and (b) discrete level of interface states.

Under the assumption that all interface states are in the thermal equilibrium with the semiconductor, the charge in the interface traps is determined by the Fermi-Dirac distribution $f(E)$:

$$f(E) = \frac{1}{1 + \exp\left(\frac{E - E_C}{kT}\right)} \quad (3.5)$$

where k is the Boltzmann constant, T is temperature, and E_C is the conduction band minimum.

The occupied acceptor-like states produce negative charges, and unoccupied donor-like states produce positive charges. The charge in the interface traps can be expressed using the following formula:

$$Q_{it} = q \int_{E_V}^{E_C} D_{it}^D(E) [1 - f(E)] dE - q \int_{E_V}^{E_C} D_{it}^A(E) f(E) dE, \quad (3.6)$$

where q is the elementary charge, E_V is the valence band maximum, D_{it}^D and D_{it}^A are the density of donor-like and acceptor-like states.

However, eq. 3.6 should be modified in order to consider the slow electron emission from the deep interface traps [15]. Due to the wide bandgap of GaN and AlGaN, the time constant of electron emission from the deep interface states reaches very large values. For example, Figure 3.5 shows the calculated time constant τ as a function of the trap energy E according to the following Shockley-Read-Hall equation:

$$\tau = \frac{1}{N_C \nu \sigma} \exp\left(\frac{E_C - E}{kT}\right). \quad (3.7)$$

where N_C , ν , and σ are the effective density of states in the conduction band, the thermal velocity of electrons, and the capture cross section of the trap, respectively.

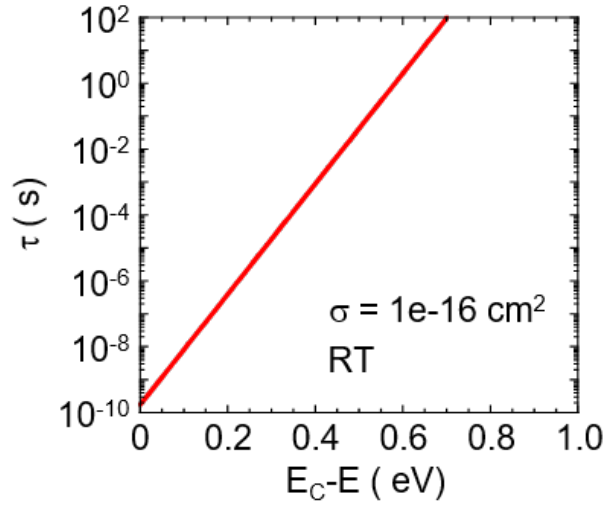


Figure 3.5. Time constant of electron emission from the interface traps to the conduction band.

As can be seen from Figure 3.5, for $E = E_C - 0.7$ eV, τ is approximately equal to 100 s. On the other hand, for $E = E_C - 1.6$ eV (midgap of GaN), τ is estimated to be several years at room temperature. This means that only a limited number of the interface states can be detected during the standard C-V measurements. Therefore it is necessary to take this effect into account to accurately simulate C-V characteristics of GaN based MIS structure. In this order, first we introduced the parameter η_e , which describes the efficiency of electron emission from the trap at energy E . Based on the SRH model, η_e can be calculated as follows:

$$\eta_e = 1 - \exp\left[-t N_C \nu \sigma \exp\left(\frac{E - E_C}{kT}\right)\right]. \quad (3.8)$$

where t is the measurement time. Figure 3.6 shows the calculated η_e as a function of E . It should be noted that the $\eta_e(E)$ is a step like function at RT.

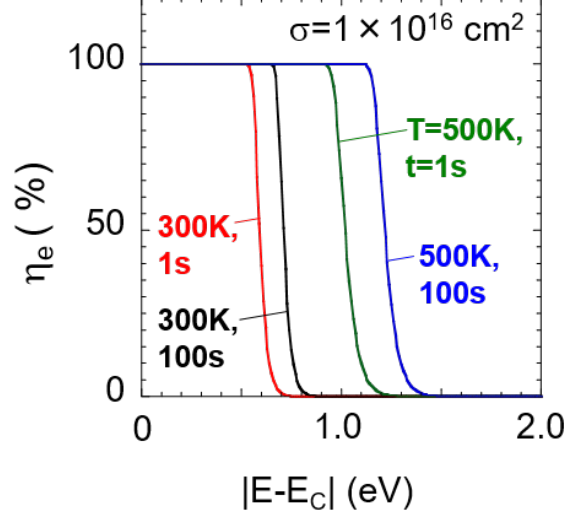


Figure 3.6. Calculated η_e vs trap energy at room temperature and 500K.

Using Equation 3.8 and assuming that the interface states were in equilibrium at zero gate bias and the negative V_G was then applied, the charge in the interface traps should be expressed by

$$Q_{it} = q \int_{E_V}^{E_C} D_{it}^D(E) [1 - f_0(1 - \eta_e) - \eta_e f] dE - q \int_{E_V}^{E_C} D_{it}^A(E) [f_0(1 - \eta_e) + \eta_e f] dE, \quad (3.9)$$

where f_0 and f are the Fermi-Dirac function at zero bias and at the negative bias in question, respectively.

3.8 Theoretical C-V curves of the $\text{Al}_2\text{O}_3/\text{GaN}$ structure

In order to understand C-V behavior of the MOS Insulator/GaN structures, we carried out the theoretical calculations of C-V curves based on solving a Poisson's equation. Among the various high-k gate dielectrics used for GaN MIS-HEMTs, Al_2O_3 is the most commonly applied so far and is one of the most attractive candidates owing to its large bandgap, high dielectric constant and high breakdown field. It should be noted that Hashizume et al. [16] first proposed Al_2O_3 as the gate insulator for GaN MIS-HEMT. Therefore, for the calculations, we chose Al_2O_3 with the bandgap 7 eV as an insulator.

We assumed that in the Al₂O₃ layer the Poisson's equation becomes the Laplace's equation:

$$\frac{d^2V}{dx^2} = 0. \quad (3.10)$$

Furthermore, we assumed that in AlGaN and GaN layers the Poisson's equation takes the following form:

$$\frac{d^2V}{dx^2} = -\frac{q}{\varepsilon_0\varepsilon_{sem}}(N_D - n), \quad (3.11)$$

where $q > 0$ is the elementary charge, ε_0 is the vacuum permittivity, ε_{sem} is the relative permittivity of a semiconductor, n is the electron density and N_D is the concentration of fully ionized donor dopants.

The above equations 3.10–3.11 were solved self-consistently using the finite element SOR method with the following boundary conditions:

- Dirichlet type boundary conditions at the contacts.
- Neumann type boundary conditions at the Al₂O₃/GaN interface determined by the density of the interface state charge (Q_{it}). In particular, the boundary conditions at the Al₂O₃/GaN interface are expressed as:

$$\varepsilon_0\varepsilon_{sem}\frac{dV}{dx}|_{sem} - \varepsilon_0\varepsilon_{ins}\frac{dV}{dx}|_{ins} = Q_{it} + Q_{fix} \quad (3.12)$$

where ε_{ins} is the insulator (Al₂O₃) dielectric constant; Q_{it} and Q_{fix} are the sheet density of the interface trap charge (given by Equation 3.9) and interface fixed charge, respectively.

The solution of model equations are the in-depth distributions $V(x)$ and $n(x)$. The solution was obtained for the bias V_G and $V_G + V_{AC}$, where V_{AC} is the amplitude of the AC signal. On this basis, we calculated the total charge in the whole structure for these biases, i.e., $Q(V_G)$ and $Q(V_G + V_{AC})$ and finally the differential capacitance C using the following formula:

$$C = \frac{Q(V_G) - Q(V_G + V_{AC})}{V_{AC}}. \quad (3.13)$$

Figure 3.7(a) shows the exemplary band diagrams of the Al₂O₃/n-GaN structure, which were calculated using $D_{it}(E)$ from Figure 3.7(b). As can be see from Figure

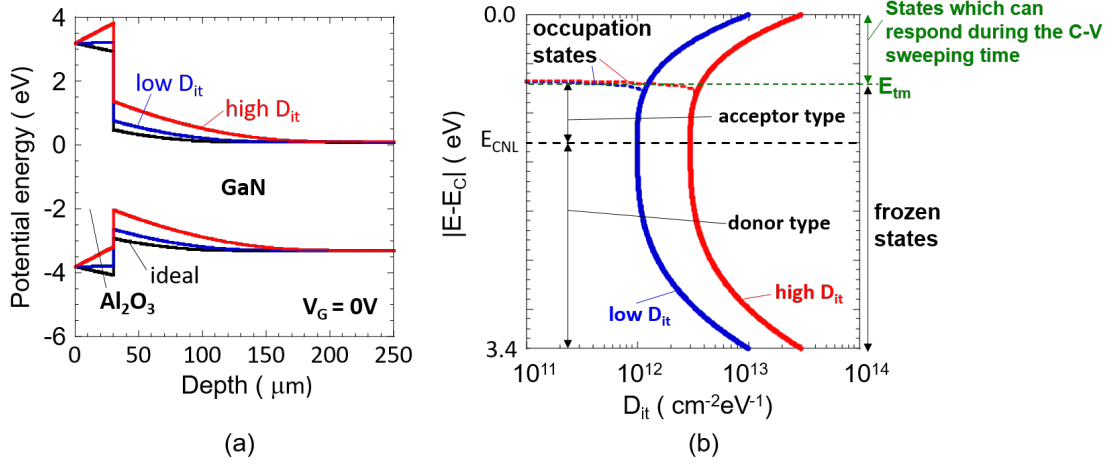


Figure 3.7. (a) Calculated potential distribution of Al₂O₃/n-GaN MOS diode and (b) interface states distributions used in calculation. E_{tm} is the deepest energy of the state which can respond during the C-V sweeping time.

3.7(a) with the increasing D_{it} , the band bending increases because interface state charge become more negative as shown in Figure 3.7(b).

3.8.1 Impact of continuous interface states on the C-V curves

In this section, we study the effect of the continuous interface states on the C-V curves of the Al₂O₃/GaN structure. Figure 3.8 shows theoretical C-V curves of the Al₂O₃/GaN calculated for $D_{it0} = 0$, 10^{12} , and 3×10^{12} eV⁻¹cm⁻² using the parameters show in Table 3.1. All the calculated curves exhibited typical behavior which is observed in the experimental C-V curves of the Al₂O₃/GaN structures [20], i.e. with the increasing interface state density, C-V curves shifts toward positive gate voltage and become more stretch out, as shown in Figure 3.8.

It is obvious that such behavior is due to the (i) change of the interface state charge when the Fermi level E_F is moving between conduction band edge E_C and E_{tm} level (the deepest energy of the state which can respond during the C-V sweeping time, see Figure 3.7(b)) and (ii) “frozen states” (distributed between E_V and E_{tm}) which behave like a fixed charge, i.e. they cannot de-trap electrons during the C-V sweeping at room temperature.

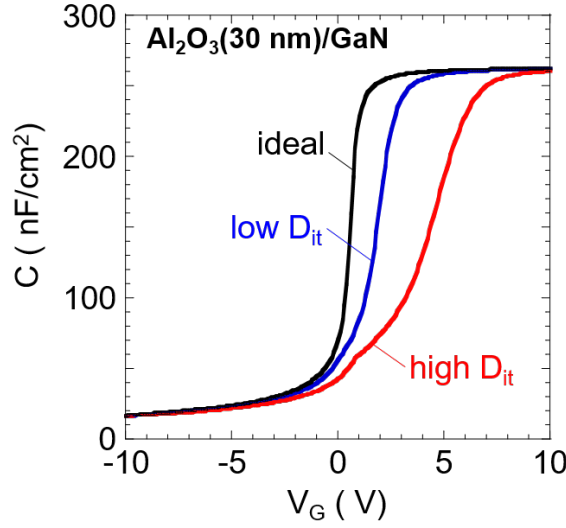


Figure 3.8. Theoretical C-V curves calculated for a Al₂O₃/GaN MOS diode.

Table 3.1. Parameters used in the calculations. m_0 is the mass of a free electron, q is the elementary charge.

Parameter name	Symbol (unit)	Numerical value (material or interface)
Effective mass of electron	m_e/m_0	0.20 (GaN)
Relative permittivity	ϵ	9.5 (GaN) 9.0 (Al ₂ O ₃)
Donor concentration	N_D (cm ⁻³)	5×10^{16}
Surface barrier height	ϕ_s (eV)	3.4 (Ni/Al ₂ O ₃) [17]
Charge neutrality level	E_{CNL}	$E_C - 1.3$ eV (Al ₂ O ₃ /GaN) [18]
Capture cross section of interface states	σ (cm ²)	1×10^{-16} [19]
C-V Measurement duration	t (s)	100

3.8.2 Effect of discrete interface states on the C-V curves

In this section we discuss the influence of the discrete interface states on the C-V curves of the Al₂O₃/GaN structure. Figure 3.9(a) shows theoretical C-V curves of the Al₂O₃/GaN structure calculated assuming the discrete level (shown in Figure 3.9(b)) and parameters from Table 3.1.

As one can see from Figure 3.9(a) acceptor-type discrete level acts like a fixed charge at the Al₂O₃/GaN interface and mainly shift the C-V curve toward a more positive voltages. On the other hand, donor-type discrete level has negligible impact on the C-V curves. It should be noted that such behavior is quite different from that observed in the case of the continuous interface states (see Figure 3.8). This can be explained as follows. Namely as can be see from Figure 3.9(b) the discrete

trap is located relatively deep at $E - E_C \approx 0.5$ eV (around E_{tm} level). Due to that acceptor-like states are almost fully negative ionized during the C-V sweeping time and thus they have significant impact on the C-V curves. On the other hand, donor-like states are almost neutral during the C-V sweeping time and therefore they have negligible effect on the C-V curves.

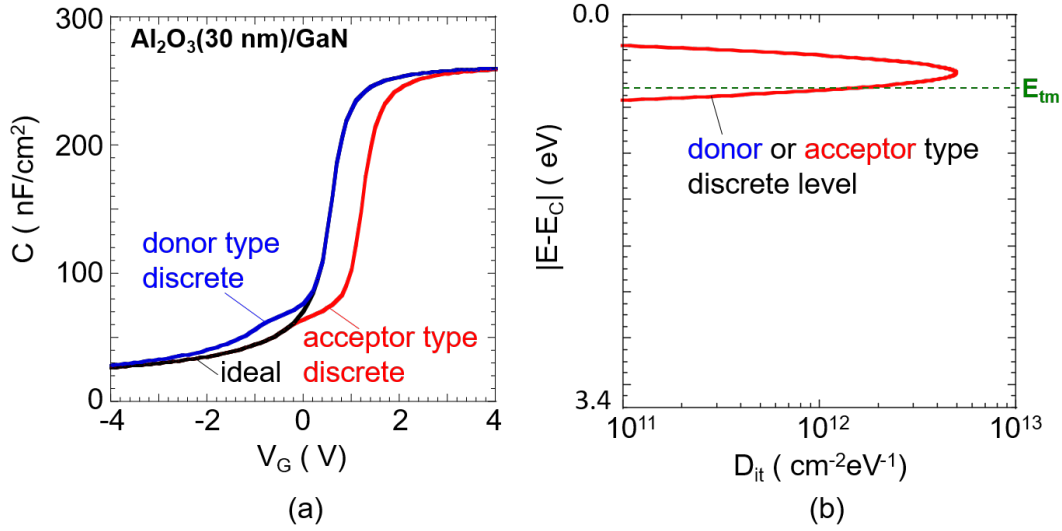


Figure 3.9. (a) Theoretical C-V curves of the $\text{Al}_2\text{O}_3/\text{GaN}$ structure calculated for the discrete level from (b).

3.9 Special Case of Interface States distributed both in energy and space

The frequency dispersion at accumulation bias is a commonly observed feature in the experimental capacitance-voltage (CV) characteristics of MOS structures using GaAs, InP and InGaAs [21–27], as shown in Figure 3.10. To explain this instability behavior, the border trap (BT) model was proposed [29]. This model assumes defect levels inside the gate insulator, as shown in Figure 3.11(a). In this case, BTs have long time constants as they interact with the conduction band electrons via tunneling, leading to large frequency dispersion even at accumulation bias [32, 33]. The disorder-induced gap state (DIGS) model [2, 30], as schematically shown in Figure 3.11(b), can well explain frequency dispersion at accumulation bias. In this model, it is assumed that disordered region at the semiconductor surface includes defects, dangling bonds and lattice displacement (disorder in bond lengths and angles), thereby

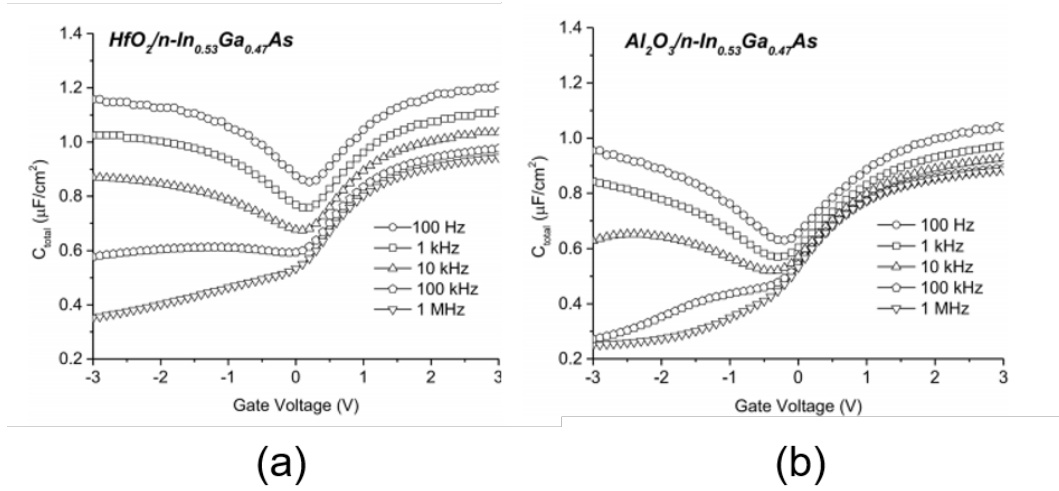


Figure 3.10. C-V characteristics as a function of frequency of (a) HfO_2 and (b) Al_2O_3 on n-InGaAs [28].

producing electronic states with density distributions in both energy and space. When interface states have space distribution, electron capture/emission processes also include tunneling effects. Recently, Galatage et al. [27] reported a comparison of the BT and DIGS models by fitting both models to experimental data. Although both models suggested that frequency dispersion was caused by high density electronic states within 0.8 nm from the crystalline semiconductor surface, they claimed that the experimental capacitance frequency dispersion in accumulation can be well explained by the DIGS model. This led them to conclude that frequency dispersion is indeed due primarily to disorder induced gap states in the semiconductor side. Moreover, since the C-V frequency dispersion in InGaAs MOS structures has been observed for a variety of dielectrics including Al_2O_3 , HfO_2 , ZrO_2 , LaAlO , HfAlO , etc, it is unlikely that the same BT would have almost the same energy from the InGaAs conduction band edge can be consistently reproduced using different dielectric materials.

On the other hand, GaN MIS structures are more stable than other materials such as GaAs. Figure 3.12 shows an $\text{Al}_2\text{O}_3/\text{n-GaN}$ MOS structure prepared by ALD [12]. We used a homo-epitaxial Si-doped GaN layer with a thickness of 4 μm grown on an n^+ -GaN substrate with a relatively low dislocation density ($< 3 \times 10^6 \text{ cm}^{-2}$). The donor density is $6.2 \times 10^{16} \text{ cm}^{-3}$, which was determined by a C-V method using a

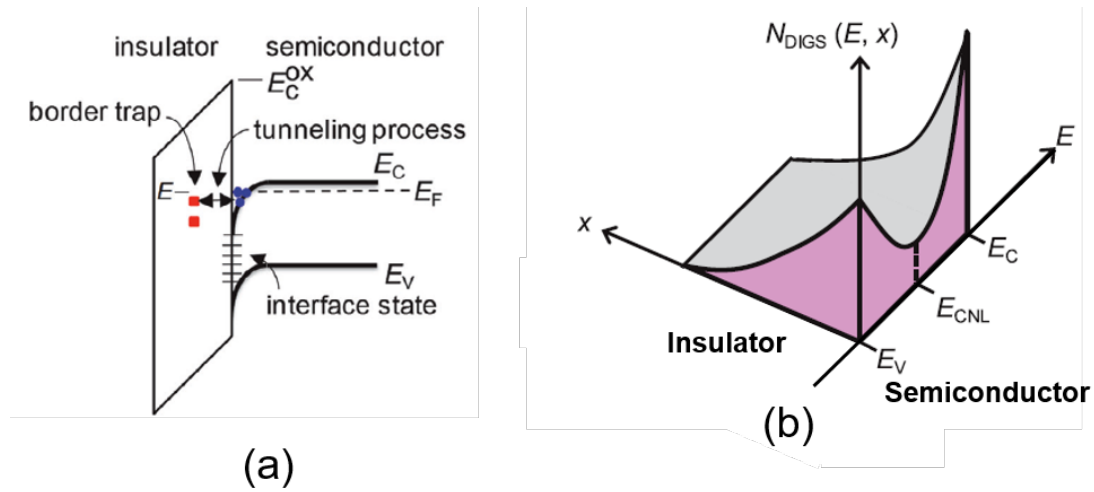


Figure 3.11. Schematic illustrations of (a) border trap (BT) model and (b) disorder-induced gap state (DIGS) model [30, 31].

Schottky diode. After the pre-treatment of the n-GaN surface in a 30%-HF solution for 1min, the Al_2O_3 layer with a nominal thickness of 30 nm was deposited on the n-GaN surface using an ALD system (SUGA-SAL1500) at 350 °C. In the deposition process, water vapor and trimethylaluminum were introduced into a reactor in alternate pulse forms. Each precursor was injected into the reactor for 15 ms, and the purging time was set to 5 s. In this case, the deposition rate is 0.11nm/cycle, indicating the formation of Al_2O_3 in a layer-by-layer fashion. For some samples, a post-deposition annealing was carried out in N_2 for 30 min at 400 °C. A circular Ni/Au (=20/50 nm) with a diameter of 200 μm was deposited on the Al_2O_3 surface as a gate electrode. From an ellipsometry measurement, the refractive index of the ALD Al_2O_3 was estimated to be 1.60 – 1.65, which is close to the values reported for the amorphous Al_2O_3 films prepared by sputtering and ALD methods [34, 35]. Figure 3.13 shows a crosssectional transmission electron microscope (TEM) image of the as-deposited $\text{Al}_2\text{O}_3/\text{GaN}$ interface fabricated on the GaN substrate. The sample has an abrupt and flat interface, indicating low-energy and layer-by-layer characteristics resulting from the ALD process. There is no detectable transition layer like native oxide of GaN at the $\text{Al}_2\text{O}_3/\text{GaN}$ interface. In addition, Al_2O_3 is amorphous and remained unchanged, i.e., no phase transformation even after post-deposition annealing process in the temperature range of 300 - 500 °C. This is consistent with the

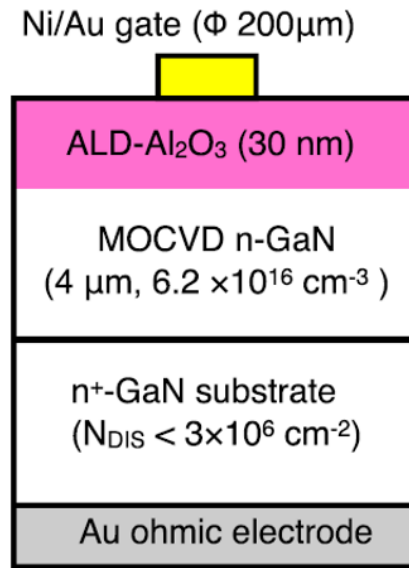


Figure 3.12. Schematic illustration of the $\text{Al}_2\text{O}_3/\text{n-GaN}$ MOS structure fabricated on the GaN substrate.

fact that the phase transformation of Al_2O_3 films from amorphous to crystalline happens at temperature of 800 °C or higher. Figure 3.14 shows the room-temperature

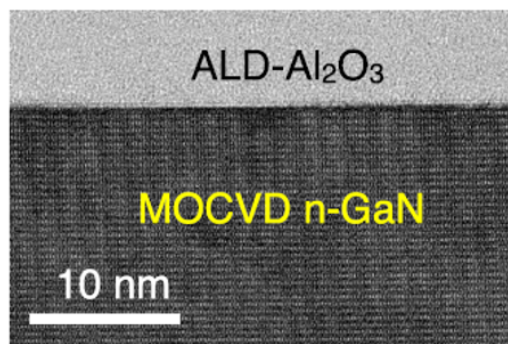


Figure 3.13. Schematic illustration of the $\text{Al}_2\text{O}_3/\text{n-GaN}$ MOS structure fabricated on the GaN substrate.

(RT) C-V characteristics of the as-deposited $\text{Al}_2\text{O}_3/\text{n-GaN}/\text{n}^+\text{-GaN}$ diode (without annealing) in a wide measurement frequency range of 1 Hz to 1 MHz. The sample showed a significant frequency dispersion at reverse bias. By lowering the frequency of the ac measurement signal, deeper interface states are expected to respond accordingly to an ac signal. This allows more of the states to follow the ac frequency

and thereby contribute an additional component to the measured capacitance. Similar frequency dispersions in C-V characteristics were reported for SiO₂/GaN and Al₂O₃/GaN structures [36–38]. In addition, bump-like C-V curves at low frequencies indicate the existence of a discrete level with relatively high density at the GaN surface. Furthermore, it should be noted that Figure 3.14 doesn't show frequency

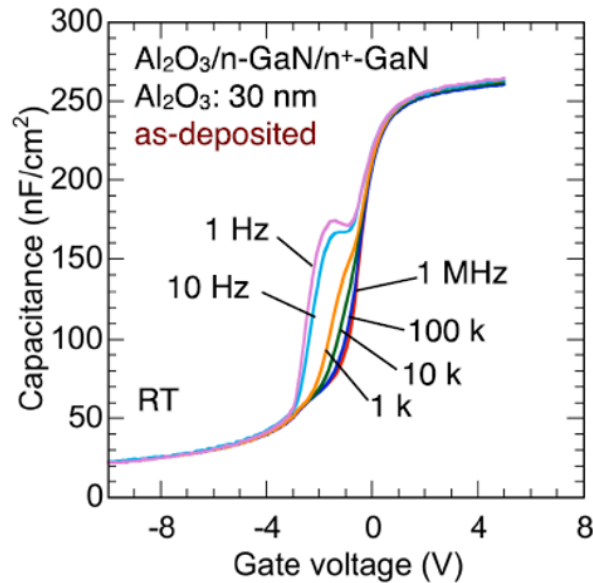


Figure 3.14. Room-temperature (RT) C-V characteristics of MOS diodes fabricated on the GaN substrate without annealing.

dispersion at accumulation bias. It indicates that the Al₂O₃ layer is relatively good quality, i.e. does not exhibit the border traps/interface states near the Al₂O₃/GaN interface.

3.9.1 Conclusion

In this chapter, the history of the model of electric states at metal–semiconductor and insulator–semiconductor interface was described. In particular, we focused on the two fundamental models of interface states, i.e. MIGS and DIGS model.

We explained the primary difference between these two models and we showed why the MIGS model cannot be applied to the Insulator/III-N interfaces. Furthermore, we introduced theoretical approach for the simulations of the GaN based MOS C-V curves. In addition, we performed systematic calculations and analysis of theoretical C-V curve from Al₂O₃/GaN structures assuming different distribution of interface

states at the $\text{Al}_2\text{O}_3/\text{GaN}$ interface.

References

- [1] J. Tersoff, Phys. Rev. Lett. **52**, 465 (1984).
- [2] H. Hasegawa and H. Ohno, J. Vac. Sci. Technol. **B4**, 1130 (1986).
- [3] M. Cardona and N. E. Christensen, Phys. Rev. B **35**, 6182 (1987).
- [4] W. Mönch, J. Appl. Phys. **80**, 5076 (1996).
- [5] V. Heine, Phys. Rev. **138**, A1689 (1965).
- [6] T. Teraji and S. Hara, Phys. Rev. **B70**, 035312 (2004).
- [7] H. Hasegawa, T. Sato and C. Kaneshiro, J. Vac. Sci. Technol. **B17**, 1856 (1999).
- [8] T. Sato, S. Kasai and H. Hasegawa, Appl. Surf. Sci. **175/176**, 181 (2001).
- [9] H. Hasegawa, T. Sato and S. Kasai, Appl. Surf. Sci. **166**, 92 (2000).
- [10] W. E Spicer, I. Lindau, P. R. Skeath and C. Y. Su, J. Vac. Sci. Technol. **17**, 1019 (1980).
- [11] E. Yamaguchi and M. R. Junnarkar, J. Cryst. Growth **189-190**, 570 (1998).
- [12] J. Kotani, S. Kasai, T. Hashizume, and H. Hasegawa, J. Vac. Sci. Technol. B **23**, 1799 (2005).
- [13] J. Neugebauer and C. G. Van de Walle, Appl. Phys. Lett. **69**, 503 (1996).
- [14] U. Kaufmann, M. Kunzer, H. Obloh, M. Maier, Ch. Manz, A. Ramakrishnan, and B. Santic, Phys. Rev. B **59**, 5561 (1999).
- [15] W. Shockley and W. T. Read, Phys. Rev. **87**, 835 (1952); R. N. Hall, *ibid.* **87**, 387 (1952).
- [16] T. Hashizume, S. Ootomo, T. Inagaki, and H. Hasegawa, J. Vac. Sci. Technol. B **21**, 1828 (2003).
- [17] E. Bersch, S. Rangan, and R. A. Bartynski, Phys. Rev. B **78**, 085114 (2008).
- [18] W. Mönch, J. Appl. Phys. **109**, 113724 (2011).
- [19] M. Miczek, C. Mizue, T. Hashizume, and B. Adamowicz, J. Appl. Phys. **103**, 104510 (2008).
- [20] S. Kaneki, J. Ohira, S. Toiya, Z. Yatabe, J. T. Asubar, and T. Hashizume,

- Appl. Phys. Lett. **109**, 162104 (2016).
- [21] H. Hasegawa and T. Sawada, IEEE Trans. Electron Devices **27**, 1055 (1980).
- [22] C. L. Hinkle, A. M. Sonnet, M. Milojevic, F. S. Aguirre-Tostado, H. C. Kim, J. Kim, R. M. Wallace, and E. M. Vogel, Appl. Phys. Lett. **93**, 113506 (2008).
- [23] R. V. Galatage, H. Dong, D. M. Zhernokletov, B. Brennan, C. L. Hinkle, R. M. Wallace, and E. M. Vogel, Appl. Phys. Lett. **99**, 172901 (2011).
- [24] Y. Xuan, Y. Q. Wu, H. C. Lin, T. Shen, and P. D. Ye, IEEE Electron Device Lett. **28**, 935 (2007).
- [25] N. Goel, P. Majhi, W. Tsai, M. Warusawithana, D. G. Schlom, M. B. Santos, J. S. Harris, and Y. Nishi, Appl. Phys. Lett. **91**, 093509 (2007).
- [26] S. Kovesnikov, N. Goel, P. Majhi, H. Wen, M. B. Santos, S. Oktyabrsky, V. Tokranov, R. Kambhampati, R. Moore, F. Zhu, J. Lee, and W. Tsai, Appl. Phys. Lett. **92**, 222904 (2008).
- [27] R. V. Galatage, D. M. Zhernokletov, H. Dong, B. Brennan, C. L. Hinkle, R. M. Wallace, and E. M. Vogel, J. Appl. Phys. **116**, 014504 (2014).
- [28] G. Jiao, C. Yao, Y. Xuan, D. Huang, P. D. Ye, and M.-F. Li, IEEE Trans. Electron Devices **59**, 1661 (2012).
- [29] Y. Yuan, L. Wang, B. Yu, B. Shin, J. Ahn, P. C. McIntyre, P. M. Asbeck, M. J. W. Rodwell, and Y. Taur, IEEE Electron Device Lett. **32**, 485 (2011).
- [30] L. He, H. Hasegawa, T. Sawada, and H. Ohno, J. Appl. Phys. **63**, 2120 (1988).
- [31] Z. Yatabe, J. T. Asubar, and T. Hashizume, J. Appl. D **49**, 393001 (2016).
- [32] H.-P. Chen, Y. Yuan, B. Yu, J. Ahn, P. C. McIntyre, P. M. Asbeck, M. J. W. Rodwell, and Y. Taur, IEEE Trans. Electron Devices **59**, 2383 (2012).
- [33] G. Brammertz, A. Alian, D. H.-C. Lin, M. Meuris, M. Caymax, and W.-E. Wang, IEEE Trans. Electron. Devices **58**, 3890 (2011).
- [34] Y. Jin, K. Saito, M. Shimada, and T. Ono, J. Vac. Sci. Technol., B **21**, 942 (2003).
- [35] S. K. Kim, S. W. Lee, C. S. Hwang, Y. S. Min, J. Y. Won, and J. Jeong, J. Electrochem. Soc. **153**, F69 (2006).
- [36] B. Gaffey, L. J. Guido, X. W. Wang, and T. P. Ma, IEEE Trans. Electron Devices **48**, 458 (2001).

- [37] K. Matocha, R. J. Gutmann, and T. P. Chow, *IEEE Trans. Electron Devices* **50**, 1200 (2003).
- [38] R. D. Long, A. Hafez, M. Gunji, Y. Nishi, and P. C. McIntyre, *Appl. Phys. Lett.* **101**, 241606 (2012).

Chapter 4

Evaluation of surface charging at AlGa_N surface using a dual-gate structure

4.1 Background

In “Introduction”, the background of this chapter was described. However, in this chapter, the background is rewritten more precisely.

There are several remaining stability issues impeding the widespread deployment of GaN-based devices. One of the major concern is the current collapse phenomenon which is the temporary reduction of drain current following the application of high voltage and/or high power at both on- and off-state operations [1, 2]. According to the most widely accepted “virtual gate” model proposed by Vetury et al. [2], current collapse is mainly due to surface charging at a portion of the gate-drain (G-D) access region immediately close to the gate edge. On the basis of the gate injection and surface hopping model [3, 4] illustrated in Figure 4.1, electron conduction via trap-to-trap hopping can be promoted with the application of increasing drain voltage. Consequently, this may lead to the widening of the “virtual gate” from the gate edge until some further distance on the G-D access region. Using Kelvin probe force microscopy, several groups reported the changes in surface potential of AlGa_N due to surface trap occupancy in the G-D access region after applying an off-bias stress to the AlGa_N/Ga_N HEMTs [6–10]. In addition, it has recently been demonstrated that trapping can extend as far as several hundred nanometers from the drain-side gate edge [9, 10]. However, there have been few reports on the effects of spatially induced surface charging on the current-voltage ($I - V$) characteristics of AlGa_N/Ga_N HEMTs.

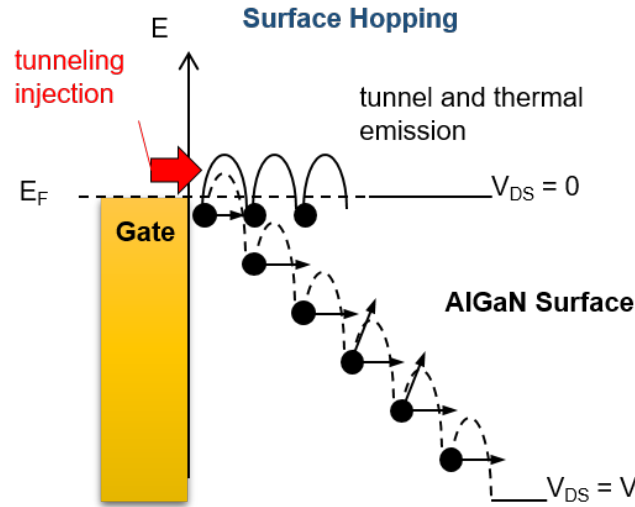


Figure 4.1. Gate injection and surface hopping model [5].

Accordingly in one of our previous works [11], we investigated the effect of local bias stress on access regions of AlGa_N/Ga_N HEMTs using a dual-gate structure. In this present communication, using the similar dual-gate architecture, we extend our investigation to the effect of pulsed bias stress on the $I - V$ characteristics under which power devices in power inverter circuits are normally subjected to. The dual-gate structure enables us to characterize the effects on the $I - V$ characteristics of AlGa_N/Ga_N HEMTs of spatially induced surface charging on the access region from the gate edges to the drain and source electrodes. We also probe the possibility that surface charging immediately adjacent to the gate may also lead to threshold voltage (V_{TH}) shift.

4.2 Device structure and fabrication process

Figure 4.2 shows a schematic illustration of a dual-gate AlGa_N/Ga_N HEMT used in this study. The gate length (L_G) and width (W_G) are 1.0 and 60 μm , respectively. The G1-G2 inter-gate distance is 0.5 μm . We used an Al_{0.25}Ga_{0.75}N/Ga_N heterostructure grown on a sapphire substrate by metal-organic chemical vapor deposition. The thicknesses of Ga_N and AlGa_N layers are 2 μm and 25 nm, respectively. Typical values of the carrier concentration and the sheet resistance are $9.0 \times 10^{12} \text{cm}^{-2}$ and 470 Ω/sq , respectively. The device isolation was carried out by reactive ion-beam etching assisted with electron-cyclotron-resonance plasma using

a gas mixture of $\text{CH}_4/\text{H}_2/\text{Ar}/\text{N}_2$. As drain and source electrodes, Ti/Al/Ti/Au (=30/50/20/100 nm) metal stack was deposited, followed by rapid thermal annealing (RTA) at 800 °C for 1 min. Finally, Ni/Au (=30/50 nm) bilayer was deposited to form the Schottky gates. No surface passivation was employed in the dual-gate HEMTs.

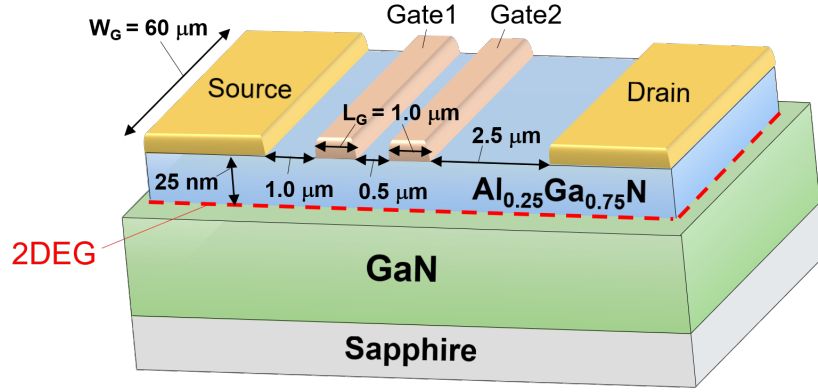


Figure 4.2. Dual-gate AlGaN/GaN HEMT structure.

The $I - V$ characteristics were measured using an Agilent B1500A precision semiconductor device parameter analyzer. For investigating the effect of pulsed voltage stress on the DC $I - V$ characteristics, Agilent E5250A low-leakage switch mainframe was employed for switching the semiconductor pulse generator unit (SPGU) and the source measure unit (SMU) signals of the B1500A semiconductor device parameter analyzer. Band diagram simulations were performed using a SILVACO ATLAS 2D finite element simulator.

4.3 Results and discussions

4.3.1 Typical I-V characteristics of dual-gate HEMTs

Figure 4.3 shows the typical drain $I - V$ and transfer characteristics of the dual-gate AlGaN/GaN HEMT driven using either G1 and G2. During each measurement, while one gate was used for the driving the device, the other gate was kept floating. Both gates satisfactorily control the drain current. As shown in Figure 4.3(b), we observed equal values of V_{TH} for G1- and G2-gate driving operations. On the other hand, higher values of drain current and transconductance were obtained when the device was driven using G1. As shown in Figure 4.2, the effective length of the G-S

access region for G1 operation is less than that for G2 operation. This relationship leads to a smaller parasitic source access resistance for G1 operation [12,13], resulting in the observed higher values of drain current and transconductance.

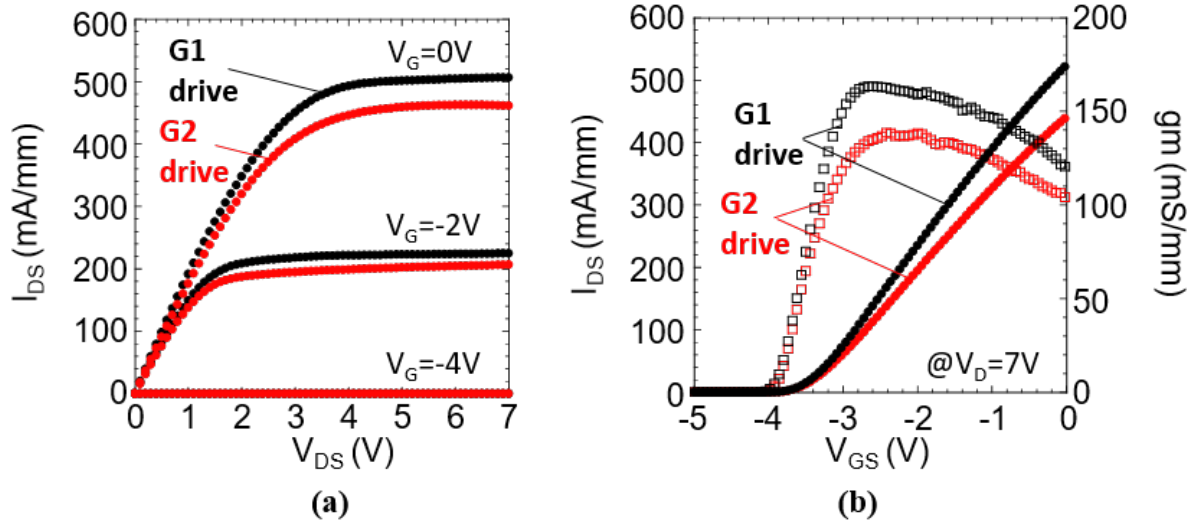


Figure 4.3. Dual-gate AlGaIn/GaN HEMT structure.

4.3.2 Pulse measurements of I_D - V_D characteristics

Next, driving the device using G1, conventional pulsed $I - V$ measurements were performed using three quiescent bias (QB) points, namely: $QB_0 = (V_{DSQ0}, V_{GSQ0}) = (0 V, 0V)$, $QB_1 = (V_{DSQ1}, V_{GSQ1}) = (0 V, -5V)$, $QB_2 = (V_{DSQ2}, V_{GSQ2}) = (10 V, -5 V)$. The QB_1 and QB_2 points applied off-stress bias without and with the drain voltage, respectively, to the device. The pulse width is $5 \mu s$ while the pulse period is $500 \mu s$ for these measurements giving a duty cycle of 1%. Figure 4.4 compares the pulsed $I - V$ curves obtained using these three QB points. The $I_D - V_{DS}$ curve obtained using QB_0 can be considered as the equilibrium or un-stressed $I_D - V_{DS}$ curve and therefore can serve as the reference $I - V$ curve. At quiescent bias point QB_1 , a relatively high electric field is concentrated at both gate edges, resulting in surface charging on both the G-D and G-S access regions. Accordingly, this increased the drain and source access resistances, and induced the drain current reduction, as shown in Figure 4.4. For quiescent bias point QB_2 , while the G-S region is similarly stressed as in QB_1 , the G-D region is subjected to a more severe stress due to the

positive drain voltage. This higher bias stress on the G-D region can lead to the larger drain access resistance, resulting in the significant increase in R_{ON} evident in Figure 4.4. These results indicate that the off-state pulse stress clearly induces "current collapse" due to the surface charging at the access region [14, 15].

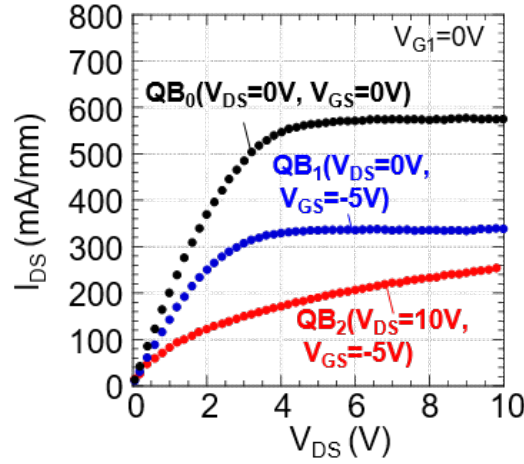


Figure 4.4. Pulsed $I-V$ curves obtained using three quiescent bias (QB) points under the G1 drive.

To imitate a typical voltage stress under which devices in power switching circuits are normally subjected to, we applied a voltage stress consisting of pulsed $V_{GS_{stress}}$ train alternating between -5V (pinch-off state) and -2V (on-state) on a particular gate simultaneously with a constant drain voltage $V_{DS_{stress}}$ of 15 V for 10 s, as illustrated in Figure 4.5. Immediately after applying the pulsed stress to one of the gates, with $V_{GS} = -2$ V applied on the other gate, the resulting after stress DC $I_D - V_{DS}$ curve was measured by sweeping the drain to source voltage from 0 to 20 V. Agilent E5250A low-leakage switch mainframe was employed for switching from the stress mode to the measurement mode.

4.3.3 G2-stress/G1-drive scheme and G1-stress/G2-drive scheme

For this particular experiment, we performed two sets of "stressed" $I_D - V_{DS}$ measurements, namely: (1) G2-stress/G1-drive scheme, where G2 was used for stressing the device while G1 was used for the following driving the device, and (2) G1-stress/G2-drive scheme, where G1 was used for stressing the device while G2 was used for driving the device, as shown in Figures 4.6(a) and 4.7(a). Figures 4.6(b)

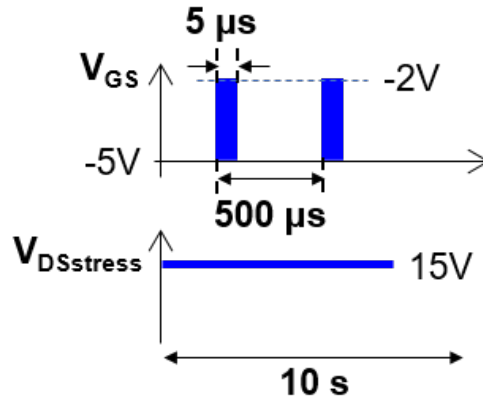


Figure 4.5. Pulsed gate voltage stress applied simultaneously with a constant drain voltage $V_{DSstress}$.

and 4.7(c) compare the results of these two sets of measurements. It should be emphasized that these measurement schemes differ in what region (G-D or G-S access region) is stressed. Stressing the device using G2 (scheme 1) promotes surface charging near G2. In this case, due to the device layout, the increment in access resistances is effectively confined on the drain side of driving gate G1, as schematically indicated by the inset of Fig. 5(b). Therefore, G2 stress effectively only increased R_{ON} and have no effect on the saturation drain current (I_{DSS}). On the other hand, G1 stress promotes the increase of a source access resistance when the device is driven by the G2 gate. This resulted in the observed significant decrease in I_{DSS} , as shown in Figure 4.7(c).

Following the same configuration as in the G1-stress/G2-drive scheme, we then examined the change in transfer characteristics. As seen in **Fig. 6**, the V_{TH} shifts towards the positive voltage direction upon increasing the $V_{DSstress}$. There is a possibility that the observed V_{TH} shift can occur due to surface charging near the G2 edge on the source side (G1 side). It is likely that stressing G1 induced surface charging on the access region as far as $0.5 \mu\text{m}$ from the G1 edge reaching the G2 edge. This extent of surface charging due to bias stress is not remote, for instance, as demonstrated in Refs. [9] and [10]. To shed a light on this, we then carried out a 2D potential simulation using the SILVACO ATLAS 2D finite element simulator. In this case, we assumed negative surface charges with densities ranging from 1×10^{12} to $1 \times 10^{13} \text{ cm}^{-2}$ uniformly distributed on the AlGaIn surface between G1 and G2.

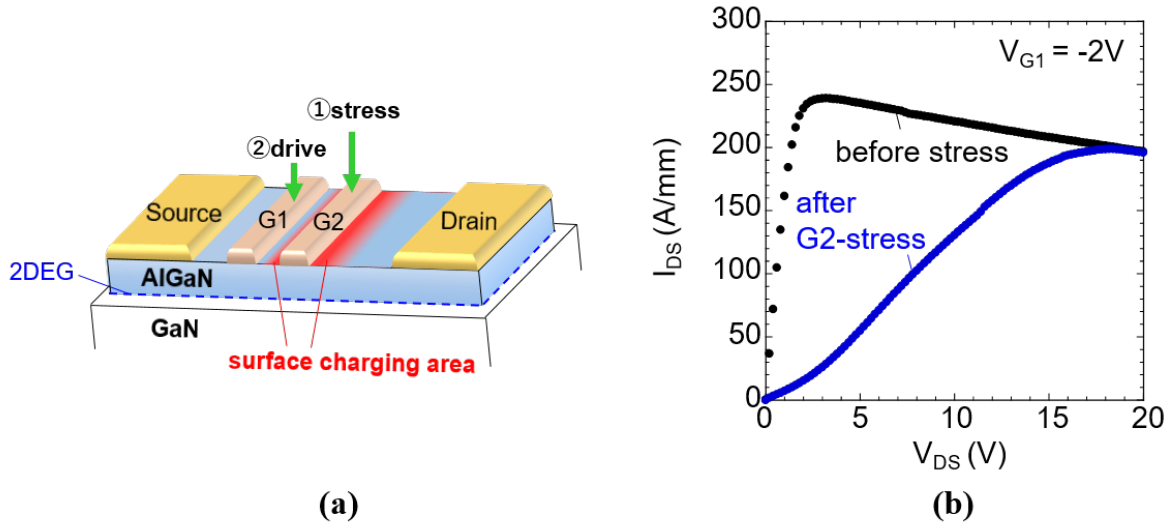


Figure 4.6. (a) Schematic illustration of G2-stress/G1-drive scheme and (b) I_{DS} - V_{DS} curves before and after the pulsed voltage stress for G2-stress/G1 drive.

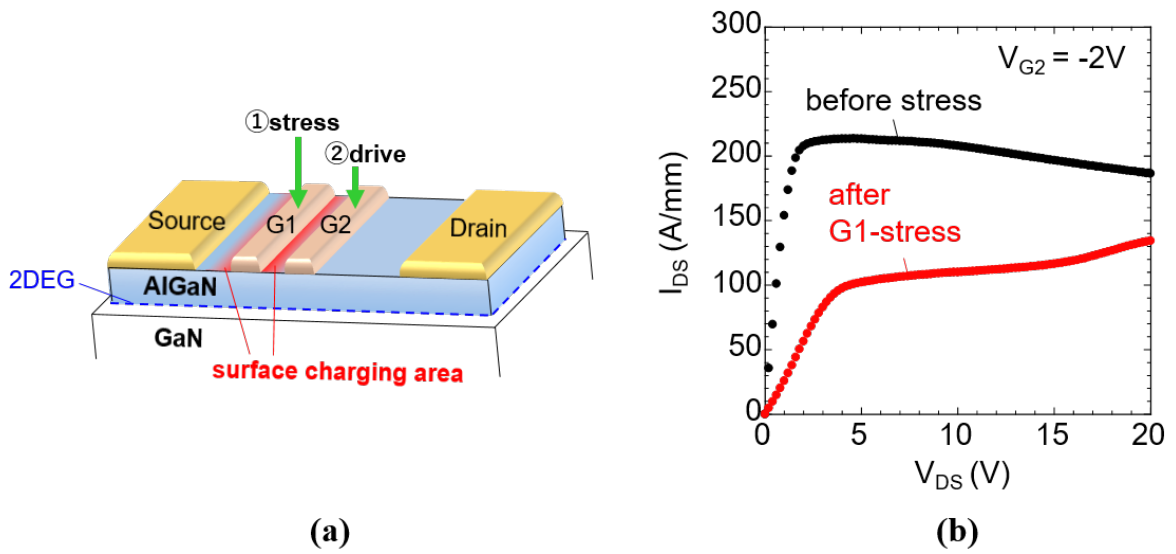


Figure 4.7. (a) Schematic illustration of G1-stress/G2-drive scheme and (b) I_{DS} - V_{DS} curves before and after the pulsed voltage stress for G1-stress/G2-drive.

For calculation, we used structural and size parameters in consistent with those shown in Figure 4.2. We calculated under the “simulation line” as shown in Figure 4.9(a). In addition, an Al composition of 0.25 in AlGa_N, a two-dimensional electron gas (2DEG) density of 9×10^{12} cm⁻², a conduction band offset of 0.36 eV and a Schottky barrier height of 1.4 eV were also used in the calculation.

Figure 4.9(b) shows 2D potential distribution near the G2 edge on the source side

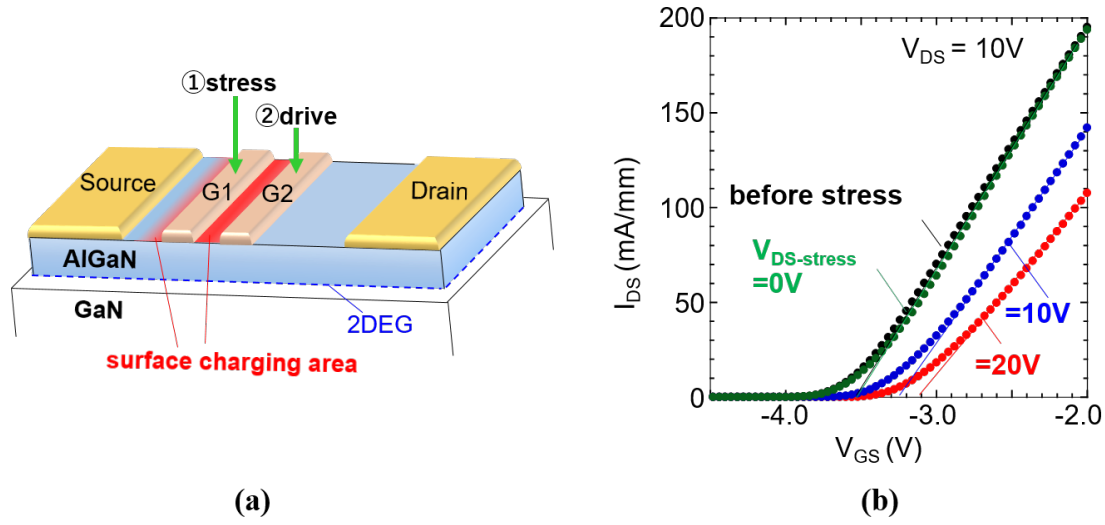


Figure 4.8. Schematic illustration of G1-stress/G2-drive scheme and (b) transfer characteristics before and after the pulsed stress for the G1-stress/G2-drive scheme.

(G1 side). These negative surface charges mimic the role of the trapped electrons on the AlGa_N surface due to G1 stress in the physical experiment. It is clearly seen that surface negative charges with a density of $5 \times 10^{12} \text{ cm}^{-2}$ modulate the potential distribution in the AlGa_N barrier layer near the G2 edge, extending as far as under the G2 itself. The influence of such negative surface charges on the AlGa_N/Ga_N energy band diagram profile is probed along two cutlines, line A and line B illustrated in Figure 4.9(b). As expected and presented in Figure 4.9(c), the negative surface charges have no significant effect on the band diagram profile of the AlGa_N/Ga_N heterostructure along cutline A which is 30 nm away from the G2 edge. This is, in fact, the same with the energy band diagram of a Schottky junction under zero bias. Interestingly, however, along cutline B, the potential profile near the surface of the AlGa_N barrier layer is apparently bended and lifted up in a manner shown in Figure 4.9(d). Consequently, this may lead to a decreased 2DEG concentration in this region and eventually shifting of the V_{TH} towards positive voltage direction. In fact, the calculation showed a 2DEG density of $7.5 \times 10^{12} \text{ cm}^{-2}$ along line A, which is smaller than $9.0 \times 10^{12} \text{ cm}^{-2}$ along line B. This result also lends credence to the earlier supposition that surface charging can extend as far as $0.5 \mu\text{m}$ from the stressing gate edge. From the calculation, we found that no significant potential modulation occurred at the G2 edge when assuming values of surface charge density

less than $2 \times 10^{12} \text{ cm}^{-2}$. As expected, on the other hand, the higher density of surface charges induces more pronounced potential modulation in the AlGa_{0.25}N layer. Our recent work [16] showed electronic states with densities ranging from 1×10^{12} to $3 \times 10^{12} \text{ cm}^{-2}$ at Al₂O₃/AlGa_{0.25}N interfaces near the conduction band edge. Since it is expected that unpassivated AlGa_{0.25}N surfaces (present case) have the higher surface state densities than the passivated surface, the surface charge density of $5 \times 10^{12} \text{ cm}^{-2}$ used in the calculation indicates a possible density of electronic states on unpassivated AlGa_{0.25}N surfaces.

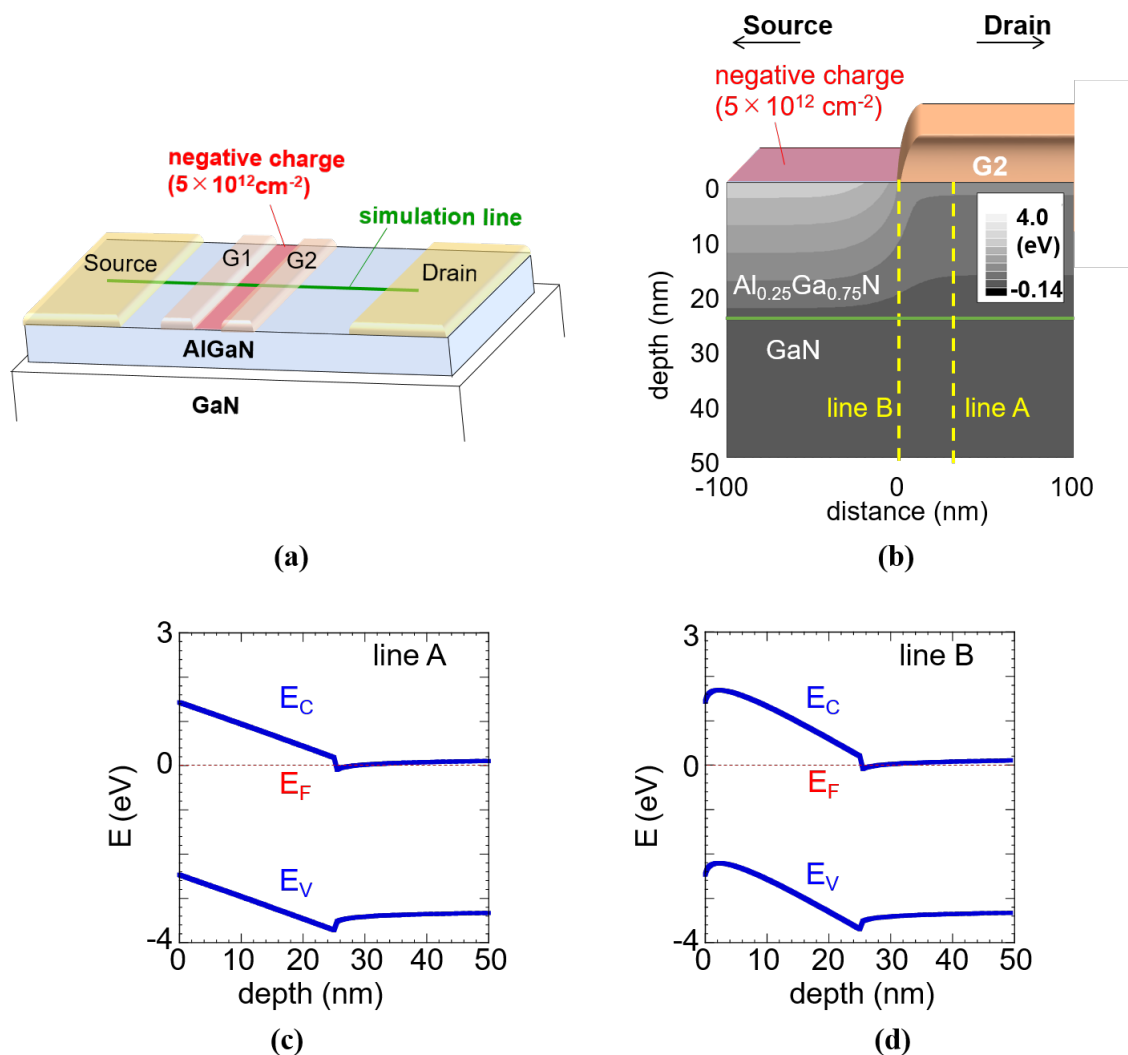


Figure 4.9. (a) Indicate the “simulation line” at the dual-gate AlGa_{0.25}N/GaN HEMT. (b) Calculated 2D potential distribution near the G2 edge on the source (G1) side. Band diagram of the AlGa_{0.25}N/GaN heterostructure along (c) cutline A and (d) cutline B.

In the G2-stress/G1-drive scheme corresponding to the $I_{DS} - V_{DS}$ curves in Figure 4.6(b), on the other hand, no V_{TH} shift was observed. The electric field on the gate edge of the source side is much lower than that on the drain side. Thus stressing G2 induced a weak extension of surface charging on the source side, as schematically shown in Figure 4.6(a). Therefore, the surface charging region is sufficiently far from the G1 edges, leading to no V_{TH} shift during G1 drive operation after the G2 stress. The calculation indicates that no significant potential modulation occurs when the surface charging region is 50 nm far from the gate edge, even though the surface charge density is $5 \times 10^{12} \text{ cm}^{-2}$ or higher.

4.4 Conclusion

In summary, we have evaluated off-bias-stress spatially induced surface charging effects using a dual-gate HEMT structure. Pulsed voltage stress on the G-D access region leads only to increase in R_{ON} of the device. On the other hand, pulsed voltage stress on the G-S region leads not only to increase in R_{ON} but also to decrease in I_{DSS} . In the case of the G1-stress/G2-drive operation, we observed a clear V_{TH} shift towards the positive voltage direction upon increasing the $V_{DS\text{stress}}$. The 2D potential simulation indicated that surface negative charges induced by the G1 stress modulate the potential distribution in the AlGaIn barrier layer near the G2 edge where the potential near the surface of the AlGaIn barrier layer are apparently bended and lifted. Consequently, this may lead to a decreased 2DEG concentration in this region and eventually shifting of the V_{TH} towards positive voltage direction. It was also found that such surface charging can extend as far as $0.5 \mu\text{m}$ from the stressing gate edge. For accrual device technology, we will have to investigate effects of a surface passivation [17] and/or a field plate structures [18,19] on surface charging region at the AlGaIn surface.

References

- [1] M. A. Khan, M. S. Shur, Q. C. Chen, and J. N. Kuznia, *Electron. Lett.* **30**, 2175 (1994).
- [2] R. Vetry, N. Q. Zhang, S. Keller, and U. K. Mishra, *IEEE Trans. Electron Devices* **48**, 560 (2001).
- [3] R. J. Trew, D. S. Green, and J. B. Shealy, *IEEE Microwave Mag.* **10** [4], 116 (2009).
- [4] J. Kotani, M. Tajima, S. Kasai, and T. Hashizume, *Appl. Phys. Lett.* **91**, 093501 (2007).
- [5] U. K. Mishra, L. Shen, T. E. Kazior, and Y.-F. Wu, *Proc. IEEE* **96**, 287 (2008).
- [6] G. Koley, V. Tilak, L. F. Eastman, and M. G. Spencer, *IEEE Trans. Electron Devices* **50**, 886 (2003).
- [7] K. Nakagami, Y. Ohno, S. Kishimoto, K. Maezawa, and T. Mizutani, *Appl. Phys. Lett.* **85**, 6028 (2004).
- [8] S. Kamiya, M. Iwami, T. Tsuchiya, M. Kurouchi, J. Kikawa, T. Yamada, A. Wakejima, H. Miyamoto, A. Suzuki, A. Hinoki, T. Araki, and Y. Nanishi, *Appl. Phys. Lett.* **90**, 213511 (2007).
- [9] S. DasGupta, L. B. Biedermann, M. Sun, R. Kaplar, M. Marinella, K. R. Zavadil, S. Atcitty, and T. Palacios, *Appl. Phys. Lett.* **101**, 243506 (2012).
- [10] D. W. Cardwell, A. R. Arehart, C. Poblenz, Y. Pei, J. S. Speck, U. K. Mishra, S. A. Ringel, and J. P. Pelz, *Appl. Phys. Lett.* **100**, 193507 (2012).
- [11] M. Tajima and T. Hashizume, *Jpn. J. Appl. Phys.* **50**, 061001 (2011).
- [12] S. Russo and A. D. Carlo, *IEEE Trans. Electron Devices* **54**, 1071 (2007).
- [13] C. Y. Lu, E. B. Treidel, O. Hilt, R. Lossy, N. Chaturvedi, E. Y. Chang, J. Würfl, and G. Tränkle, *Semicond. Sci. Technol.* **25**, 075005 (2010).
- [14] G. Meneghesso, F. Rampazzo, P. Kordoš, G. Verzellesi, and E. Zanoni, *IEEE Trans. Electron Devices* **53**, 2932 (2006).

-
- [15] G. Meneghesso, G. Verzellesi, F. Danesin, F. Rampazzo, F. Zanon, A. Tazzoli, M. Meneghini, and E. Zanoni, *IEEE Trans. Device Mater. Reliab.* **8**, 332 (2008).
 - [16] C. Mizue, Y. Hori, M. Miczek, and T. Hashizume, *Jpn. J. Appl. Phys.* **50**, 021001 (2011).
 - [17] T. Hashizume, S. Ootomo, T. Inagaki, and H. Hasegawa, *J. Vac. Sci. Technol. B* **21**, 1828 (2003).
 - [18] S. Karmalkar and U. K. Mishra, *IEEE Trans. Electron Devices* **48**, 1515 (2001).
 - [19] Y. Ando, Y. Okamoto, H. Miyamoto, T. Nakayama, T. Inoue, and M. Kuzuhara, *IEEE Electron Device Lett.* **24**, 289 (2003).

Chapter 5

Current linearity and operation stability in GaN MIS HEMTs

5.1 Background

The background of this chapter was already described in “Introduction”. However, the background of this chapter is described here more precisely.

Various kinds of insulator materials have been applied to improve the performance of GaN-based MIS HEMTs, several problems remain unsolved [1]. The most serious problem is the threshold voltage (V_{TH}) instability, as schematically shown in Figure 5.1(a). Several papers reported that different bias conditions induce varying degrees of V_{TH} shift in MIS HEMTs [2–7]. Lu et al. [2] and Johnson et al. [5] reported that higher positive gate biasing of the MIS HEMTs induces larger V_{TH} shift toward the forward bias direction. There are two possible mechanisms for this issue. Under a high positive gate bias, the Fowler-Nordheim (FN) tunneling mechanism can enhance the gate leakage current. In this case, electrons injected into trap levels in insulators cause excess negative charges, resulting in the V_{TH} shift toward the positive bias direction. The high positive gate bias also supplies electrons to electronic states at the insulator/barrier (AlGaN or InAlN) interface, and the acceptor-type states produce negative charges when they trap electrons. Due to the long associated time constant for electron emission even at RT, electrons captured at deeper interface states remain trapped during the entire duration of gate sweeping toward the negative bias direction [1, 8]. This also causes the V_{TH} shift toward the positive bias direction in the $I_D - V_G$ characteristics, as schematically shown in Figure 5.1(a).

Another problem is an unexpected degradation of current linearity in GaN-based MIS HEMTs. Although a dynamic range of input signal sweeping is one of advan-

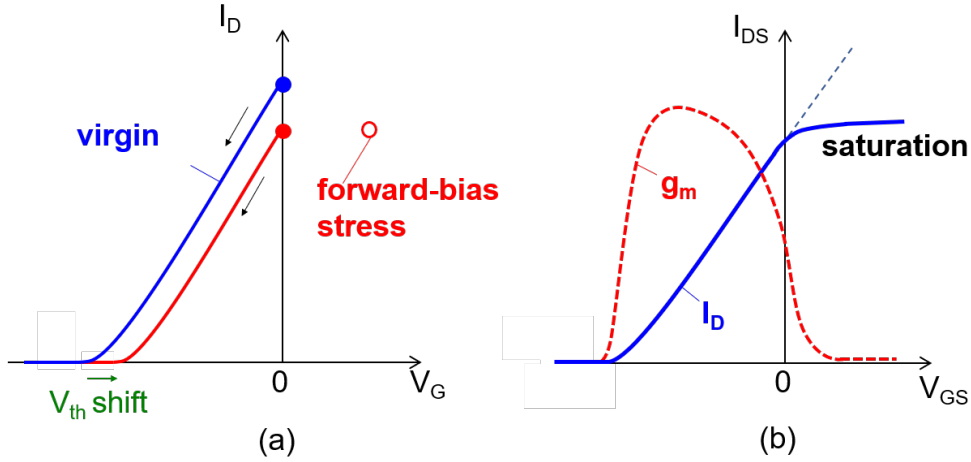


Figure 5.1. Schematic illustration of the $\text{Al}_2\text{O}_3/\text{Al}_{0.24}\text{Ga}_{0.76}\text{N}/\text{GaN}$ MOS HEMT structure.

tages in MIS HEMTs, some groups reported on the sudden current saturation at forward bias [9, 10], as shown in Figure 5.1(b). It is likely that a high density of electronic states at the insulator/barrier interface, in particular near the conduction band edge, screens the gate electric field and causes a limited control of surface potential of the barrier layer. This prevents further increase in the 2DEG density, leading to pronounced current saturation at forward gate bias. Such degradation of current linearity can be responsible for gain loss and degradation of large signal linearity in power amplifiers.

Accordingly, this paper presents DC characterization of AlGaIn/GaN MOS HEMTs using Al_2O_3 focusing on the impact of interface states on current linearity and operation stability. To control electronic states at the $\text{Al}_2\text{O}_3/\text{AlGaIn}$ interface, MOS HEMTs were subjected to a bias annealing under air atmosphere.

5.2 Device Fabrication Processes

Figure 5.2 schematically shows the MOS-HEMT device studied in this work. $\text{Al}_{0.24}\text{Ga}_{0.76}\text{N}/\text{GaN}$ heterostructure grown on SiC substrate by metal organic chemical vapor deposition (MOCVD) was used as the starting wafer. The 2DEG density and mobility of the AlGaIn/GaN heterostructure were $9.0 \times 10^{12} \text{ cm}^{-2}$ and $1740 \text{ cm}^2\text{V}^{-1}\text{s}^{-1}$, respectively. Ti/Al/Ti/Au (= 20/50/20/50 nm) source and drain electrodes were deposited on the AlGaIn surface, followed by ohmic annealing

at 830 °C for 1 min in N_2 ambient. As a surface protection layer during ohmic annealing, a 20-nm-thick SiN film was deposited to prevent damage to the AlGaIn surface [11]. After the ohmic metallization process, the SiN film was removed using a buffered HF solution. An Al_2O_3 layer with a nominal thickness of 30 nm was then deposited on the AlGaIn surface using an atomic layer deposition (ALD) system (SUGA-SAL1500) at 300 °C. In the deposition process, water vapor and trimethylaluminum were introduced into a reactor in alternate pulse forms. Each precursor was injected into the reactor for 15 ms, and the purging time was set to 5 s. In this case, the deposition rate is 0.11 nm/cycle, facilitating the formation of Al_2O_3 in a layer-by-layer fashion. Finally, the device fabrication was completed by electron beam evaporation of Ni/Au bilayer and subsequent lift-off process to form the gate electrode. The gate length, gate width, and gate-drain distance were 5, 100, and 10 μm , respectively.

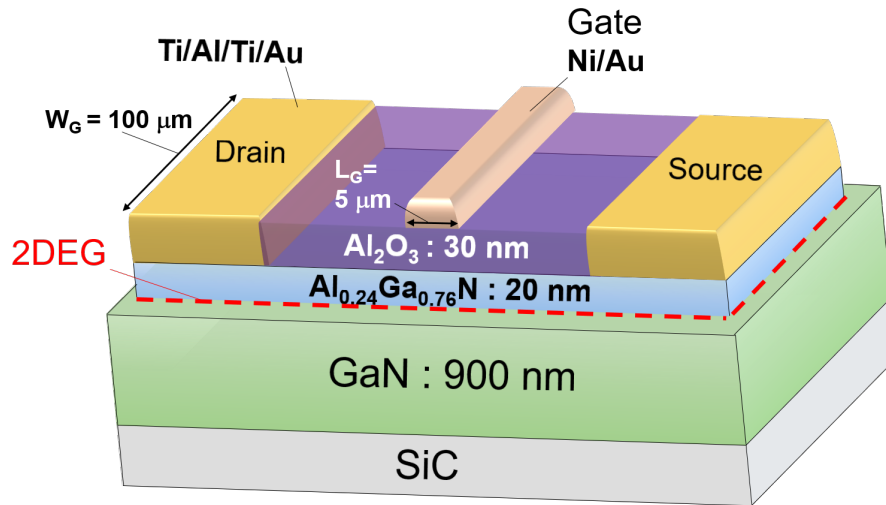


Figure 5.2. Schematic illustration of the $\text{Al}_2\text{O}_3/\text{Al}_{0.24}\text{Ga}_{0.76}\text{N}/\text{GaN}$ MOS HEMT structure.

5.3 Extremely Decreased Electronic States at $\text{Al}_2\text{O}_3/\text{n-GaN}$ Interface by Reverse-Bias Annealing

The process of our group to decrease the interface state density is proposed in this section. To improve the interface properties of GaN MIS structures, we have carried out various kinds of control processes including post-deposition and post-

metallization annealing processes. As described in Ref. [12], $\text{Al}_2\text{O}_3/\text{GaN}/\text{n}^+\text{-GaN}$ MOS diodes described in chapter 3.9 were applied a standard post-deposition annealing at 400-700 °C in N_2 for 30 min. It was effective in decreasing state densities at the $\text{Al}_2\text{O}_3/\text{GaN}$ interface. Even in this case, the interface state density of $5 \times 10^{11} \text{cm}^{-2} \text{eV}^{-1}$ or higher remained, indicating that the post-deposition annealing is insufficient for controlling interface states.

However, we then found that the “reverse-bias annealing” in air, at 300 °C, and under reverse voltage (-10 V) is more effective in achieving excellent C-V characteristics with negligible frequency dispersion, as shown in Figure 5.3(a). The C-V

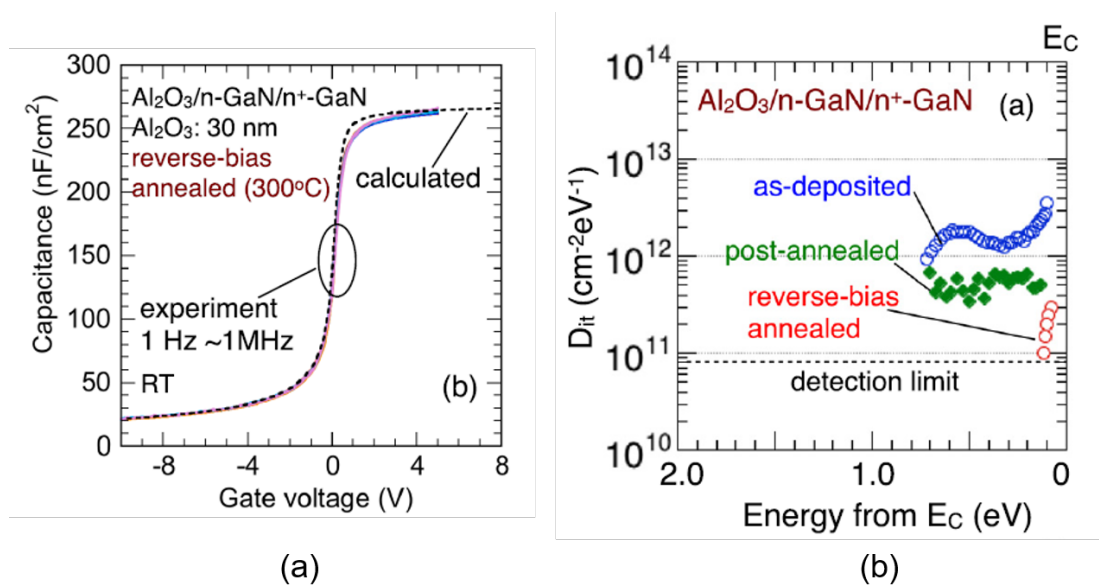


Figure 5.3. (a) Room-temperature (RT) C-V characteristics of MOS diodes fabricated on the GaN substrate with reverse-bias annealing and (b) interface state density (D_{it}) distributions determined by applying the Terman method to 1-MHz C-V results for $\text{Al}_2\text{O}_3/\text{GaN}/\text{n}^+\text{-GaN}$.

curves of the bias-annealed sample are very close to the calculated curve (broken line) with no such bump-like behavior in a very wide frequency range of 1 Hz - 1 MHz. There is a difference of flat-band voltage (V_{FB}) between samples without and with the reverse-bias annealing. Again, on the one hand, the annealed sample exhibited a V_{FB} very close to the calculated value; while, on the other hand, the as-deposited sample showed a V_{FB} shift toward the negative bias direction, probably due to excess positive charges arising from donor-type interface states and/or defect levels in the bulk Al_2O_3 . As mentioned below, the bias-annealing process decreased

such states and levels, resulting in the V_{FB} recovery to the expected value.

Figure 5.3(b) shows the interface state density distributions of Al₂O₃/GaN interfaces determined by applying the Terman method to 1 MHz CV results for the Al₂O₃/n-GaN/n⁺-GaN structure. Note that the time constant of electron emission is extremely long at RT for interface states with deep energies relative to the conduction band edge. We thus plotted the evaluated data within the range $E_C - 0.8$ eV in Figure 5.3(b). The as-deposited sample exhibited relatively high state densities in the range of 10^{12} cm⁻²eV⁻¹. In addition, a peak corresponding to a density of 2×10^{12} cm⁻²eV⁻¹ appeared at around $E_C - 0.6$ eV, probably arising from a discrete trap related to the nitrogen-vacancy defects [13–15]. After post-deposition annealing at 400 °C, the interface state density was decreased. Even in this case, however, the state densities of 5×10^{11} cm⁻²eV⁻¹ or higher remained. On the other hand, the reverse-bias annealing in air at 300 °C for 3 h resulted in a significant reduction in state density. In fact, the reverse-bias-annealed sample showed a state density below the detection limit ($< 1 \times 10^{11}$ cm⁻²eV⁻¹) except for those energies near the conduction band edge, corresponding to nearly ideal C-V curves without frequency dispersion as shown in Figure 5.3(a).

Figure 5.4 shows the C-V characteristics measured at 200 °C for the Al₂O₃/n-GaN/n⁺-GaN structure with the reverse-bias annealing. For high temperature C-V measurements, it is expected that deeper interface states can respond both to bias sweeping and ac signal modulation, causing changes in C-V characteristics compared with those measured at RT. In fact, Matocha et al., [16,17] Ooyama et al., [18] and Long et al. [19] reported significant stretch-out of C-V curves, bump-like C-V behavior, and enhanced frequency dispersion for SiO₂/GaN and Al₂O₃/GaN structures at measurement temperatures from 175 to 300 °C. Such unstable C-V behavior at high temperatures indicates that relatively high-density interface states can cause operation instability in GaN-based MOSFETs. In our reverse-bias annealed sample, however, the high-temperature C-V behavior remained almost unchanged, as compared with the RT C-V curves shown in Figure 5.4. In particular, negligible frequency dispersion and the same C-V slope were observed even at high temperature of 200 °C. These results indicate that the present process applied on a MOS

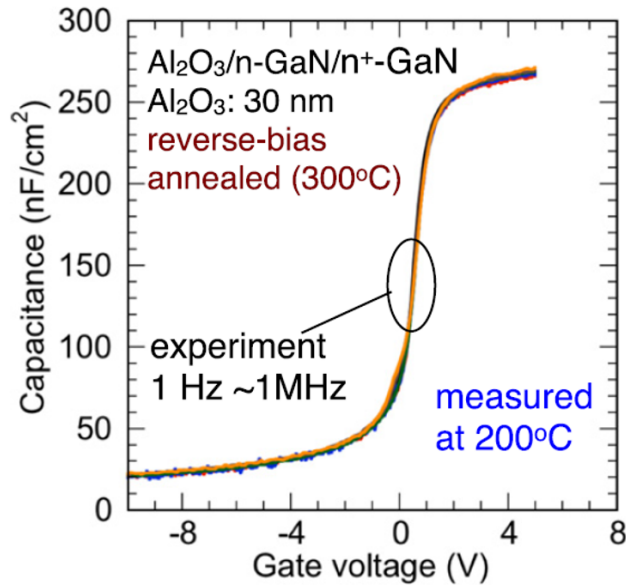


Figure 5.4. C-V characteristics measured at 200 °C of MOS diodes fabricated on the GaN substrate with reverse-bias annealing.

structure on a high quality and low dislocation density GaN layer realizes a stable MOS structure with low interface state densities. In this work, we expect that the desirable effects of the reverse-bias annealing can be extended to AlGaIn/GaN MOS HEMTs, thereby giving an alternative method in pushing the performance of these devices when applied in high power and high frequency applications.

5.4 Results and Discussion

5.4.1 $I - V$ characteristics and gate controllability of AlGaIn/GaN MOS-HEMTs

Typical $I_D - V_D$ characteristics of MOS-HEMTs without and with the bias annealing are shown in Figure 5.5. Both devices showed relatively good $I_D - V_D$ behavior at low V_G bias. For the MOS-HEMT without annealing, however, suppressed increase in I_D was observed at the gate bias higher than 0 V. On the other hand, the MOS-HEMT with the bias annealing showed good gate control of I_D even at forward gate bias, as shown in Figure 5.5(b).

The transfer characteristics of MOS-HEMTs without and with the bias annealing are shown in Figure 5.6(a). For comparison, their transfer curves as a function of gate overdrive voltage ($V_G - V_{TH}$) are replotted in Figure 5.6(b). The bias-

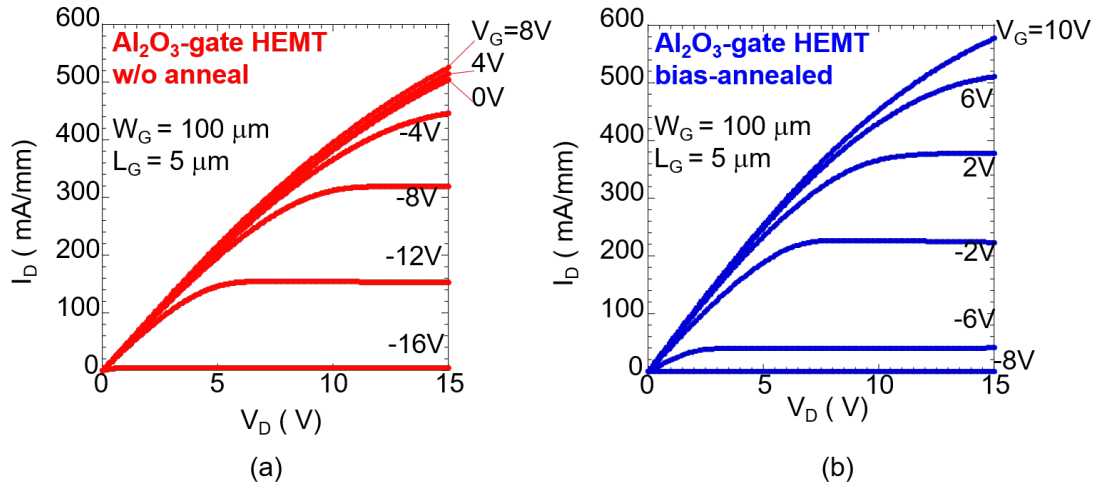


Figure 5.5. $I_D - V_D$ characteristics of $\text{Al}_2\text{O}_3/\text{AlGaIn}/\text{GaIn}$ MOS HEMTs (a) without and (b) with the bias annealing.

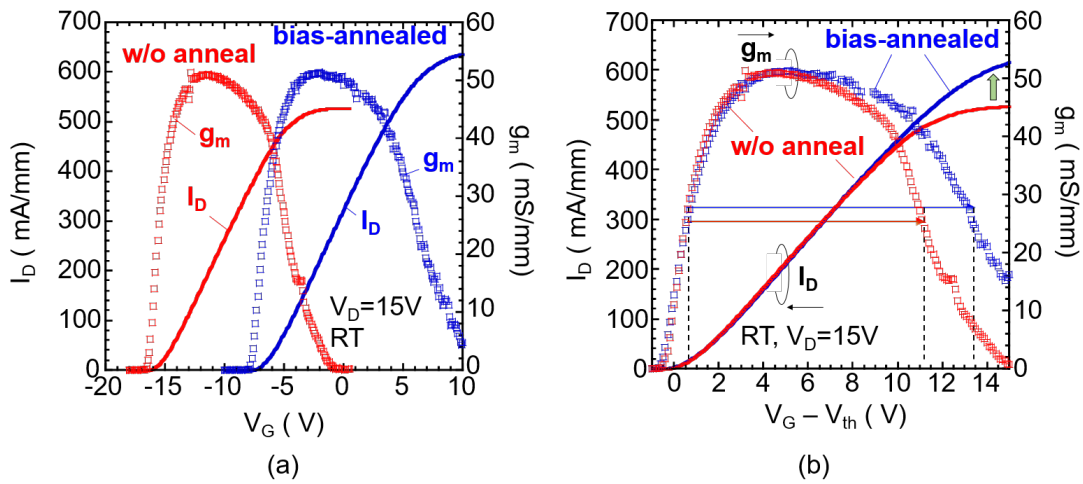


Figure 5.6. (a) Transfer characteristics of $\text{Al}_2\text{O}_3/\text{AlGaIn}/\text{GaIn}$ MOS HEMTs without and with the bias annealing process. (b) The data were replotted with respect to $V_G - V_{th}$.

annealing process effectively improved the current linearity, particularly in forward bias, resulting in a broader g_m plateau and increased maximum drain current. This effect is important for the MOS-HEMT in terms of the input dynamic range at forward bias. We then calculated the subthreshold slope of MOS-HEMTs from the semi-log scale $I_D - V_G$ characteristics shown in Figure 5.7. A high value of subthreshold slope of 148 mV/dec was obtained before the bias annealing. After bias annealing, the subthreshold slope was decreased down to 112 mV/dec. In addition,

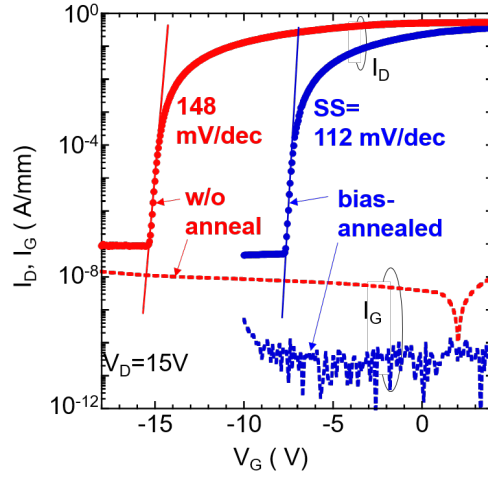


Figure 5.7. Logarithmic transfer curves and gate leakage current of MOS-HEMTs.

the V_{TH} change and significant decrease in gate leakage current were observed in the MOS-HEMT after the bias annealing, as shown in Figure 5.7. A possible mechanism for these will be discussed later.

To investigate interface properties of the $\text{Al}_2\text{O}_3/\text{AlGaN}$ gate structures, $C - V$ characterization was performed on MOS diodes fabricated on the same AlGaN/GaN heterostructures. A circular gate with a diameter of $200 \mu\text{m}$ was prepared for the MOS diodes. $C - V$ curves obtained using a signal frequency of 1 MHz at RT are shown in Figure 5.8(a). Both diodes without and with the bias annealing showed the two-step behavior typically observed in HEMT MOS structures [8,20]. The first step at reverse bias indicates the depletion of 2DEG at the AlGaN/GaN interface. The following capacitance plateau corresponds to the equivalent capacitance of Al_2O_3 and AlGaN layers connected in series. At forward bias, the nearly flat band condition of the AlGaN layer can lead to the electron spillover from the AlGaN/GaN to $\text{Al}_2\text{O}_3/\text{AlGaN}$ interfaces [20]. Consequently, the effective capacitance approaches that of the insulator capacitance.

To evaluate the effects of interface states on the $C - V$ characteristics, one-dimensional simulation including self-consistent Poisson-Schrödinger calculations was carried out for the $\text{Al}_2\text{O}_3/\text{AlGaN}/\text{GaN}$ structure, taking into account a state density distribution $[D_{it}(E)]$ consisting of acceptor- and donor-like states separated by the charge neutrality level E_{CNL} [21–23], as schematically shown in Figure 5.8(b).

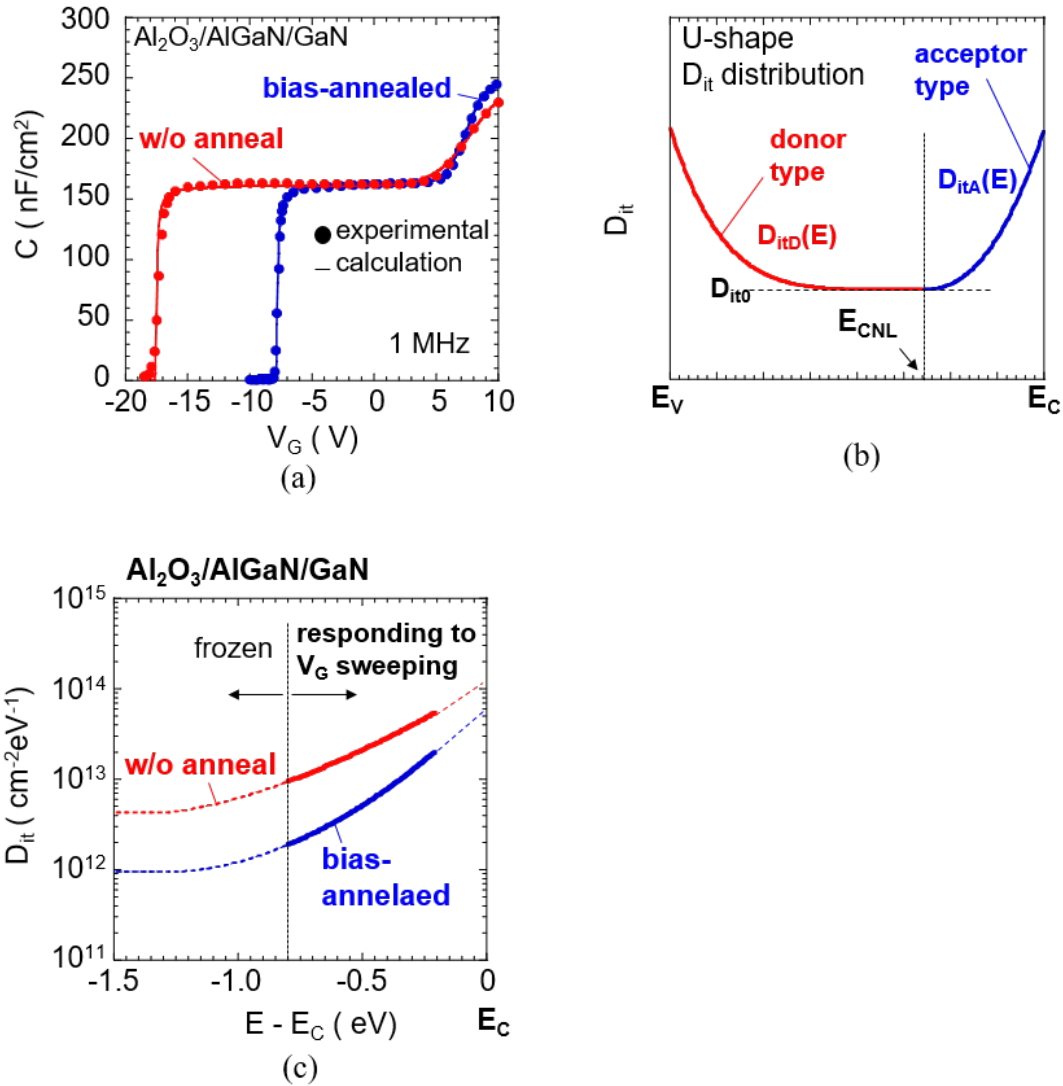


Figure 5.8. (a) C-V characteristics of the $\text{Al}_2\text{O}_3/\text{AlGaN}/\text{GaN}$ MOS diodes. The solid line indicates calculated curves. (b) Schematic illustration of interface state density (D_{it}) distribution used for calculation. (c) D_{it} distributions determined by the fitting of C-V curves.

Along the insulator-semiconductor interface, the crystalline periodicity of the semiconductor is terminated. In addition, disorder in atomic-bond arrangement can be induced at the semiconductor surface. In this case, the separation of conduction and valence bands becomes insufficient, resulting in the penetration of bonding and anti-bonding states into the forbidden band (bandgap) from valence and conduction bands, respectively [24,25]. Therefore, the charging character of interface states also reflects those of valence and conduction bands. Namely, a negative charge appears

in the conduction band if a state is occupied by an electron (acceptor-like character), while valence band state is positively charged when unoccupied (donor-like character). Thus, it can be assumed that the interface state continuum consists of a mixture of acceptor-like and donor-like states, as schematically shown in Figure 5.8(b), and their branch point act as the E_{CNL} . This model is often used as a density distribution of interface states [26–28].

For the calculation, we assumed an arbitrary D_{it} distribution using the following equations [21]:

$$D_{itA} = D_{it0} \exp \left[\left(\frac{E - E_{CNL}}{E_{0A}} \right)^{n_A} \right], \quad (5.1)$$

$$D_{itD} = D_{it0} \exp \left[\left(\frac{E_{CNL} - E}{E_{0D}} \right)^{n_D} \right], \quad (5.2)$$

where D_{it0} is the minimum state density. E_0 and n define the curvature of the D_{it} distribution, as shown in Figure 5.8(b). In addition, we can estimate electron emission time constant $\tau(E)$ from interface states to the conduction band using Shockley-Read-Hall (SRH) statistics:

$$\tau(E) = \frac{1}{v_{TH} \sigma_{TH} N_C} \exp \left(\frac{E_T}{kT} \right), \quad (5.3)$$

where v_{TH} , σ_{TH} , N_C , and E_T are electron thermal velocity, capture cross section of interface states, density of state at the conduction band, and interface state energy, respectively. From $\tau(E)$ and the experimental C-V measurement time (t_{meas}), we calculated the effective emission coefficient $D_{eT}(E)$ of interface states:

$$D_{eT}(E) = 1 - \exp \left[-\frac{t_{meas}}{\tau(E)} \right]. \quad (5.4)$$

Figure 5.9 shows the calculated $D_{eT}(E)$ at RT using $t_{meas} = 100s$ and $\sigma = 1 \times 10^{-16} cm^2$ [21]. According to Eq. (5.3), $\tau(E)$ of interface states near midgap or deeper are too large at RT, resulting in $D_{eT}(E) = 0$. This means that electrons once captured at such deep interface states remain trapped even when large negative bias is applied to the gate electrode. It is estimated from Figure 5.9 that interface states at energies below $E_C - 0.8$ eV behave like “frozen states”. By considering $D_{eT}(E)$

and Fermi-Dirac occupation function, we obtained interface state charges (ionized state density) at a given gate voltage V_G . Then we calculated $C - V$ curve based on the potential and electron density distributions by numerically solving Poisson-Schrödinger equations, and compared experimental and calculated $C - V$ curves. If we observed the discrepancy between them, then the D_{it} distribution was modified and the recalculation was repeatedly carried out. Physical parameters used in the calculation are summarized in Table 5.1.

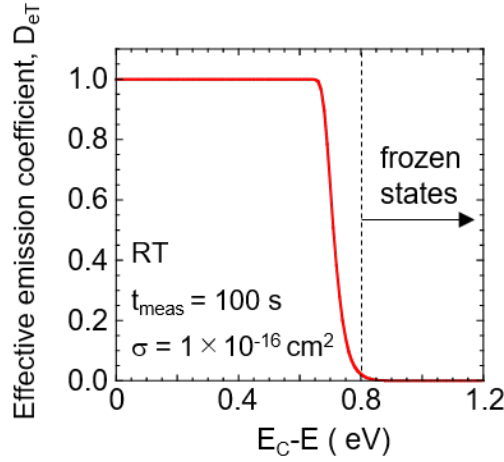


Figure 5.9. Calculated $D_{eT}(E)$ using $t_{\text{meas}} = 100$ s, $s = 1 \times 10^{-16}$ cm $^{-2}$ and $t(E)$ obtained from Eq. (4).

Table 5.1. Parameters used in the calculations. m_0 is the mass of a free electron, q is the elementary charge, and AlGa N denotes Al $_{0.24}$ Ga $_{0.76}$ N.

Parameter name	Symbol (unit)	Numerical value (material or interface)
Bandgap at RT	E_G (eV)	3.4 (Ga N) [29]
		3.89 (AlGa N) [29, 30]
Effective mass of electron	m_e/m_0	7.0 (Al $_2$ O $_3$) [32]
		0.20 (Ga N)
Relative permittivity	ϵ	0.23 (AlGa N)
		9.5 (Ga N)
Band offset	ΔE_C (eV)	9.2 (Al $_{0.24}$ Ga $_{0.76}$ N)
		9.0 (Al $_2$ O $_3$)
Surface barrier height	ϕ_s (eV)	0.34 (AlGa N /Ga N) [29]
		2.1 (Al $_2$ O $_3$ /AlGa N) [32]
Polarization induced sheet charge	n_s (q/cm 2)	3.4 (Ni/Al $_2$ O $_3$) [31]
Charge neutrality level	E_{CNL}	8×10^{12} (AlGa N /Ga N)
Capture cross section of interface states	σ (cm 2)	$E_C - 1.3$ eV (Al $_2$ O $_3$ /AlGa N) [23]
		1×10^{-16} [21]
C-V Measurement duration	t (s)	100

Using the D_{it} distributions shown in Figure 5.8(c), the calculation well reproduced the experimental $C - V$ data, as indicated by solid lines in Figure 5.8(a). As described above, only the acceptor-like traps in the energy range indicated by solid lines in Figure 5.8(c) can change their charge state accordingly with the gate voltage sweep at RT. Note, in addition, that it is difficult to evaluate the state density distribution at energies above $E_C - 0.2$ eV from $C - V$ measurements using frequency of 1 MHz, because electron trapping/detrapping processes at such shallow interface states can respond to the measurement AC signal and accordingly give an inaccurate estimate of capacitance. Therefore, state densities at the energies above $E_C - 0.2$ eV were not considered for the present $C - V$ calculation.

As shown in Figure 5.8(c), the $\text{Al}_2\text{O}_3/\text{AlGaIn}$ interface without annealing showed high interface state densities of over $1 \times 10^{13} \text{ cm}^{-2}\text{eV}^{-1}$. The bias annealing process effectively decreased the state densities, leading to the steeper $C - V$ slope in forward bias shown in Figure 5.8(a). The calculated V_{TH} corresponding to the first step in the $C - V$ curve was -7.5 V, very close to that of the MOS-HEMT subjected to bias annealing, as shown in Figure 5.8(a). On the other hand, the sample without the annealing showed a V_{TH} shift toward the negative bias direction, probably due to excess positive charges arising from donor-type interface states and/or defect levels in the bulk Al_2O_3 . When a fixed charge of $+1.2 \times 10^{13} \text{ cm}^{-2}$ was assumed in the Al_2O_3 layer or at the $\text{Al}_2\text{O}_3/\text{AlGaIn}$ interface, the calculation reproduced the experimental $C - V$ result for the HEMT without annealing, as shown in Figure 5.8(a). A possible candidate for a defect level in Al_2O_3 is an oxygen-vacancy related defect [33, 34]. The bias-annealing process decreased such levels, resulting in the V_{TH} recovery toward the expected value. Zhou et al. [35] also reported similar V_{TH} recovery with a post-deposition annealing in $\text{Al}_2\text{O}_3/\text{AlGaIn}/\text{GaN}$ MOS-HEMTs. As shown in Figure 5.7, in addition, we observed decrease in gate leakage current in the MOS-HEMT after the bias annealing. For the GaN-based MIS-HEMTs using Al_2O_3 , SiN_x and AlTiO , it has been reported that the Poole-Frenkel (PF) emission conduction was dominant for gate leakage current [36–39]. Similarly to the V_{TH} recovery behavior, there is a possibility the reduction of leakage current arises from decrease in defect levels in the Al_2O_3 layer, contributing to the suppression of the

PF hopping conduction.

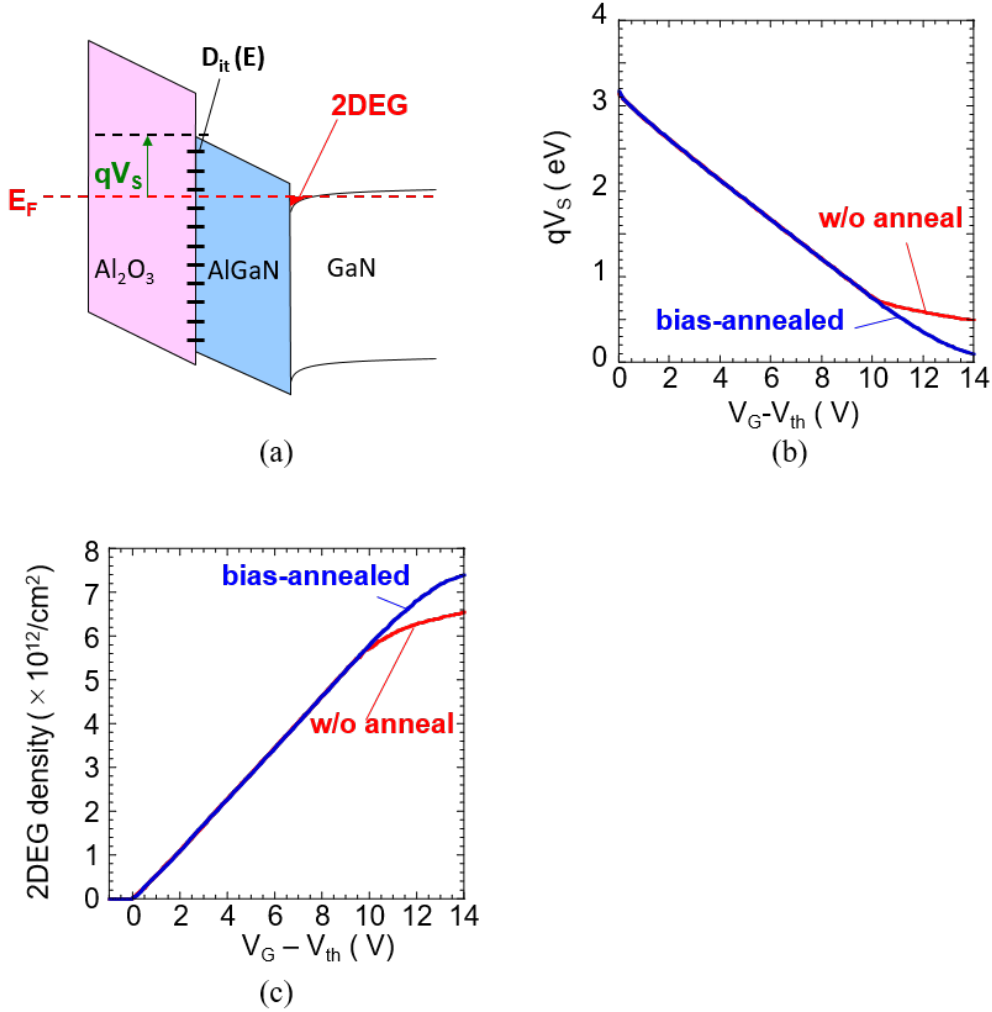


Figure 5.10. (a) Band diagram of the Al₂O₃/AlGaN/GaN structure. V_S indicates the AlGaN surface potential. (b) Calculated V_S as a function of V_G - V_{TH} with assuming D_{it} distributions shown in Figure 5.8. (c) Calculated 2DEG densities as a function of V_G - V_{TH} for the MOS-HEMTs without and with the bias annealing.

The $C - V$ analysis showed that the bias annealing process effectively decreased state densities at the Al₂O₃/AlGaN interface, leading to the improvement of current linearity, as shown in Figure 5.6. To gain a better insight into the relationship between interface states and gate controllability of the MOS-HEMT, we calculated surface potential (V_S) of AlGaN shown in Figure 5.10(a) and the 2DEG density as a function of gate overdrive, taking into account D_{it} distributions obtained from the $C - V$ analysis [Figure 5.8(c)]. For the 2DEG density calculation, we used the following equation [40, 41]:

$$2DEGdensity_i = \frac{m_e k_B T}{\pi \hbar^2} \ln [1 + \exp ((E_i - E_f)/(k_B T))], \quad (5.5)$$

where m_e is the effective electron mass, k_B is Boltzman's constant, T is the temperature, and i indicates the i_{th} discrete excited level at the AlGa_N/Ga_N interface.

Figure 5.10(b) shows the calculated V_S as a function of gate overdrive for the MOS-HEMTs without and with the bias annealing. In the gate bias range up to 10 V, both devices showed the same V_S change. This gate voltage corresponds to $qV_S = 0.8$ eV. As mentioned above, interface states at energies below $E_C - 0.8$ eV are considered to be "frozen states", i.e., negligible effect on the V_S control. Beyond $V_G - V_{TH} = 10V$, acceptor states shown in Figure 5.8(c) are active accordingly with the gate voltage sweeping, and the ionized acceptor charges screen the gate electric field. Thus high-density states prevent V_S modulation (poor potential control) for the MOS-HEMT without the bias annealing. Such V_S behavior is directly related to the control of the 2DEG density, as shown in Figure 5.10(c). The limited increase in the 2DEG density with V_G is clearly observed for the MOS-HEMT without the bias annealing. On the other hand, the MOS-HEMT with annealing shows relatively good control of 2DEG by V_G . The calculated results shown in Figure 5.10(c) are similar to the measured $I_D - V_G$ curves of MOS-HEMTs shown in Figure 5.6(b), indicating that the effective reduction of interface states is responsible for the improved linearity in MOS-HEMT with bias annealing.

It should be mentioned that some papers reported poor current linearity in MIS-type AlGa_N/Ga_N HEMTs. To investigate current linearity behavior, we tried to plot the full width at half maxima (FWHM) of $g_m - V_G$ profiles as a function of the equivalent oxide thickness (EOT) including insulator and AlGa_N barrier layers. Figure 5.11 shows comparison of FWHM of g_m for AlGa_N/Ga_N MIS-HMETs using SiO₂ [42–44], Al₂O₃ [35, 45–48], SiN [9, 10, 49, 50], HfO₂ [51, 52], AlN [53], Ga₂O₃ [54] and TiO₂ [55] dielectric materials. Our data are also included in Figure 5.11. It is expected that the FWHM of g_m increases with EOT, and experimental data generally showed this tendency. However, there is a wide scattering of data, indicating that interface properties of insulator/AlGa_N structures are not dependent on the insulator material used but on the bond disorder and/or surface defects

on the AlGa_N surface, probably related to fabrication process conditions including deposition methods [1, 56–58]. The broken line is a guide to the eye for the better results reported [44, 46, 50]. Our device with the bias annealing showed high FWHM value, demonstrating excellent current linearity in our AlGa_N/Ga_N MOS-HEMT.

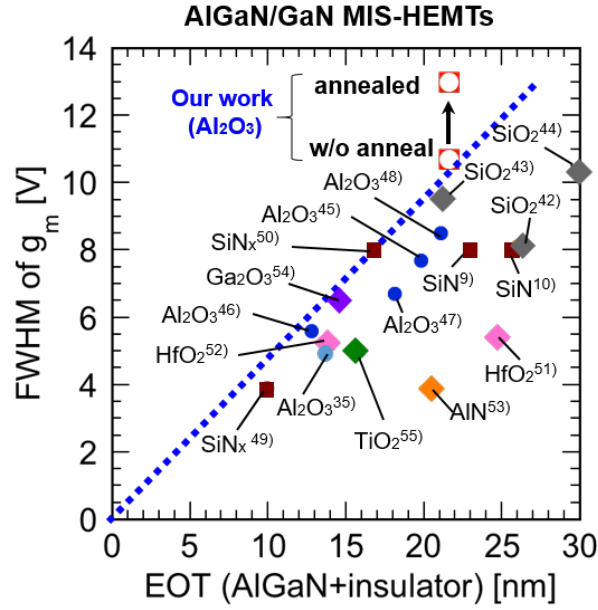


Figure 5.11. Plots of FWHM in the gm spectrum as a function of the equivalent oxide thickness (EOT) including insulator and AlGa_N barrier layers for AlGa_N/Ga_N MIS-HEMTs. The numbers indicate literatures cited.

5.4.2 Operation Stability of AlGa_N/Ga_N MOS-HEMTs

To evaluate operation stability of the MOS-HEMT, the V_{TH} shift after applying forward bias stress was also investigated. For fair comparison, the equivalent stress bias with respect to $V_G - V_{TH}$ was applied to the MOS-HEMTs without and with the bias annealing ($V_G - V_{TH} = 23V$), as shown in Figure 5.12. The gate stress time was 10 s, while keeping $V_D = 15V$. Then the $I_D - V_G$ characteristics were measured from $V_G = 0V$ toward the negative bias direction, as shown in Figure 5.12. The broken lines indicate the transfer curves without the stress bias. We observed V_{TH} shift toward the forward bias direction after applying the stress bias for both devices, similar to those reported for AlGa_N/Ga_N MIS-HEMTs [2, 3]. It is likely due to electron injection into traps in Al₂O₃ and/or states at the Al₂O₃/AlGa_N interface, producing negative charges. It was found from the $C - V$ analysis as described above

that the bias annealing process effectively reduced both interface states and bulk traps in Al_2O_3 , thereby mitigating the V_{TH} shift even after applying the forward bias stress in bias-annealed device, as shown in Figure 5.12.

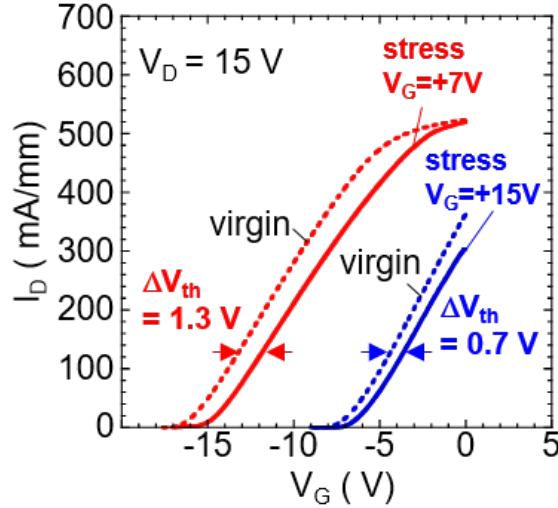


Figure 5.12. Transfer characteristics before and after the forward bias stress for the MOS-HEMTs without and with the bias annealing.

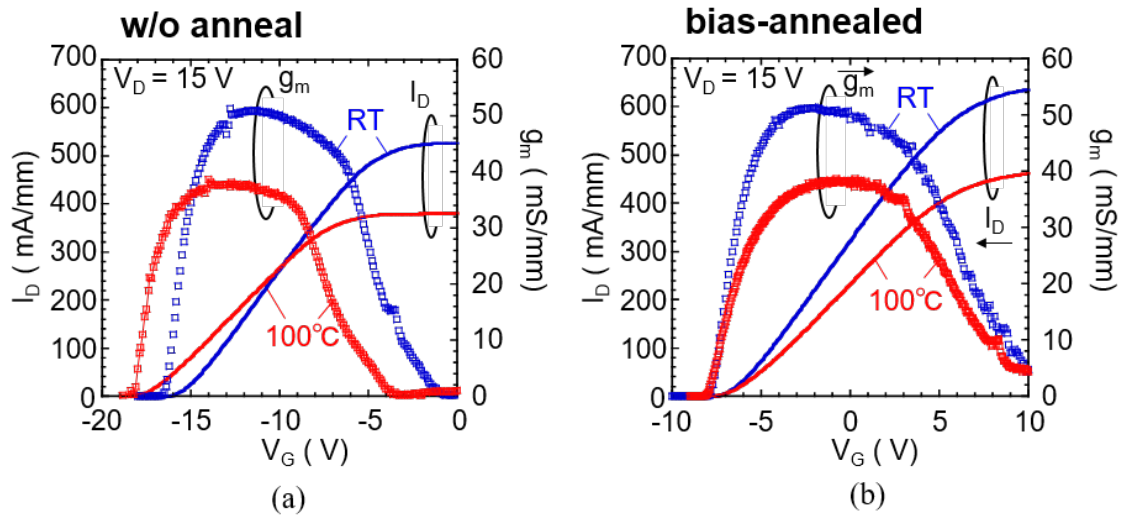


Figure 5.13. Transfer characteristics measured at RT and 100 °C for the MOS-HEMTs (a) without and (b) with the bias annealing.

We then measured the transfer characteristics of the devices at a higher temperature of 100 °C. As shown in Figure 5.13, both devices showed about 30% reduction in g_m and decreased maximum drain current, as compared with those measured at

RT. This is consistent with the results reported by Husna et al. [59] and Suria et al. [60], and mainly due to the reduction of electron mobility attributed to optical phonon scattering at high temperatures [61, 62]. As shown in Figure 5.13(a), the MOS-HEMT without the annealing showed a deeper V_{TH} at 100 °C. Husna et al. [59] and Yang et al. [63] reported similar V_{TH} shift at high temperature, and pointed out a possibility that some of donor-like defect levels such as oxygen vacancies in Al_2O_3 can detrapp larger number of electrons at elevated temperatures, resulting in excess positive charges driving the V_{TH} toward the negative bias direction. According to the SRH statistics, in addition, deeper interface states can emit electrons to the conduction band at higher temperatures, relatively increasing the number of positive charges at the $\text{Al}_2\text{O}_3/\text{AlGaIn}$ interface. High densities of states for the MOS-HEMT without the annealing, as shown in Figure 5.8(c), enhance this charging effect. On the other hand, the V_{TH} of the MOS-HEMT with the bias annealing remained unchanged even at 100 °C, as shown in Figure 5.13(b), probably due to the reduction of defect levels in Al_2O_3 and interface states.

5.5 Conclusions

To improve current linearity and operation stability, bias annealing in air at 300 °C was applied to $\text{AlGaIn}/\text{GaIn}$ MOS-HEMTs using Al_2O_3 as gate oxide. The device without annealing showed a sudden current saturation at forward bias. On the other hand, the MOS HEMT with the annealing showed improved current linearity, resulting in the increase in the maximum drain current. Lower subthreshold slope was also observed after the bias annealing. From the precise C-V analysis on the MOS diode fabricated on the $\text{AlGaIn}/\text{GaIn}$ heterostructure, it was found that the bias annealing effectively reduced the state density at the $\text{Al}_2\text{O}_3/\text{AlGaIn}$ interface. This led to efficient modulation of the AlGaIn surface potential closely to the conduction band edge, resulting in good gate control of 2DEG density even at forward bias. In addition, the MOS HEMT with the annealing showed smaller threshold voltage shift after applying forward bias stress. For the device without annealing, the V_{TH} measured at 100 °C was much deeper than that at RT. On the other hand, such temperature-dependent change in the V_{TH} was not observed for the MOS-HEMT with the annealing. We therefore demonstrated that bias annealing in air is effec-

tive in improving current linearity and operation stability of Al₂O₃/AlGa_xN/GaN MOS-HEMTs.

References

- [1] Z. Yatabe, J. T. Asubar, and T. Hashizume, *J. Phys. D* **49**, 393001 (2016).
- [2] Y. Lu, S. Yang, Q. Jiang, Z. Tang, B. Li, and K. J. Chen, *Phys. Status Solidi C* **10**, 1397 (2013).
- [3] P. Lagger, M. Reiner, D. Pogany, and C. Ostermaier, *IEEE Trans. Electron Devices* **61**, 1022 (2014).
- [4] M. Ľapajna, M. Jurkovič, L. Válik, Š. Haščik, D. Gregušová, F. Brunner, E.-M. Cho, and J. Kuzmik, *Appl. Phys. Lett.* **102**, 243509 (2013).
- [5] D. W. Johnson, R. T. P. Lee, R. J. W. Hill, M. H. Wong, G. Bersuker, E. L. Piner, P. D. Kirsch, and H. R. Harris, *IEEE Trans. Electron Devices* **60**, 3197 (2013).
- [6] P. Lagger, P. Steinschifter, M. Reiner, M. Stadtmuller, G. Denifl, A. Naumann, J. Muller, L. Wilde, J. Sundqvist, D. Pogany, and C. Ostermaier, *Appl. Phys. Lett.* **105**, 033512 (2014).
- [7] T.-L. Wu, D. Marcon, B. Bakeroot, B. D. Jaeger, H. C. Lin, J. Franco, S. Stoffels, M. V. Hove, R. Roelofs, G. Groeseneken, and S. Decoutere, *Appl. Phys. Lett.* **107**, 093507 (2015).
- [8] Z. Yatabe, Y. Hori, W.-C. Ma, J. T. Asubar, M. Akazawa, T. Sato, and T. Hashizume: *Jpn. J. Appl. Phys.* **53**, 100213 (2014).
- [9] Z. Zhang, W. Li, K. Fu, G. Yu, X. Zhang, Y. Zhao, S. Sun, L. Song, X. Deng, Z. Xing, L. Yang, R. Ji, C. Zeng, Y. Fan, Z. Dong, Y. Cai, and B. Zhang, *IEEE Electron Device Lett.* **38**, 236 (2017).
- [10] X. Lu, K. Yu, H. Jiang, A. Zhang, and K. M. Lau, *IEEE Trans. Electron Devices* **64**, 824 (2017).
- [11] Y. Hori, C. Mizue, and T. Hashizume, *Jpn. J. Appl. Phys.* **49**, 080201 (2010).
- [12] S. Kaneki, J. Ohira, S. Toiya, Z. Yatabe, J. T. Asubar, and T. Hashizume, *Appl. Phys. Lett.* **109**, 162104 (2016).

-
- [13] S. Kim, Y. Hori, W.-C. Ma, D. Kikuta, T. Narita, H. Iguchi, T. Uesugi, T. Kachi, and T. Hashizume, *Jpn. J. Appl. Phys.* **51**, 060201 (2012).
- [14] T. Hashizume and R. Nakasaki, *Appl. Phys. Lett.* **80**, 4564 (2002).
- [15] T. Hashizume and H. Hasegawa, *Appl. Surf. Sci.* **234**, 387 (2004).
- [16] K. Matocha, T. P. Chow, and R. J. Gutmann, *IEEE Electron Device Lett.* **23**, 79 (2002).
- [17] K. Matocha, R. J. Gutmann, and T. P. Chow, *IEEE Trans. Electron Devices* **50**, 1200 (2003).
- [18] K. Ooyama, H. Kato, M. Miczek, and T. Hashizume, *Jpn. J. Appl. Phys.* **47**, 5426 (2008).
- [19] R. D. Long, A. Hazeghi, M. Gunji, Y. Nishi, and P. C. McIntyre, *Appl. Phys. Lett.* **101**, 241606 (2012).
- [20] C. Mizue, Y. Hori, M. Miczek, and T. Hashizume, *Jpn. J. Appl. Phys.* **50**, 021001 (2011).
- [21] M. Miczek, C. Mizue, T. Hashizume, and B. Adamowicz, *J. Appl. Phys.* **103**, 104510 (2008).
- [22] J. Robertson and B. Falabretti, *J. Appl. Phys.* **100**, 014111 (2006).
- [23] W. Mönch, *J. Appl. Phys.* **109**, 113724 (2011).
- [24] H. Lüth, *Surface and Interfaces of Solids* (Springer, Berlin, 1993) 2nd ed., p. 262 and 382.
- [25] J. Tersoff, *Phys. Rev. Lett.* **52**, 465 (1984).
- [26] P. D. Ye, *J. Vac. Sci. Technol. A* **26**, 697 (2008).
- [27] J. Osvald, R. Stoklas, and P. Kordoš, *Phys. Status Solidi B* **252**, 996 (2015).
- [28] B. S. Eller, J. Yang, and R. J. Nemanich, *J. Vac. Sci. Technol. A* **31**, 050807 (2013).
- [29] O. Ambacher, J. Smart, J. R. Shealy, N. G. Weimann, K. Chu, M. Murphy, W. J. Schaff, and L. F. Eastmann, W. Riger, and J. Hilsenbeck, *J. Appl. Phys.* **85**, 3222 (1999).
- [30] M. Holtz, T. Prokofyeva, M. Seon, K. Copeland, J. Vanbuskirk, S. Williams, S. A. Nikishin, V. Tretyakov, and H. Temkin, *J. Appl. Phys.* **89**, 7977 (2001).
- [31] E. Bersch, S. Rangan, and R. A. Bartynski, *Phys. Rev. B* **78**, 085114 (2008).

-
- [32] T. Hashizume, S. Ootomo, T. Inagaki, and H. Hasegawa, *J. Vac. Sci. Technol. B* **21**, 1828 (2003).
- [33] P. Jonnard, C. Bonnelle, G. Blaise, G. Rémond, and C. Roques-Carmes, *J. Appl. Phys.* **88**, 6413 (2000).
- [34] M. Choi, J. L. Lyons, A. Janotti, and C. G. Van de Walle, *Phys. Status Solidi B* **250**, 787 (2013).
- [35] H. Zhou, G. I. Ng, Z. H. Liu, and S. Arulkumaran, *Appl. Phys. Express* **4**, 104102 (2011).
- [36] H. Liu, W. Hsu, C. Lee, B. Chou, Y. Liao, and M. Chiang, *IEEE Trans. Electron Devices* **61**, 2760 (2014).
- [37] S. Le, T. Ui, T. Q. Nguyen, H. Shih, and T. Suzuki, *J. Appl. Phys.* **119**, 204503 (2016).
- [38] M. Hua, C. Liu, S. Yang, S. Liu, K. Fu, Z. Dong, Y. Cai, B. Zhang, and K. J. Chen, *IEEE Trans. Electron Devices* **62**, 3215 (2015).
- [39] S. A. Jauss, K. Hallaceli, S. Mansfeld, S. Schwaiger, W. Daves, and O. Ambacer, *IEEE Trans. Electron Devices* **64**, 2298 (2017).
- [40] L. Gordon, M. Miao, S. Chowdhury, M. Higashiwaki, U. K. Mishra, and CG Van de Walle, *J Phys. D* **43**, 505501 (2010).
- [41] M. Zervos, A. Kostopoulos, G. Constantinidis, M. Kayambaki, and A. Georgakilas, *J. Appl. Phys.* **91**, 4387 (2002).
- [42] M. A. Khan, X. Hu, G. Sumin, A. Lunev, J. Yang, R. Gaska, and M. S. Shur, *IEEE Electron Device Lett.* **21**, 63 (2000).
- [43] D. Mistele, T. Rotter, K.S. Röver, S. Paprotta, M. Seyboth, V. Schwegler, F. Fedler, H. Klausning, O.K. Semchinova, J. Stemmer, J. Aderhold, and J. Graul, *Mater. Sci. Eng. B* **93**, 107 (2002).
- [44] L. Pang, Y. Lian, D. Kim, J.-H. Lee, and K. Kim, *IEEE Trans. Electron Devices* **59**, 2650 (2012).
- [45] P. D. Ye, B. Yang, K. K. Ng, J. Bude, G. D. Wilk, S. Halder, and J. C. M. Hwang, *Appl. Phys. Lett.* **86**, 063501 (2005).
- [46] D. J. Meyer, R. Bass, D. S. Katzer, D. A. Deen, S. C. Binari, K. M. Daniels, and C. R. Eddy, Jr., *Solid-State Electron.* **54**, 1098 (2010).

- [47] E. Miyazaki, Y. Goda, S. Kishimoto, and T. Mizutani, *Solid-State Electron.* **62**, 152 (2011).
- [48] F. Sang, M. Wang, C. Zhang, M. Tao, B. Xie, C. P. Wen, J. Wang, Y. Hao, W. Wu, and B. Shen, *Jpn. J. Appl. Phys.* **54**, 044101 (2015).
- [49] K. Zhang, M. Wu, X. Lei, W. Chen, X. Zheng, X. Ma, and Y. Hao, *Semicond. Sci. Technol.* **29**, 075019 (2014).
- [50] H. Jiang, C. Liu, Y. Chen, X. Lu, C. W. Tang, and K. M. Lau: *IEEE Trans. Electron Devices* **64**, 832 (2017).
- [51] S. Sugiura, Y. Hayashi, S. Kishimoto, T. Mizutani, M. Kuroda, T. Ueda, T. Tanaka, *Solid-State Electron.* **54**, 79 (2010).
- [52] O. Seok, W. Ahn, M.-K. Han, and M.-W. Ha, *Semicond. Sci. Technol.* **28**, 025001 (2013).
- [53] J.-J. Zhu, X.-H. Ma, Y. Xie, B. Hou, W.-W. Chen, J.-C. Zhang, and Y. Hao, *IEEE Trans. Electron Devices* **62**, 512 (2015).
- [54] H.-Y. Shih, F.-C. Chu, A. Das, C.-Y. Lee, M.-J. Chen, and R.-M. Lin, *Nanoscale Res. Lett.* **11**, 235 (2016).
- [55] Y.-S. Lin and C.-C. Lu, *J. Vac. Sci. Technol. B* **35**, 011209 (2017).
- [56] T. Hashizume and R. Nakasaki, *Appl. Phys. Lett.* **80**, 4564 (2002).
- [57] T. Hashizume and H. Hasegawa, *Appl. Surf. Sci.* **234**, 387 (2004).
- [58] S. Kim, Y. Hori, W.-C. Ma, D. Kikuta, T. Narita, H. Iguchi, T. Uesugi, T. Kachi, and T. Hashizume, *Jpn. J. Appl. Phys.* **51**, 060201 (2012).
- [59] F. Husna, M. Lachab, M. Sultana, V. Adivarahan, Q. Fareed, and A. Khan, *IEEE Trans. Electron Devices* **59**, 2424 (2012).
- [60] A. J Suria, A. S. Yalamarthy, H. So, and D. G Senesky, *Semicond. Sci. Technol.* **31**, 115017 (2016).
- [61] W.S. Tan, M.J. Uren, P.W. Fry, P.A. Houston, R.S. Balmer, and T. Martin, *Solid-State Electron.* **50**, 511 (2006).
- [62] Y.-H. Wang, Y. C Liang, G. S Samudra, T.-F. Chang, C. Huang, L. Yuan, and G.-Q. Lo, *Semicond. Sci. Technol.* **28**, 125010 (2013).
- [63] S. Yang, S. Liu, C. Liu, M. Hua, and K. J Chen, *Semicond. Sci. Technol.* **31**, 024001 (2016).

Chapter 6

Conclusion

This thesis aimed at the evaluation the effect of interface states on the electronic characterization of AlGaN/GaN HEMTs and to control the interface state density at Al₂O₃/AlGaN or Al₂O₃/GaN interfaces.

Chapter 1 started with the introduction of wireless mobile communication systems which are widely used all over the world. GaN and related materials are attractive for the application to the semiconductor devices owing to their superior physical properties. In addition, GaN-related High Electron Mobility Transistors (HEMTs) are very attractive for such devices. However, it is rather difficult to characterize and control electronic states, in particular, at the insulator/semiconductor interfaces in the insulated-gate GaN transistors because of their wide bandgap and complicated structure having two (or more) interfaces.

Chapter 2 explained the physical properties of III-N semiconductors and their heterostructures, followed by the generation of two-dimensional electron gas (2DEG). 2DEG is generated by spontaneous and piezoelectric polarization charges. Such polarization charges were calculated from some constants of GaN and AlN. Finally, 2DEG density vs AlGaN thickness was calculated.

Chapter 3 discussed basic theories on the electronic states at the Semiconductor surface and Insulator/Semiconductor interface. The models of “Metal-Induced-Gap-State (MIGS)” and “Disorder-Induced-Gap-State (DIGS)” were described. In addition, the equations from DIGS model to calculate interface state density distributions were described. To evaluate the effect of interface states on potential distribution and C-V characteristics of Al₂O₃/GaN MOS diodes. Finally, “reverse-bias annealing” to control the interface state density was proposed.

Chapter 4 introduced the experimental results obtained for this thesis. The dual-

gate AlGa_N/Ga_N HEMTs were fabricated to evaluate the surface charging area. In G2-stress/G1-drive scheme, the V_{TH} was shifted toward forward bias direction. To shed a light this phenomenon, the two-dimensional simulation was carried out. The 2D potential simulation indicated that surface negative charges induced by the G1 stress modulate the potential distribution in the AlGa_N barrier layer near the G2 edge where the potential near the surface of the AlGa_N barrier layer are apparently bended and lifted. Consequently, this may lead to a decreased 2DEG concentration in this region and eventually shifting of the V_{TH} towards positive voltage direction. It was also found that such surface charging can extend as far as 0.5 μm from the stressing gate edge.

Chapter 5 investigated the relationship between the interface state densities and the electrical properties of the Al₂O₃/AlGa_N/Ga_N MOS HEMTs. The “reverse-bias annealing” was also applied to the MOS HEMTs for reducing the Al₂O₃/AlGa_N interface. The device without annealing showed a sudden current saturation at forward bias. On the other hand, the MOS HEMT with the annealing showed improved current linearity, resulting in the increase in the maximum drain current. Lower subthreshold slope was also observed after the bias annealing. From the precise C-V analysis on the MOS diode fabricated on the AlGa_N/Ga_N heterostructure, it was found that the bias annealing effectively reduced the state density at the Al₂O₃/AlGa_N interface. This led to efficient modulation of the AlGa_N surface potential closely to the conduction band edge, resulting in good gate control of 2DEG density even at forward bias. In addition, the MOS HEMT with the annealing showed smaller threshold voltage shift after applying forward bias stress. For the device without annealing, the V_{TH} measured at 100 °C was much deeper than that at RT. On the other hand, such temperature-dependent change in the V_{TH} was not observed for the MOS-HEMT with the annealing. We therefore demonstrated that bias annealing in air is effective in improving current linearity and operation stability of Al₂O₃/AlGa_N/Ga_N MOS-HEMTs.

List of publications/conferences/awards

Publications

Journals

1. KenyaNishiguchi, Joel T. Asubar and T. Hashizume, “Evaluation of off-bias-stress induced surface charging at AlGa_N/Ga_N surface using a dual-gate transistor structure”, Japanese Journal of Applied Physics, Vol. 53, pp. 070301-1-4 (2014). (IF=1.384, TC=2)
2. KenyaNishiguchi, Syota Kaneki, Shiro Ozaki, and Tamotsu Hashizume, “Current linearity and operation stability in Al₂O₃-gate AlGa_N/Ga_N MOS high electron mobility transistors”, Japanese Journal of Applied Physics, Vol. 56, pp. 101001-1-8 (2017). (IF=1.384, TC=0)

Proceedings

1. KenyaNishiguchi and Tamotsu Hashizume, “Surface charging effects on current stability of AlGa_N/Ga_N HEMTs”, Proc. of The 2014 International Meeting for Future of Electron Devices, Kansai (IMFEDK), pp. 66-67 (2014).
2. KenyaNishiguchi, Joel T. Asubar, N. Tamaki, and Tamotsu Hashizume, “Evaluation of surface charging at AlGa_N surface using dual-gate structure”, Proc. of The 11th Topical Workshop on Heterostructure Microelectronics (TWHM), pp. 19-20 (2015).
3. KenyaNishiguchi, Shota Kaneki, and Tamotsu Hashizume, “Effects of bias annealing on current linearity of Al₂O₃/AlGa_N/Ga_N MOS HEMTs”, Proc. of The 12th Topical Workshop on Heterostructure Microelectronics (TWHM), pp. 21-22 (2017).

Journals related to this study

1. Kota Ohi, Joel Tacla Asubar, KenyaNishiguchi, and Tamotsu Hashizume, “Current Stability in Multi-Mesa-Channel AlGa_N/Ga_N HEMTs”, IEEE Transactions on Electron Devices, Vol. 60, No. 10, pp. 2997-3004 (2013).
2. Joel Asubar, Kota Ohi, KenyaNishiguchi, and Tamotsu Hashizume, “Improved current stability in multi-mesa-channel AlGa_N/Ga_N transistors”, Physica Status Solidi C, Vol. 11, No. 3-4, pp. 857-861 (2014).
3. Shiro Ozaki, Kozo Makiyama, Toshihiro Ohki, Naoya Okamoto, Shota Kaneki, KenyaNishiguchi, Naoki Hara, and Tamotsu Hashizume, “Effects of air annealing on DC characteristics of InAlN/GaN MOS high-electron-mobility transistors using atomic-layer-deposited Al₂O₃”, Applied Physics Express, Vol. 10, No. 6, pp. 061001-1-4 (2017).
4. Tamotsu Hashizume, KenyaNishiguchi, Shota Kaneki, Jan Kuzmik, and Zenji Yatabe, “State of the art on gate insulation and surface passivation for Ga_N-based power HEMTs”, Materials Science in Semiconductor Processing, 掲載決定 (2018年4月公表予定)

Conferences

International conferences

1. KenyaNishiguchi and Tamotsu Hashizume, “Surface charging effects on current stability of AlGa_N/Ga_N HEMTs”, The 2014 International Meeting for Future of Electron Devices, Kansai (IMFEDK), PB-08, Kyoto, Japan, June 19-20, 2014.
2. KenyaNishiguchi, Joel T. Asubar and Tamotsu Hashizume, “Spatial discrimination of surface charging region in AlGa_N/Ga_N HEMTs investigated using dual-gate architecture”, The International Workshop on Nitride Semiconductors (IWN), WeEP2, Wrocaw, Poland, August 24-29, 2014.
3. KenyaNishiguchi, Joel T. Asubar, N. Tamaki, and Tamotsu Hashizume, “Evaluation of surface charging at AlGa_N surface using dual-gate structure”, 11th Topical Workshop on Heterostructure Microelectronics (TWHM), 2-6,

Takayama, Japan, August 23-26, 2015.

4. KenyaNishiguchi, Joel T. Asubar, N. Tamaki, and Tamotsu Hashizume, "Controllability improvement of Al_2O_3 -gate structure for GaN transistors", Compound Semiconductor Week (CSW), WeB2-2, Toyama, Japan, June 26-30, 2016.
5. KenyaNishiguchi, Syota Kaneki, and Tamotsu Hashizume, "Improving Gate controllability of AlGaIn/GaN MOS HEMTs", 12th International Conference on Nitride Semiconductors (ICNS), C 2.3, Strasbourg, France, July 24-28, 2017.
6. KenyaNishiguchi, Joel T. Asubar, N. Tamaki, and Tamotsu Hashizume, "Effects of bias annealing on current linearity of $\text{Al}_2\text{O}_3/\text{AlGaIn}/\text{GaN}$ MOS HEMTs", 12th Topical Workshop on Heterostructure Microelectronics (TWHM), 3-6, Kirishima, Kyushuu, Japan, August 28-31, 2017.

Domestic conferences

1. 西口賢弥, Joel T. Asubar, 橋詰保, "デュアルゲート構造による AlGaIn/GaN HEMT の電流コラプス評価", 第 74 回応用物理学会秋季学術講演会, 20a-D7-11, 同志社大学, 平成 25 年 9 月.
2. 西口賢弥, Joel T. Asubar, 橋詰保, "デュアルゲート構造による AlGaIn/GaN HEMT のオフ状態ストレスによる電流変動評価", 第 49 回応用物理学会北海道支部学術講演会, A-20, 北海道大学, 平成 25 年 12 月.
3. 西口賢弥, Joel T. Asubar, 橋詰保, "AlGaIn/GaN HEMT におけるオフストレス後の電流変動評価", 第 61 回応用物理学会春季学術講演会, 19a-D8-5, 青山大学, 平成 26 年 3 月.
4. 西口賢弥, Joel T. Asubar, 橋詰保, "AlGaIn/GaN HEMT におけるオフ状態ストレス後の表面帯電評価", 第 62 回応用物理学会春季学術講演会, 12p-A21-10, 東海大学, 平成 27 年 3 月.
5. 西口賢弥, 橋詰保, "高温アニールプロセスが GaN MOSFET 特性に与える影響", 第 63 回応用物理学会春季学術講演会, 22a-W541-6, 東京工業大学, 平成 28 年 3 月.
6. 西口賢弥, 橋詰保, "GaN キャップ層が AlGaIn/GaN MOS 構造の C-V 特性

- に与える影響”, 第 64 回応用物理学会春季学術講演会, 16a-P4-10, パシフィ
コ横浜, 平成 29 年 3 月.
7. 西口賢弥, 金木 奨太, 橋詰保, “ Al_2O_3 膜を用いた AlGaIn/GaN MOS HEMT
の電流制御性向上”, 第 78 回応用物理学会秋季学術講演会, 7p-S22-4, 福岡
国際会議場, 平成 29 年 9 月.

Awards

1. “第 17 回応用物理学会北海道支部発表奨励賞” 西口賢弥, Joel T. Asubar,
橋詰保, “デュアルゲート構造による AlGaIn/GaN HEMT のオフ状態スト
レスによる電流変動評価”, 平成 25 年 12 月.